On-line monitoring of electroactive biofilms on the electrodes of bioelectrochemical systems by means of heat transfer biofilm sensors

Zur Erlangung des akademischen Grades eines

DOKTORS DER INGENIEURWISSENSCHAFTEN (Dr.-Ing.)

von der KIT-Fakultät für Chemieingenieurwesen und Verfahrenstechnik des Karlsruher Instituts für Technologie (KIT)
genehmigte

DISSERTATION

von

M.Sc. Andreas Netsch

aus Darmstadt

Tag der mündlichen Prüfung: 06.06.2025

Erstgutachter: Prof. Dr. Harald Horn

Zweitgutachter: Prof. Dr.-Ing. Dirk Holtmann

Acknowledgements

Over the last 5 years working on this thesis, I have received a huge amount of support, for which I would like to express my sincere gratitude. With the help of many people I would not have been able to bring this work to completion.

First and foremost, I would like to thank Prof. Harald Horn for the opportunity to write my PhD Thesis at the Engler-Bunte-Institut as well as for his guidance, quick and clear advice for any issues that arose.

For my practical supervision, I would like to thank Michael for his help and ideas on any kind of problems that have arisen. And giving me the freedom to develop and follow my own ideas.

For taking on the second examiner on my thesis, I would like to thank Prof. Dirk Holtmann.

A special thanks belongs to Johannes Reiner and Max Hackbarth for your tremendous support in helping me understand the initially sometimes crazy world of bioelectrochemistry and bringing back the good spirit to the lab in the post-COVID times. Though we still at times remained puzzled what is happening (not working as expected) in our systems, I would like to thank the entire bioelectrochemistry group for your endless willingness to discuss and brainstorm ideas with which we could solve some (most?) of the problems we faced. ... and develop many more questions to pose.

To my fellow PhD students and colleagues it was a pleasure working with you and I am thankful for the collaborative and friendly spirit that we shared at our institute. Especially to Szilard, Stephan, Mehran, Giorgio and Amelie for their friendship. I also want to thank Andrea for her care and personal advice.

To my students, Alissa, Zhaoyu, Danning, Shaswata, Inka it was a great experience and pleasure to supervise you in your thesis and your contributions to my research. Especially, Inka, thank you for allowing me to convince you over and over again to stay longer until that last experiment was finally completed.

The EBI wouldn't function without a lot of work behind the scenes. Therefore, I want to firstly thank Gudrun Abbt-Braun unmatched effort and work ethic in organizing the institute and solving any administrative issues. For their work behind the scenes a big thanks to Ursula Schäfer and Sylvia Heck. Also I want to thank our technicians for the amusing times during the supervision of the practical

courses. And especially, Axel for the measurement of numerous IC samples. My experiments wouldn't have been possible without the EBI-Workshop: Freddy, Erwin, Dennis, Jogi, thank you for taking my sometimes imperfect sketches and drawings and construct anything from small creative solutions to big reactors.

Ultimately, I want to thank my friends and family for their support and pushing me through the downs and cheering with me the ups of the my PhD journey.

Abstract

Bioelectrochemical systems (BES) are a promising technology for the energy and resource recovery from waste streams. Utilizing the ability of electroactive bacteria to transfer electrons to an external solid acceptor enables the linking of the bacterial metabolism with electrochemical systems. Most prominently investigated among the BES are microbial fuel cells (MFC) and their integration into wastewater treatment. Upscaling and long-term stable operation of MFCs, though, remains challenging. Electroactive biofilms like other productive biofilms face the trade-off between thick biofilms harboring a high count of bacterial cells and the mass and charge transport limitations as a consequence of the diffusive or electrical constraints. For long-term stable operation the control of the biofilm structure within an optimal range will be crucial for the viability of the technology in wastewater treatment.

The main objective of this dissertation was to investigate of the applicability of a heat transfer biofilm sensor on the anodes of a bioelectrochemical system to support the detection of limiting conditions caused by excess biofilm accumulation.

Two major aspects were demonstrated within this thesis. Firstly, a commercially available biofilm sensor was integrated into different flow cells on a carbonaceous electrode material, commonly applied in BES. The sensor sensitivity was determined for the conversion of the dimensionless sensor signal into a structural biofilm parameter (e.g., mean thickness). Influences of substratum material and geometry, as well as hydrodynamics on the sensor measurement were identified and quantified. Most favorable sensor sensitivities in the range of below 1 $\mu m^3/(\mu m^2 \times a.u.)$ were found at high flow velocities (27 cm/s) on a planar substratum. A theoretical model incorporating material properties, geometry and hydrodynamic conditions was developed for the prediction of the sensor sensitivity, allowing for an integration into various systems.

Secondly, the optimal range for the anodic biofilm thickness was determined for an electroactive biofilm cultivated from wastewater in a microbial electrolysis cell (MEC). The maximum current density in the MEC was in the range of 3.5 A/m^2 with a mean biofilm thickness on the anode of 100 - 150 μm. Thicker biofilms displayed a deteriorating performance as a consequence of increased substrate limitations and pH gradients, along with increasing electrical charge resistance.

The results from this thesis show the necessity to control the anodic biofilm thickness in BES for a long-term stable operation. Biofilm sensors, especially the heat transfer sensor investigated in this thesis, present a viable option for the support of biofilm control in technical systems.

Kurzfassung

Bioelektrochemische Systeme (BES) sind eine vielversprechende Technologie für die Energie- und Ressourcenrückgewinnung aus Abfallströmen. Die Fähigkeit von elektroaktiven Mikroorganismen zur direkten Elektronenübertragung auf einen festen externen Elektronenakzeptor ermöglicht es den bakteriellen Stoffwechsel mit elektrochemischen Systemen zu verknüpfen. Die am prominentesten untersuchten BES sind mikrobielle Brennstoffzellen (MBZ) und ihre Integration in die Abwasseraufbereitung. Das Upscaling und der stabile Langzeitbetrieb von MBZ bleibt jedoch eine Herausforderung. Die Nutzung elektroaktiver Biofilme geht, wie bei anderen produktiven Biofilmen, auch mit dem Kompromiss zwischen einem dicken Biofilm, der eine hohe Anzahl von Bakterienzellen tragen kann, und den Beschränkungen des Massen- und Ladungstransports als Folge der diffusiven oder elektrischen Limitierungen, einher. Für einen stabilen Langzeitbetrieb ist die Kontrolle der Biofilmstruktur innerhalb eines optimalen Bereichs für den Einsatz von BES in der Abwasseraufbereitung entscheidend.

Hauptziel dieser Dissertation war die Untersuchung der Anwendbarkeit eines wärmeleitenden Biofilmsensors auf den Anoden eines BES zur Identifizieurng von Limitierungen des Stofftransports im Biofilm, die durch eine übermäßige Biofilm-Akkumulation hervorgerufen werden.

Zwei Kernaspekte wurden in dieser Arbeit aufgezeigt. Erstens wurde ein kommerziell erhältlicher Biofilmsensor in verschiedene Durchflusszellen auf einem kohlenstoffbasierenden Elektrodenmaterial integriert, das typischerweise in BES verwendet wird. Die Sensitivität des Sensors wurde für die Umwandlung des dimensionslosen Sensorsignals in einen strukturellen Biofilmparameter (z.B. mittlere Dicke) bestimmt. Die Einflüsse von Material und Geometrie des Substratums, sowie der hydrodynamischen Bedingungen auf die Sensormessung wurden identifiziert und quantifiziert. Die beste Sensorsensitivität im Bereich von unter 1 $\mu m^3/(\mu m^2 \times$a.u.) wurde bei hohen Strömungsgeschwindigkeiten (27 cm/s) auf einem flachen Substratum gemessen. Ein theoretisches Modell, das Materialeigenschaften, die Geometrie des Substratums und die hydrodynamischen Bedingungen berücksichtigt, wurde für die Vorhersage der Sensorsensitivität entwickelt, was eine Integration in verschiedene Systeme ermöglicht. Zweitens wurde der optimale Bereich für die Dicke eines anodischen Abwasserbiofilms in einer mikrobiellen Elektrolysezelle (MEZ) bestimmt. Die maximale Stromdichte in der MEZ lag im Bereich von 3,5 A/m^2 bei einer mittleren Biofilmdicke auf der Anode von 100 - 150 μm. Dickere Biofilme zeigten eine abnehmende Leistung als Folge der zunehmenden Substratlimitierung und pH-Gradienten, zusammen mit einem zunehmenden elektrischen Leitungswiderstand im Biofilm.

Die Ergebnisse dieser Arbeit zeigen die Notwendigkeit der Kontrolle der anodischen Biofilmdicke in BES für einen stabilen Langzeitbetrieb. Biofilmsensoren, insbesondere der in dieser Arbeit untersuchte Wärmeleitungssensor, stellen eine praktikable Option für die Unterstützung der Biofilmkontrolle in technischen Systemen dar.

Contents

List of Figures

List of Tables

List of Abbreviations

Abbreviation	Description
BES	Bioelectrochemical system
C-PP	Graphite-Polypropylene
CLSM	Confocal Laser Scanning Microscopy
COD	Chemical Oxygen Demand
DET	Direct Electron Transfer
EAB	Electroactive Bacteria
EET	Extracellular Electron Transfer
EPS	Extracellular polymeric Substances
MBR	Membrane Bioreactor
MEC	Microbial Electrolysis Cell
MES	Microbial Electrosynthesis Cell
MET	Mediated Electron Transfer
MFC	Microbial Fuel Cell
OCT	Optical Coherence Tomography
OD	Optical density
ORR	Oxygen Reduction Reaction
PC	Polycarbonate
PEM	Proton Exchange Membrane
PUR	Polyurethan
PVC	Polyvinylchloride
SST	Stainless Steel
TEA	Terminal Electron Acceptor
TRL	Technological Readiness Level
VFA	Volatile Fatty Acids

List of Symbols

Latin symbols

Symbol	SI-unit	Definition
A	m^2	area
BV	m^3	biovolume
c	mol/m^3	concentration
CE	%	coulombic efficiency
d	m	diameter
D	a u	sensor signal
F	C/mol	Faraday's constant
h	m	height
i	A/m^2	current density
I	A	current
l	m	length
L	m	thickness
m	kg	mass
n	–	number of replicas
N	–	number of pixels
Nu	–	Nusselt number
$\dot{P}$	W	Power
Pr	–	Prandtl number
Q	m^3/s	volumetric flow rate
$\dot{Q}$	W	heat flux
r	m	radius
R	K/W	thermal resistance
R_a	m	roughness
R_a^{star}	–	roughness coefficient
Re	–	Reynolds number
SC	%	substratum coverage

Symbol	SI-unit	Definition
t	s	time
T	K	temperature
u	m/s	flow velocity
U	V	voltage
V	m^3	volume
w	m	width

Greek symbols

Symbol	SI-unit	Definition
α	$W/(m^2\,K)$	heat transfer coefficient
γ	–	intermittence factor
Δ	–	difference
ϵ	–	fraction
η	–	turbulence factor
λ	$W/(m\,K)$	thermal conductivity
ρ	kg/m^3	density
ϕ	–	porosity

Indizes

Index	Definition
An	anode
Cat	cathode
exp	experimental
F	biofilm
grav	gravimetric
i	inner
inorg.	inorganic
tbl	thermal boundary layer
th	thermal

1 Introduction

Novel technologies are urgently required throughout all sectors of the industry and society to achieve carbon neutrality. This includes the chemical as well as the water treatment industry. A transformation of the petro-based chemical industry towards an integration into a more circular economy needs to include biotechnological processes towards a green bioeconomy. Municipal and industrial waste streams, therefore, should be regarded as energy and resource streams (Rani et al. 2022).

Biological wastewater treatment has already long been established in municipal and industrial wastewater treatment (Gujer 2007). In the last 25 years bioelectrochemistry has arisen as a promising biotechnological approach for energy and resource recovery from wastewater. Exploiting the ability of specific microorganisms to transfer electrons from their metabolism to an electron acceptor outside of the cell, bioelectrochemistry offers the possibility for direct conversion of the chemically bound energy in the waste stream to electricity, hydrogen or the production of value-added chemicals (Slate et al. 2019). Among the bioelectrochemical systems (BES) the application of microbial fuel cells (MFC) in wastewater treatment has rendered the most probable use case (Mateo et al. 2018). Currently, significant amounts of energy are used for the treatment of wastewater. It is estimated, that approx. 20 % of municipal current consumption in Germany is caused by wastewater treatment (Fricke 2009). The aeration required in conventional wastewater treatment plant is energy intensive, accounting for 50-80 % of the energy consumption (Fricke 2009). MFCs allow for the simultaneous removal of organic compounds in the wastewater under anaerobic conditions and power production, drastically reducing the required energy input due to aeration (Mateo et al. 2018).

Although, BES and especially MFCs, have been subject to intensive research efforts in the last two decades, the technology has yet to be successfully introduced into the market, as there are only a few pilot-scale MFC-systems up to 1,000 L reported (Babanova et al. 2020; Blatter et al. 2021; Heinrichmeier et al. 2023). Recent evaluations of the technological readiness have estimated the Technological Readiness Level (TRL), based on the NASA evaluation system, around 4-5, which applies to, technologies that have been validated in lab environments, but no prototypes in an industrial environment have been demonstrated (Ieropoulos et al. 2024; Rani et al. 2022). For comparison, the maximum TRL is 9 for fully proven systems in an operational environment. Upscaling BES from lab-scale/pilot-scale systems to larger scales has been challenging (Dewan et al. 2008; Logan 2010). Due to a number of issues the scalability of BES and long-term stable and efficient operation has yet

to be achieved. The challenges include low power output and deteriorating long-term performance as a consequence of low substrate concentrations, high internal resistance and mass transport limitations (Mateo et al. 2018).

The electroactive biofilm in BES can be considered a productive or beneficial biofilm (Edel et al. 2019; Philipp et al. 2024). Similar to the productive biofilms in membrane biofilm reactors efficient substrate supply is necessary for the utilization of electroactive biofilms in a technical system. Consequently, mass transport limitations due to the structural properties of the biofilm (e.g., thickness, density, porosity) need to be avoided to ensure a long-term stable operation (Belleville et al. 2022). A prerequisite for the control of the biofilm structure, to the optimal range between cell accumulation and unhindered mass transport of substrate through the biofilm, is the knowledge of the current state of the biofilm. Monitoring the electroactive biofilm on the electrodes of BES would support the identification of occurring mass transport restrictions, diminishing the efficiency of the BES.

The overall aim of this thesis was to investigate and demonstrate the feasibility of the integration of heat transfer biofilm sensors for the monitoring of electroactive biofilms onto anodes of a BES. Within the framework of upscaling BES from lab-scale to technical scale reactor systems, that can be integrated into wastewater treatment plants, technically established biofilm sensors are required for the monitoring of the biofilm structure, as most laboratory monitoring techniques are hard to integrate or not compatible for the targeted application. Therefore, a commercially available biofilm sensor (DEPOSENS, Lagotec GmbH, Magdeburg, Germany) was investigated and adapted towards the integration in the anodes of a BES. For the practical application the dimensionless sensor signal requires to be transformed to structural biofilm parameters (e.g., mean biofilm thickness).

This work was divided into three steps, displayed in the Chapters 3 to 5.

Firstly, the material compatibility of a typical carbonaceous electrode material (graphite-polypropylene C-PP) with the DEPOSENS sensor was tested (see Chapter 3). Due to the different material properties, foremost the thermal conductivity of the substratum, in comparison to the standard material (stainless steel - SST), the sensor is applied to, an impact of the substratum was expected. The sensitivity of sensors applied to C-PP pipes and the standard SST pipes were investigated in the cultivation of an anaerobic wastewater biofilm. Additionally, the impact of the sensor settings for the measurement was determined.

Secondly, for the broad applicability of the sensor, geometric and hydrodynamic impacts on the sensor measurement were quantified (see Chapter 4). The biofilm sensor was integrated into meso-fluidic flow

cells for an in-depth analysis of the biofilm structure by means of optical coherence tomography to develop a theoretical model for the prediction of the sensor sensitivity.

In a third step, the necessity of on-line monitoring of electroactive biofilms was proven for the mitigation of mass transfer limitations and the identification of an optimal thickness for anodic wastewater biofilms (see Chapter 5). The biofilm thickness, quantified by means of optical coherence tomography and continuously monitored with the heat transfer biofilm sensor, was correlated with the current production from a BES. Thereby, demonstrating the feasibility of the integration of the DEPOSENS biofilm sensor for the application in BES.

2 Fundamentals

2.1 Bioelectrochemical Systems

Bioelectrochemical systems (BES) is the summarizing term for technologies coupling the biological conversion of chemical species with the transfer of electrons beyond the boundaries of the microorganism involved in the reaction. The phenomena of extracellular electron transfer (EET) has first been described by Potter in (1911) with specific bacteria producing an electromotive force along with the consumption of organic compounds. For the technical utilization of this mechanism so called electroactive bacteria (EAB), generally, require forming biofilms on conductive solid interfaces (electrodes). Similar to a chemical fuel cell, BES are composed of a two-electrode system, anode and cathode, that are connected electrically by an external circuit. Both electrodes are immersed into an electrolyte, that in case of dual chamber systems is separated into anolyte and catholyte by a proton exchange membrane (PEM) (Franks and Nevin 2010; Logan 2007). For single chamber systems both electrodes share a common electrolyte. Figure 2.1 shows a general sketch of a single chamber BES.

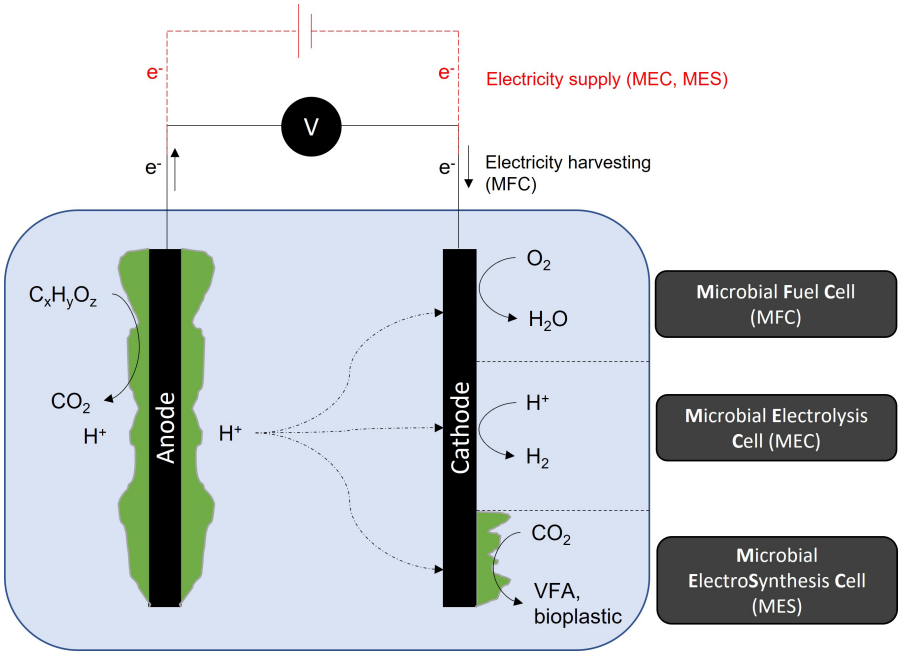

Figure 2.1: Sketch of a bioelectrochemical system (BES) displaying the basic reactions at the anode (oxidation of organic substrate) and the cathode (reduction). Depending on the cathodic reaction BES are classified in different configurations: Microbial Fuel Cells (MFC) for electricity production, Microbial Electrolysis Cells (MEC) for hydrogen production and Microbial Electrosynthesis Cells (MES) to produce value-added chemicals (e.g., volatile fatty acids (VFA) or bioplastics).

One or both reactions (oxidation at the anode or reduction at the cathode) are biologically catalyzed with the utilization of EAB in BES. Depending on the spontaneous or forced reactions taking place at the anode and cathode, BES can be categorized into various technologies (Logan et al. 2006). Microbial fuel cells (MFC), microbial electrolysis cells (MEC) and microbial electrosynthesis cells (MES) have received the most attention recently, and are briefly presented with their respective potential fields of application.

Microbial fuel cells are the most investigated type of BES. At the anode EAB oxidize organic substrates under anaerobic conditions to carbon dioxide and protons. Electrons deriving from the oxidation are transferred to the anode, which acts as terminal electron acceptor (TEA) for this reaction (Schröder 2007). The cathodic counterreaction can vary for MFCs. Most commonly an oxygen reduction reaction (ORR) has been utilized at the cathode (Cheng and Logan 2011). To avoid or reduce oxygen crossover to the anodic chamber, cathodes in MFCs are often constructed as gas diffusion electrodes, for an efficient transport of the oxygen to the catalytic layers of the cathode, while reducing the amount of oxygen dissolved in the electrolyte (Haupt et al. 2022). Alternatively, the anode and cathode chamber are separated by a PEM. Oxygen intrusion to the anodic chamber should be avoided as some EAB, e.g., *Geobacter sulfurreducens* has limited to no aerotolerance (Lin et al. 2004). Also, the presence of oxygen in the proximity of the anode acts as an alternate TEA to the anode, which limits the possible current production. An alternative cathodic counterreaction can be the denitrification. Both oxidized nitrogen species, nitrate and nitrite, have been used as electron acceptor at the cathode, despite theoretical decreased power output due to the more positive reaction potential of the denitrification in comparison to the ORR (Virdis et al. 2010; Virdis et al. 2008). MFCs have predominantly been investigated towards their integration into municipal or industrial wastewater treatment plants. Various sources of substrates have been utilized as carbon source, showing the wide variability of the carbon source for the anodic reaction (Pandey et al. 2016). In comparison to a chemical fuel cell, far lower current densities can be produced due to a combination of low conductivity of the electrolyte (wastewater), low substrate concentration and complex composition of the organic substrate. Maximum power densities reported for a MFC with an anodic area larger than 100 cm^2 were approx. 500 mW/m^2 (Mateo et al. 2018). Nevertheless, given the abundance of wastewater streams, along with decreased sludge production and aeration requirements compared to conventional wastewater treatment plant, MFCs have the potential for more energy-efficient treatment of wastewater (Rawat and Shandilya 2020).

Microbial Electrolysis Cells (MEC) similar to MFCs utilize an anodic electroactive biofilm for the oxidization of organic substrates, but differ from MFCs in their cathodic reaction. In contrast to

MFCs, in which electricity generation is the target, in MECs an external cell voltage ($> 0.2\,V$) is applied to the electrodes to overcome the threshold potential for cathodic hydrogen evolution (Nam et al. 2011). Protons, which are a product of the anodic oxidation reaction, diffuse to the cathode where they are reduced to hydrogen. Both anodic and cathodic reactions must be conducted under anaerobic conditions. The required external voltage for the cathodic hydrogen evolution in a MEC falls below that of conventional electrochemical electrolysis (typically a cell voltage of $1.8\,V$ is applied) by far (Zhang and Angelidaki 2014).

Microbial Electrosynthesis Cells (MES) have recently found more attention among the BES. Here cathodic electroactive biofilms utilize the electrode as an external electron source (Rosenbaum et al. 2011). With an applied external voltage electrons can be accepted by specific EAB and incorporated in their metabolism for e.g., CO_2 fixation for the production of organic substances (Harnisch and Holtmann 2019; Harnisch and Schröder 2010). Possible products that have been demonstrated include the production of the biopolymer polyhydroxybutyrate (PHB) by the knallgas bacterium *Kyrpidia spormannii* (Hackbarth et al. 2020), acetate as well as further elongation of the carbon chain of volatile fatty acids up to C6 (Flexer and Jourdin 2020; Jourdin et al. 2020). As a counter-reaction, commonly an abiotic reaction such as the water splitting reaction at the anode is utilized.

2.2 Mass and electron transport in electroactive biofilms

The predominant growth form for bacteria is in biofilms, due to the inherent advantages provided to the individual cell (Butler and Boltz 2014). It is estimated up to 80% of all bacterial species are commonly found in biofilms and not as planktonic cells (Römling 2023). Within a biofilm the bacterial cells are embedded into a matrix of extracellular polymeric substances (EPS), mostly secreted by the microorganisms, and typically adhered to a solid interface. In case of electroactive biofilms in BES the electrodes. Forming biofilms provides the microorganisms protection from harsh shear stress, antimicrobial substances and dehydration, as well as the possibility for synergistic relationships among different bacterial species (Flemming et al. 2016). The structure of biofilms, especially for mixed culture biofilms, are often heterogeneous with a high spatial and temporal variability, depending on the microbial species, local hydrodynamic and environmental conditions (substrate availability, pH, substratum, ...) (Butler and Boltz 2014). Biofilms forming on the electrodes of BES harboring microorganisms with the ability to transfer electrons from their metabolism beyond the cell membrane, are called electroactive biofilms. Similar to biofilms developing membranes with a two-sided substrate

supply in membrane biofilm reactors (Edel et al. 2019), the structure of electroactive biofilms depends on two constraints: the substrate supply through the bulk-phase and the resistance of the electron transfer via EET from bacterial cell to electrode or vice versa (Belleville et al. 2022).

Extracellular electron transfer mechanism

EET of microorganisms is the key mechanism behind bioelectrotechnology linking the biological conversion of substrates with the electrochemistry. Generally, EETs can be put into two categories: Direct electron transfer (DET), in which the electrons are transferred from microorganism to electrode through a direct physical connection and mediated electron transfer, where soluble redox mediators act as electron shuttles between the microbial cell and the electrode (Schröder 2007). The mechanisms of electron transfer do not differ between anodic and cathodic biofilms, as they can act either way towards the electrode or from the electrode to the microorganism (Rosenbaum et al. 2011). An overview of the different EET mechanisms is displayed in Figure 2.2.

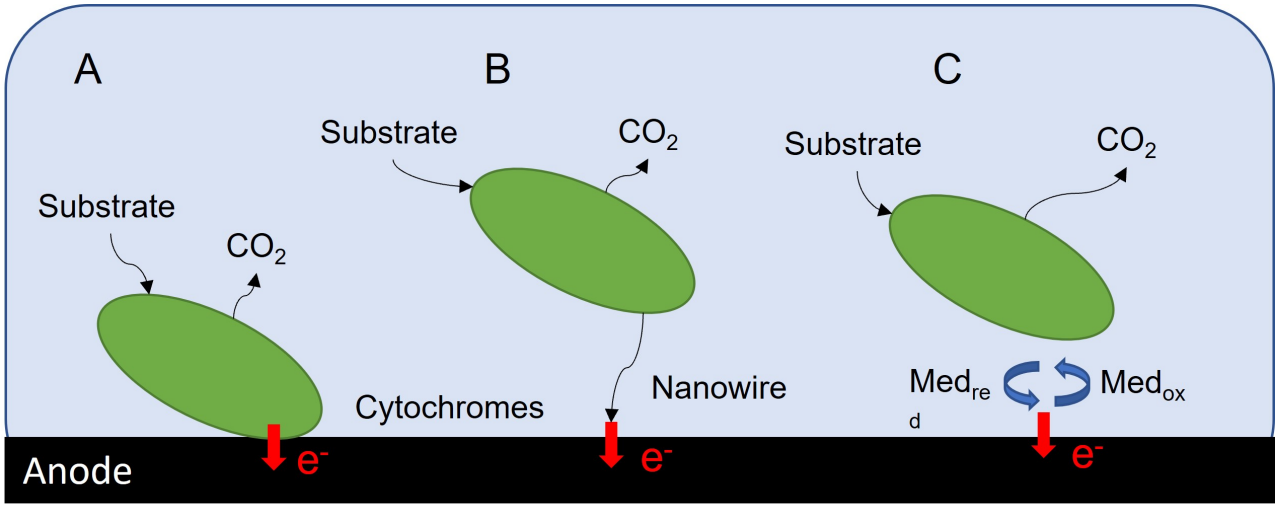

Figure 2.2: Illustration of the different mechanisms of EET: A: Direct electron transfer via Cytochromes, B: Direct electron transfer via conductive nanowires, C: Mediated electron transfer. (Adapted from (Schröder 2007))

Direct electron transfer is only known for a few electroactive microbial species (e.g., Geobacter, Shewanella, Rhodoferax) as it requires membrane bound protein relays in the microorganism, that enable electrons to bridge from the interior of the cell to an externally accessible redox site (Schröder 2007). Most commonly described for this transfer mechanism are type C-cytochromes that, when in direct contact with a solid external electron acceptor - in case of a MFC the anode, can transfer the electrons from the microbial metabolism. This direct mechanism via type C-cytochromes however

require the direct contact of the protein with the solid interface, which would limit the electroactivity of a biofilm to a single monolayer of bacteria. For longer ranged electron transfer conductive nanowires (e-pili) can develop from the cytochromes in the cell membrane towards the electrode or form a network of interlinked nanowires throughout the biofilm, enabling not only direct electron transfer from microbial cell to the electrode but also between different cells within the biofilm (Malvankar et al. 2011; Reguera et al. 2006). Conductive e-pili can have a length of approx. 10-20 µm for *Geobacter sulfurreducens*, a model electroactive organism (Reguera et al. 2006). However, there seem to be conductive proteins dispersed within the EPS of an electroactive biofilm that enhance its electrical conductivity for electron transfer (Edel et al. 2019). Renslow et al. (2013) even found the possibility of electron transfer bridging over metabolically inactive zones of the biofilm of several 100 µm, due to the conductivity of the biofilm itself. Dead cells within the biofilm though, may increase electron transfer resistance and therefore, decrease the efficiency of the biofilm.

Mediated electron transfer (MET), in contrast, relies on soluble redox species that are reduced at the microbial cell and are transported to the anode via diffusion, where they are oxidized (Wu et al. 2016). In case of cathodic biofilms,this mechanism is reversed. Carriers for the transport of electrons (also called electron shuttles) can be of endogenous nature and are secreted from the microbial cells (e.g., flavines, quinones, phenazines) or be artificially added (e.g., methylene blue) to enhance electron transport in the biofilm (Rahimnejad et al. 2011). The artificial addition of electron mediators, however, seems hardly sustainable in a continuous operation of large-scales BES. In terms of current densities, that can be produced, mediated electron transfer beats the possible current densities produced compared to DET mechanisms by far, however are limited in their transport distance to diffusive restrictions (Schröder 2007).

Mass transport limitations in electroactive biofilms

Providing sufficient nutrients (carbon source) to the microorganisms within the biofilm, as well as removing products (e.g., CO_2, H^+) from the bacterial metabolism is crucial from an efficient electroactive biofilm (Belleville et al. 2022). Mass transport requires to consider two domains in biofilm systems. Firstly, the mass transport from the bulk phase through the concentration boundary layer to the biofilm surface. This transport is subject to a combination of two mechanisms: diffusion and advection (Muffler and Ulber 2014). Secondly, the mass transport within the biofilm itself, commonly described as internal mass transport, is mainly dominated by diffusion (Stewart 2003). The effective diffusion coefficients thought depend on several parameters including the chemical species of the substrate, temperature and structural or morphological biofilm parameters (Horn and Morgenroth

2006). Low biofilm porosity (Yang et al. 2021), as well as, high cell density (Fan et al. 1990) hamper the diffusive transport by reducing the diffusion coefficients. Due to the heterogeneity of the biofilm structure local diffusion coefficients may vary with distance from the bulk and age of the biofilm (Renslow et al. 2010). The local diffusion coefficients tend to be lower at greater distances from the bulk, as well as in older biofilms, due to the higher biomass density (Renslow et al. 2010). Decreased diffusion coefficients along with elongated diffusion pathways (in thick biofilms) result in a decreased flux of substrate and products into or out of the biofilm. Typically, diffusion coefficients in biofilms are one order of magnitude lower than in pure water (Pereira et al. 2022c). For example, acetate diffusion coefficients assumed for the modeling of electroactive biofilms were reduced by a factor of 0.5 (Korth et al. 2015) or 0.8 (Kato Marcus et al. 2007). Electroactive biofilms can be considered as counter diffusion biofilms, with the substrate supply deriving from the bulk and the electron acceptor from the substratum (Belleville et al. 2022; Philipp et al. 2024). An illustration of the mass transfer in an anodic electroactive biofilm is shown in Figure 2.3

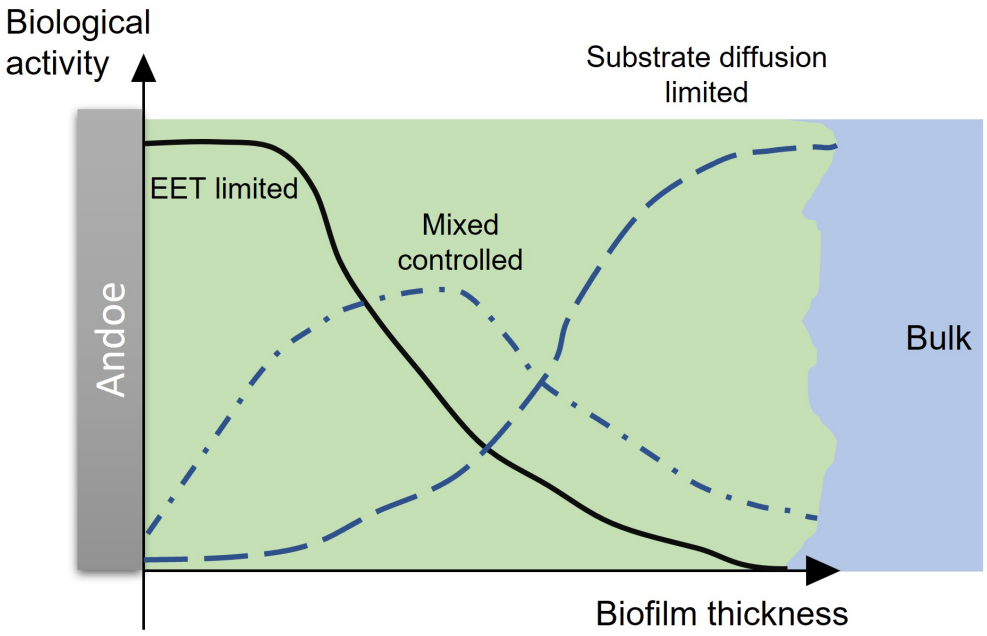

Figure 2.3: Display of substrate and electron limitation in an anodic biofilm (Adapted from Belleville et al. 2022)

Developing transport gradients within a biofilm are inevitable and can consequently impair the efficiency or even functionality of a productive biofilm. With respect to an anodic biofilm the most relevant chemical species to be transported from bulk to biofilm and vice versa are the carbon source (e.g., acetate, glucose, other organic substrates), and the products from the bacterial metabolism:

CO_2/bicarbonate and protons. Insufficient substrate supply will result in deteriorating current production, as the reaction will be limited from the side of the electron donor (Kato Marcus et al. 2007; Oliveira et al. 2013). The layers closest to the anode, that presumably have the highest efficiency given their short electron transfer distance, are most drastically affected by the substrate limitation in a biofilm. An example for the dependency of the substrate penetration depth and thereby the substrate limitation of some regions of the biofilm is given by Pereira et al. (2022c). They found the maximum non-limiting thickness of an electroactive biofilm was 55 µm (8 mM acetate), 24 µm (2 mM acetate) and only 10 µm (0.5 mM acetate) in a microbial electrolysis cell. The dependency of the current production on the available substrate concentration was demonstrated by Sapireddy et al. for *Geobacter sulfurreducens* and *Desulfuromonas acetexigens* (Sapireddy et al. 2021). For an acetate fed biofilm the current density increased along with an increased substrate concentration up to a concentration of 10 mM/L acetate, but stagnated with a further increase of the substrate concentration (Sapireddy et al. 2021).

An adverse effect on the current production of electroactive biofilms can also be caused by a lack of proton transport from the biofilm to the bulk phase. Proton accumulation in the biofilm leads to a shift of the pH to more acidic environment. Most EABs, however, are not acidophilic, so that their activity is partially or completely inhibited (Franks et al. 2009). *Geobacter sulfurreducens* was completely inhibited at pH < 5 along with a drastic decrease of their growth rate (Patil et al. 2011). Patil et al. (2011) described the operational window for anodic biofilms in the pH range between 6-9, with the maximum bioelectric activity being found at a more basic pH of 9. De Lichterverlede et al. (2019) in fact have even concluded from their model calculation that the predominant limitation in electroactive biofilms is not a consequence of limited transport of organic substrate or biofilm conductivity, moreover low pH values in the depth of the biofilm are most detrimental for the inhibition of the bacterial activity. Additionally, the pH value seems to affect the efficiency of the EET mechanisms. Both DET and MET are dependent on the local pH value in the biofilm (Malvankar et al. 2011; Wu et al. 2016). The effect of acidic pH values, though, can be mitigated with high buffer concentrations in the medium (Pereira et al. 2022b; Torres et al. 2008).

Optimal thickness for electroactive biofilms

Clearly, there is a trade-off when it comes to the optimal thickness of electroactive biofilms. Thin, e.g., monolayer biofilms, harbor only a comparatively low amount of EAB, while with increasing thickness of the biofilm, the electron transfer resistance increases as well as substrate and pH-gradients become larger. The relationship between accumulating biofilm thickness, thus the number of bacterial cells,

and current production in BES is widely accepted (Engel et al. 2019; Reguera et al. 2006). Recently, the maximum current densities related to the biofilm thickness have been found by various research groups are listed in Table 2.1. Philipp et al. (2024) suggested the maximum efficiency for *Geobacter sp.* biofilm with a medium thickness, due to the pH-limited electroactivity of biofilms to 100 µm.

Table 2.1: Overview of studies investigation the thickness of electroactive biofilms

Study	species	biofilm thickness
Sun et al. (2016)	*Geobacter sulfurreducens*	20 μm
Read et al. (2010)	*Geobacter sulfurreducens*	30 μm
Reguera et al. (2006)	*Geobacter sulfurreducens*	50 μm
Pinck et al. (2020)	*Geobacter sulfurreducens*	80 μm
Engel et al. (2019)	*Geobacter sulfurreducens*	69 μm
Engel et al. (2019)	*Geobacter sulfurreducens & Shewanella oneidensis*	93 μm

Certainly, these theoretically optimal biofilm thicknesses cannot be universally applied as the efficiency is influenced by a variety of parameters: type and concentration of the substrate, density of the biofilm, temperature, effective electrical conductivity of the biofilm, and structure of the electrode. The optimal thickness for a specific biofilm may be related to both bacterial species (Philipp et al. 2024) and system. Nevertheless, in addition to the need for an optimal thickness the importance of understanding the structural state of an electroactive biofilm becomes evident.

2.3 Biofilm sensors

Generally, a biofilm sensor detects the modified response of a deposit (e.g., biofilm) to an external signal from the sensor (Pereira and Melo 2023). Biofilm sensors for large-scale applications, in general, require meeting certain criteria, specific to the respective application, to provide relevant information. Ideally, biofilm sensors should be (Flemming 2003; Flemming et al. 1998; Pereira and Melo 2023):

- **continuous**: to provide steady information on the state of the monitored biofilm parameter in real-time
- **in-line and representative**: to measure the biofilm at a relevant and representative point of interest in the technical system with respect to hydrodynamics and substratum material
- **non-destructive and non-invasive**: the measurement of the biofilm should not alter the structure or growth of the biofilm

- **non-interfering**: the measurement principle of the sensor should not impede the functionality of the monitored technical system

In selecting a sensor for the respective application, the consideration of the biofilm parameters of interest and boundary conditions is necessary. An overview of commercially available biofilm or biofouling sensors is given in Table 2.2. All sensor listed here can be classified as on-line, real-time, in-situ, and non-destructive sensors (Pereira and Melo 2023). With regards to the targeted applications, thus far, all commercially available biofilm sensor focus on the detection of biofilm coupled with the use of cleaning agents for the subsequent removal of the biofilm. None of these sensors have been applied to control an electroactive biofilm to a predefined thickness. Considering the aim of this thesis to monitor the thickness of a biofilm on the electrodes of a MFC integrated into a wastewater treatment plant, thermal biofilm sensors seem to be the most viable option, due to the linear correlation of the thermal resistance with the biofilm thickness (Janknecht and Melo 2003). Biofilm sensors based on electrochemical measurement principles (ALVIM, BioGeorge, BIOX) would likely interfere with the bioelectrochemical process, although continuously monitoring the current or potential in a MFC could also be considered a monitoring of the activity of the electroactive biofilm, but would not provide direct information on its thickness. Optical based sensors (e.g., OPTIQUAD, BioDART, SOLution) would likely be impeded in their measurement by wastewater as a medium and could be difficult to integrate into a more complex technical system due to constructive constraints. Among the thermal biofilm sensors for this work the DEPOSENS sensor (Lagotec GmbH, Magdeburg, Germany) was chosen due to non-invasive nature of the measurement, as the sensor itself is integrated on the backside of the substratum. Thereby, the biofilm growth is not altered by changes of the local hydrodynamics by intruding sensor parts or the material properties of a different substratum.

Table 2.2: Overview of commercially available biofilm/fouling sensors. To the extent of available information the method of detection, the detected biofilm parameters and known fields of application are listed. Note that some of the information in this table is provided by the manufacturer themselves. Links to the websites are found below the table and were all accessed on 15.09.2024.

Commercial name	**working principle**	**Detection method/characteristics**	**Detected biofilm parameters**	**Known applications**
ALVIM[1] (Pavanello et al. 2011)	electrochemical	cathodic depolarization of a SST sample in reference to a clean sample	surface coverage (limit of detection: 1% of surface coverage)	cooling towers, beverage industry, reverse osmosis plant
BioGeorge[2] (Bruijs et al. 2001)	electrochemical	intermittent polarization of SST/Ti discs, detection of increased electrical impedance or current production by biofilm accumulation	biofilm activity	by-pass in pipeline of cooling systems
BIOX[3] (Mollica and Cristiani 2003)	electrochemical	quasi-intentiostatic cathodic polarisation	surface coverage, limited to thin biofilms	power plants
OPTIQuad[4] (Strathmann et al. 2013)	optical	simultaneous measurement of fluorescence, scattering, transmission and refraction	quantification of biomass, inorganic deposits and biological activity, suitable for thin biofilms <50µm	dairy wastewater, drinking water pilot system
BioDART[5]	optical	side-stream of flow system with narrow lumen detector - reduction of light transmittance of deposit	biofilm dynamics	cooling system

Continued on next page

Table 2.2 – continued from previous page

Commercial name	**working principle**	**Detection method/characteristics**	**Detected biofilm parameters**	**Known applications**
SOLution[6]	optical	live video from Ultra HD Camera in-line in the piping system	presence of biofilm	cooling systems
RO – Spotlight[7] (Rahardianto et al. 2020)	optical	high-resolution camera of illuminated background membrane	surface coverage	reverse osmosis membrane
OnGuard 3B *Analyzer*[8] (Biergans and Beardwood 2017)	mechanical & thermal	simultaneous detection via ultrasound reflection and heat transfer reduction	thickness of deposits (biofilm and scaling)	cooling system
DEPOSENS[9] (Netsch et al. 2021; Pratofiorito et al. 2024)	thermal	increase in thermal resistance with deposit accumulation at constant temperature difference between heater and reference probes	thickness of deposit (biofilm and scaling)	paper industry, heat exchangers, biogas scrubbers, geothermal plants, membrane filtration
Skidsense[10] (Crattelet et al. 2013)	thermal	application of constant or sinusoidal heat flux	thickness and chemical nature of deposit	heat exchangers, cooling systems, membrane applications

[1]www.alvimcleantech.com/cms/en/biofilmsensors, [2]si-biofilmgrowth.com/, [3]www.stelarwater.com/downloads/BIOX-2011.pdf,

[4]https://root.krohne.com/fileadmin/content/files-2/ctry_global/Newslines/NewsLine_OPTIQUAD-FFA_EN_121024.pdf

[5]www.chemaqua.com/en-us/Innovations/bioDART-Biofouling-Monitor, [6]www.solmicrotek.com/our-systems/solution/, [7]https://www.noriawater.com/,

[8]https://www.solenis.com/de-de/research-and-development/innovationen/onguard-3b-analyzer-for-biofouling/,

[9]https://lagotec.de/produkte.html, [10]https://www.richardhouriganinc.com/pdf/Skidsens_RHI.pdf

3 On-Line Monitoring of Biofilm Accumulation on Graphite-Polypropylene Electrode Material Using Heat Transfer Sensor

Published as: Netsch, A.; Horn, H.; Wagner, M. On-Line Monitoring of Biofilm Accumulation on Graphite-Polypropylene Electrode Material Using a Heat Transfer Sensor. Biosensors 2022, 12, 18. https://doi.org/10.3390/bios12010018

Abstract: Biofilms growing on electrodes are the heart piece of bioelectrochemical systems (BES). Moreover, the biofilm morphology is key for the efficient performance of the microbial fuel cells (MFC) and must be monitored and controlled for a stable operation. For the industrial use of microbial fuel cells, monitoring the biofilm directly on the electrodes inside the reactor is desirable. In this study a commercially available on-line heat transfer biofilm sensor is applied to a graphite-polypropylene pipe and compared to its standard version where the sensor is applied to a stainless-steel (SST) pipe. The aim was to investigate the transferability of the sensor to a carbonaceous material that is preferably used as electrode materials for BES. Thereby, enable biofilm monitoring directly on the electrode surface. The sensor's signals were correlated with the gravimetrically determined parameter biofilm thickness to identify its sensitivity on both materials. Results showed the transferability of the sensor to the graphite-polypropylene material, despite the sensor sensitivity was decreased by a factor of approx. 5 compared to the sensor applied to a SST pipe.

3.1 Introduction

Biofilms are used in a variety of technical systems in a beneficial or productive manner, cleaning water in the wastewater treatment over a wide range from membrane bioreactors (MBRs) (Sehar and Naz 2016) to trickling filters (Lewandowski and Boltz 2011). Among these technologies in wastewater treatment are BES, such as microbial fuel cells, as new sources of energy from wastewater (Bullen et al. 2006) or microbial electrosynthesis cells for the production of base chemicals (Harnisch and Schröder 2010). In microbial fuel cells, anodically grown electroactive biofilms oxidize organic compounds of the wastewater under anaerobic conditions, while in most studies in a separated cathodic chamber oxygen

as electron acceptor is reduced (Du et al. 2007; Logan 2007). The biofilms in microbial fuel cells create a protected environment for the electroactive bacteria, allowing for the bacteria to settle on the electrode surface, enabling the electron transfer between bacteria and electrode via conductive pili, cytochromes or electron shuttles (Logan 2007). The efficiency of electron transfer from the bacteria to the electrode is crucial for the overall performance of BES. Similar to other biofilm technologies the performance of microbial fuels cells depends on the morphological properties of the biofilm and an optimal biofilm structure (thickness, density) must be established to allow for a stable power output (Read et al. 2010; Sun et al. 2016). Bacteria with greater distance to the electrode do not further contribute to the current generation, as the electron transfer is constrained by the travel distance of the electrons from the bacteria to the electrode interface (Read et al. 2010). While increasing the biofilm density leads to an improved electrical performance, by reducing the electrical resistance of the biofilm and harboring more bacteria participating in the electron transfer, the viability of biofilms is the highest near the anode. In a simulation Kato Marcus et al. (2007) have shown that inert biomass such as dead cells or too thick biofilms on the anode deteriorate the electrical performance of a microbial fuel cell due to the substrate diffusion limitation to the surface of the electrode. Several groups of researchers have investigated the optimal biofilm thicknesses of MFCs. While an electroactive bacterium such as the *Geobacter sulfurreducens* in a monocultural biofilm can form thicknesses exceeding 100 µm (Pinck et al. 2020) it has been reported by Semenec and Franks (2015) that in multispecies wastewater biofilms bacteria located further than 50-70 µm from the electrode no longer contribute to the current production. Read et al. (2010) have reported a typical thickness for anodic biofilms in macro sized MFCs of approx. 50 µm. Therefore, a biofilm sensor to monitor the accumulation of biofilm on the electrode is required for the optimization of biofilm control strategies in BES towards a stable power generation. Biofilm monitoring requires on-line, in-situ, non-invasive measuring methods, that can be clearly attributed towards the formation of biofilms in the system (Flemming 2003). Sensors for biofilm measurement, generally spoken, are based on a modified response of the accumulated biofilm to a signal of the sensor (Janknecht and Melo 2003). A series of different biofilm sensors have been presented in literature based on impedimetric (Pires et al. 2013; Settu et al. 2015), electrochemical (Pavanello et al. 2011; Poma et al. 2021), spectroscopic (Nivens et al. 1995; Schmid et al. 2003) or thermal methods (Reyes-Romero et al. 2014; Wieland et al. 2021). Optical methods such as confocal laser scanning microscopy (CLSM) (Neu and Lawrence 2015; Neu et al. 2010) or optical coherence tomography (OCT) (Wagner and Horn 2017) for biofilm imaging have been used for the quantification of biofilm growth. The application of these optical methods is mostly limited to lab scale experiments, as they need additional sample staining (CSLM) or are limited in their ability to be integrated as

cost-efficient in-line sensors into industrial systems (Fischer et al. 2016). As each of these methods present different drawbacks or limitations such as detection range, the ability to distinguish between the compounds of the deposits, applicability and cost-efficiency for industrial systems, the choice of the sensor for the respective field of application must be evaluated in advance (Flemming 2003; Janknecht and Melo 2003).As cell attachment and biofilm development are dependent on the substratum (Donlan 2002), the biofilm thickness and structure are greatly influenced by the electrode material (Nevin et al. 2008; Semenec et al. 2015). Hence, for a representative measurement of the biofilm the sensor should be directly applied on the electrode of a bioelectrochemical system. The characteristics of an electrode material have been extensively studied and require high conductivity, mechanical and chemical stability, large surface areas and good biocompatibility (Kalathil et al. 2018; Logan et al. 2006; Yaqoob et al. 2020). Carbonaceous based or metal-based materials have been suggested as the main types of anode materials. Due to its low costs, good electrical conductivity and large surface area, carbonaceous based electrodes have established themselves as a versatile most commonly used source of electrodes in microbial fuel cells (Logan et al. 2006; Santoro et al. 2017). Among the metal-based materials, SST has distinguished itself as the most studied option dues to its outstanding mechanical properties, corrosion resistance and low costs compared to noble metals (Kalathil et al. 2018). Despite their higher electrical conductivity than carbonaceous based materials Dumas et al. have reported lower maximum power densities for SST electrodes in MFCs (Dumas et al. 2007). Plain SST bioanodes reported to inhibit bacterial adhesion due to their smooth surfaces and low surface area, therefore preventing the development of a robust electroactive biofilm necessary for high power densities in MFCs (Kalathil et al. 2018; Mustakeem 2015). In the current study a heat transfer biofilm sensor (DEPOSENS from LAGOTEC GmbH (Magdeburg, Germany)) was applied for the monitoring of biofilm accumulation on an electrode material. The latter is supposed to be used in a bioelectrochemical system (BES). In specific, the DEPOSENS sensor will be integrated into the fixed anode of a microbial fuel cell, which will be constructed as a rotating disk reactor with a rotating cathode. As comparison the DEPOSENS biofilm sensors were tested in parallel in a SST pipe and a pipe constructed out of composite graphite-polypropylene (Muddemann et al. 2017). The DEPOSENS sensor allows for the on-line monitoring of a closed technical system and can be directly integrated into the pipe system. Hence, measuring the biofilm accumulation directly at the point of interest. Unlike other biofilm sensors based on impedimetric (Pires et al. 2013) or spectrometric methods (Nivens et al. 1995) presented in literature, the chosen biofilm sensor is not limited to laboratory conditions, but is commercially available on a SST pipe and has been applied in the paper industry and for heat exchangers. To this date MFCs have mostly been investigated in lab scale experiment (Muddemann

et al. 2017).

3.2 Materials and Methods

DEPOSENS Biofilm Sensor

Experiments were conducted using DEPOSENS biofilm sensors manufactured by Lagotec GmbH (Magdeburg, Germany). The measurement principle of the sensor is displayed in Figure 3.1. It is based on the increase of the thermal resistance R_{th} of a pipe caused by deposits (e.g. biofilm) accumulating on the inner wall of the pipe (1). Deposits such as calcium carbonate ($\lambda_{\mathrm{CaCO_3}} = 2.6\mathrm{W/(m \times K)}$) or biofilms ($\lambda_{biofilm} = 0.6\mathrm{W/(m \times K)}$) (Characklis and Marshall 1990) have much lower thermal conductivities in relation to the thermal conductivity of the SST pipe wall ($\lambda_{SST} = 13.31\mathrm{W/(m \times K)}$). Therefore, the accumulation of such deposits impairs the heat transfer through the pipe wall and correlates proportionally to the thickness of the deposited layer. This phenomenon is commonly observed in heat exchangers and accounts a loss of heat transfer efficiency (Garcia et al. 2018).

$$R_{th} = \left(\frac{ln(r_{outer}) - ln(r_{inner})}{\lambda_{pipe}} + \frac{ln(r_{outer}) - ln(r_{inner})}{\lambda_{biofilm}} \right) \times \frac{1}{2\pi l} \tag{3.1}$$

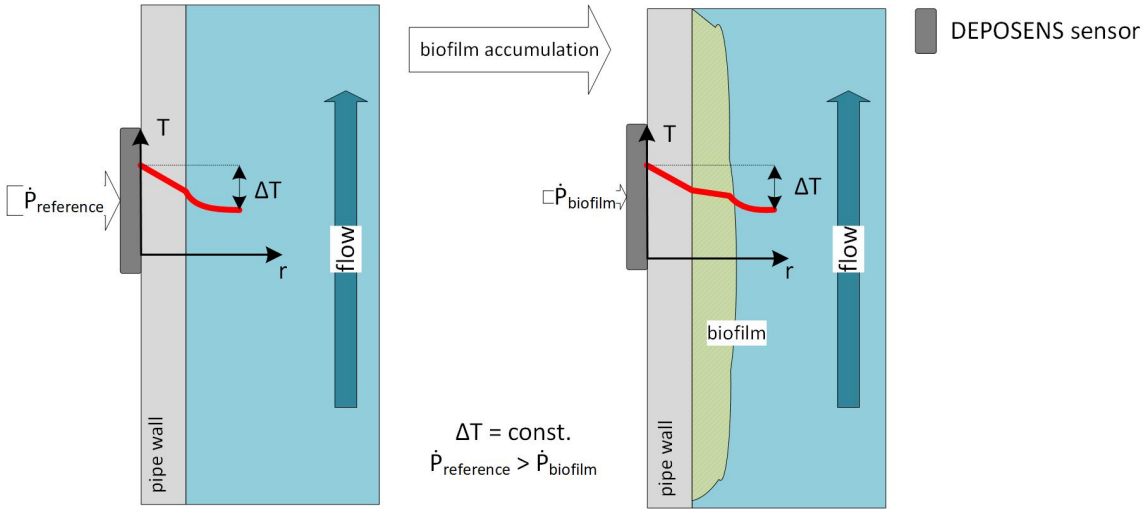

Figure 3.1: Measurement principle of the DEPOSENS biofilm sensor: the accumulated deposit (e.g. biofilm) increases the thermal resistance of the pipe wall. Consequently, a smaller heating power $\dot{P}$ is required to maintain the constant temperature difference ΔT.

The sensor (in Figure 3.1) consists of a heater and two temperature probes at different longitudinal

positions on the same board. One probe measures the pipe wall temperature at the heater and while the other measures the temperature of the medium through the pipe wall, respectively. The sensor board is glued to the outer pipe wall with a thermally conductive adhesive. Therefore, the biofilm development in the pipe is not manipulated by locally altered hydrodynamic conditions. A fixed temperature difference between heater and medium is set, thus a heat transfer from the heater to the medium is initiated. The thermal conductivity from the heater through the pipe wall to the medium is reduced proportionally to the accumulated deposits. Composition, thickness and density impact the thermal conductivity of the deposit layer. Consequently, decreasing the necessary amount of heating power to establish the set temperature difference ΔT between the two temperature probes. The resulting signal is given in reference to an initially deposit-free pipe. The flow rate must be maintained constant, as a change in the flow rate would increase or decrease the amount of heat extracted by the water, thereby altering the sensor measurement. The sensor is surrounded by a thermally isolating PUR-cover.

Experimental Setup and Biofilm Cultivation

Within this study temperature differential settings of ΔT=10 K, 5 K and 2 K were evaluated. An overview of all performed experiments with the respective parameters are listed in Table 3.1.

Table 3.1: Overview of experimental conditions (stainless steel pipe (SST) and graphite-polypropylene-compound pipe (C-PP) with a pipe diameter of d_i=25.4 mm, cultivation time up to 26 days

Q (L/min)	u (cm/s)	Re (-)	ΔT (K)	number of replicates used
			10	9
3.6	12	3000	5	8
			2	4

As previously mentioned, two different pipe materials have been tested: the commercially available 1.4571 SST pipe and an electrically conductive graphite-polypropylene-compound pipe (C-PP) (80 % graphite, 20 % polypropylene). This material has also been used by Muddemann et al. (2017) as an electrode material for bioelectrochemical systems. The SST pipes had a length of 250 mm whereas the C-PP pipes were 300 mm long with inner diameters of 25.4 mm. Since the thermal conductivity of the C-PP material ($\lambda_{C-PP} \approx 21\text{W/(m} \times \text{K)}$) and that of the SST material ($\lambda_{SST} = 13.31\text{W/(m} \times \text{K)}$)(Bogaard 1985) are in a similar magnitude, a good transferability of the biofilm sensor from the standard SST material to the C-PP material was expected. Experimental setup and biofilm cultivation The DEPOSENS biofilm sensors were installed into a recirculatory piping system with five parallelly operated pipes, containing each one SST pipe and one C-PP pipe in series. The experimental setup is shown in

Figure 3.2. Each pipe (inner diameter = 25.4 mm) was equipped with a magnetic gear pump (Niemzik PAT, Haan, Germany) re-circulating the cultivation medium. Biofilm cultivation was conducted under turbulent hydrodynamic conditions (Re = 3000; u = 12 cm/s). To ensure fully developed turbulent hydraulic conditions at the point of measurement of both sensors a run-in distance of 500 mm and a run-off distance of 400 mm was installed.

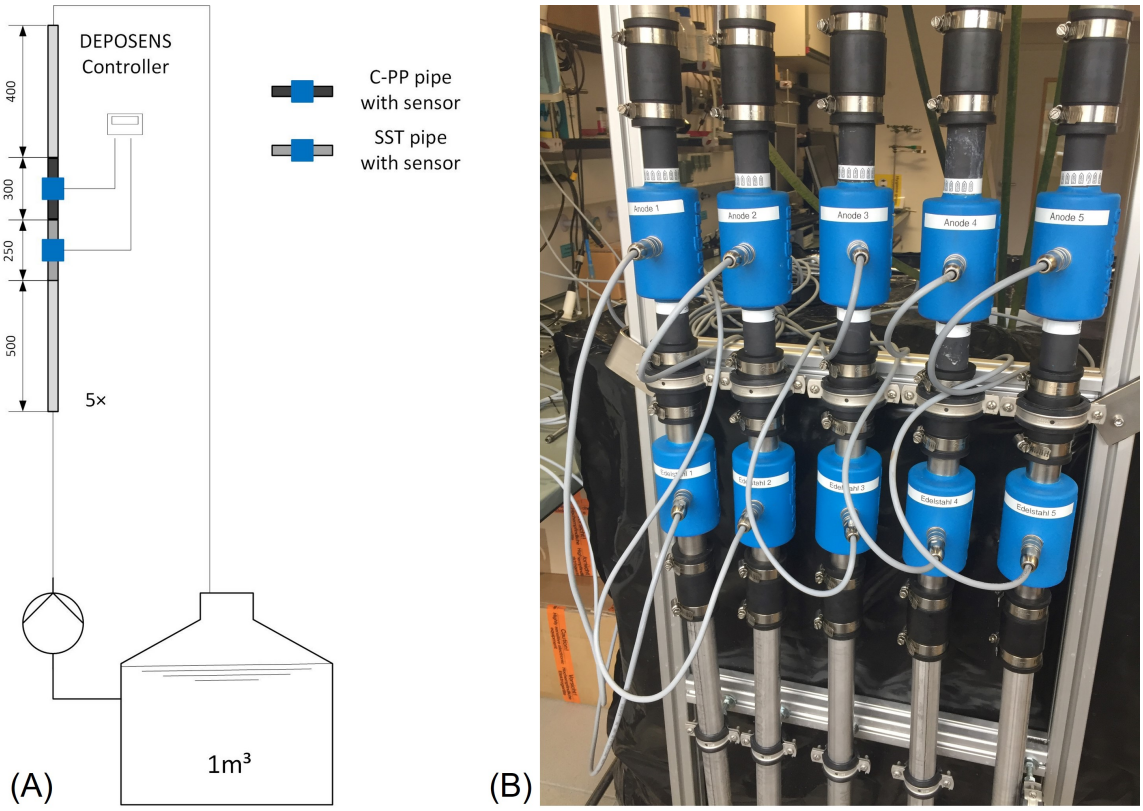

Figure 3.2: (A) The flow diagram of the experimental setup is shown. (B) A photograph of the lab-scale setup is shown with five parallelly operated pipes including each one SST pipe (bottom) and one C-PP pipe (top) with biofilm sensors installed in series.

After a 24 h inoculation phase with 120 L of activated sludge supernatant from the nearby wastewater treatment plant Bruchsal (Germany), the cultivation medium (V = 1000 L) was added to the recirculatory system. During the first 48 h of the experiments the average flow velocity was set to u = 6 cm/s (Re = 1500) to improve bacterial adhesion in the early stage of biofilm formation, due to the reduced shear stress (Duddridge et al. 1982). Afterwards, the average flow velocity was increased to u = 12cm/s (Re = 3000). For the cultivation medium a molar C:N:P-ratio was chosen at 100:10:1 as an optimal nutrient supply for biofilms growing under anaerobic conditions, as they can be found in the anodic chamber of microbial fuel cells. The cultivation medium (based on tap water) had an initial chemical oxygen demand (COD) of 200 mg/l and NH_4^+−N of 8.24 mg/l. Sodium acetate was chosen

as carbon source (c = 238.5 mg/L) and ammonium chloride (c = 31.1 mg/L) as nitrogen source. A K_2HPO_4/KH_2PO_4 mixture was used to buffer the cultivation medium at pH = 7.5. COD, ammonium and phosphate concentration were measured every 48 h with Hach-Lange vial tests, as well as the pH value and dissolved oxygen concentration. Substrate and nutrients were added to the cultivation medium when COD fell below 20 mg/l or NH_4^+-N concentration was less than 1 mg/l.

Gravimetric biofilm characterization

Following the cultivation of the biofilms in the pipes for up to 26 days until the DEPOSENS biofilm sensor signal did no longer indicate further biofilm accumulation, the pipes were sampled to determine the mean biofilm and biofilm density. The pipes were drained for 10 min in vertical position before weighing the pipes, in order to determine the wet mass. Afterwards the wet biofilm was scraped off the pipe for the determination of biofilm wet density as well as organic and inorganic fractions. When detachment of the deposits (biofilm) was visible during draining, the pipe was withdrawn. This was the case for two pairs of pipes at 10 K applied temperature difference and for one pipe pair at 5 K temperature difference.

The mean biofilm thickness was calculated, according to Equation 3.2 corresponding to the mass of the pipe in a clean state and with biofilm, respectively; A_{pipe} corresponds to the inner surface of the pipe.

$$\overline{L}_{F,grav} = \frac{m_{pipewithbiofilm} - m_{cleanpipe}}{A_{pipe}} \times \rho_{water} \qquad [\mu m] \tag{3.2}$$

The mean biofilm density $\overline{\rho}_{F,grav}$ was calculated according to Equation 3.3:

$$\overline{\rho}_{F,grav} = \frac{m_{F,dry}}{m_{F,wet}} \qquad [kg/m^3] \tag{3.3}$$

The fraction of inorganic compounds ϵ_{inorg} was determined according to Equation 3.4:

$$\epsilon_{inorg} = \frac{m_{F,dry} - m_{F,ash}}{m_{F,wet}} \qquad [kg/m^3] \tag{3.4}$$

Data Analysis and Quality Control

The aim of this study was to correlate the sensor signal with the morphology of the accumulated biofilm in the C-PP and SST pipes, respectively. After termination of the experiments the mean

biofilm thickness was correlated with the mean sensor signal of the final hour of the experiment (12 measurements). The data were plotted and a linear fit was applied to determine the sensitivity of the sensor. The linear fit was forced through the origin, because no biofilm was present at the time of sensor calibration. Resulting from the slope of the linear fit the sensitivity ($\Delta L_{F,grav}/\Delta D$) was determined. Due to the small sample size, Shapiro–Wilk and Kolmogorov–Smirnov tests were performed determining the distribution of the variables mean biofilm thickness, mean biofilm density and fraction of inorganic compounds for both the $\Delta T = 10\,K$ and $\Delta T = 5\,K$ settings. Followed by a Grubbs test to identify outliers in the data. More details are shown in Tables S2 and S3.

3.3 Results

Biofilm accumulation was monitored for 26 days until the DEPOSENS signal reached steady state. As biofilm accumulated the heat transfer resistance from the heater to the medium increased resulting in the recorded signal. Figure 3.3 shows the minimum, maximum and mean signal output of both sensors for all experiments ($n = 9$) at the standard temperature differential setting of $\Delta T = 10\,K$ (see Table 3.1). Due to the high measurement interval (5 min) a moving average of the sensor signal over a timespan of one day was applied. In Figure 3.3 can be seen, while the course of the sensor signal for both sensors is comparable, there is a difference in the intensity of the measured signal. Over the course of the experiment for both the biofilm sensor on the SST and the C-PP pipes the sensor signals increased steadily and reached a plateau after approx. day 15.

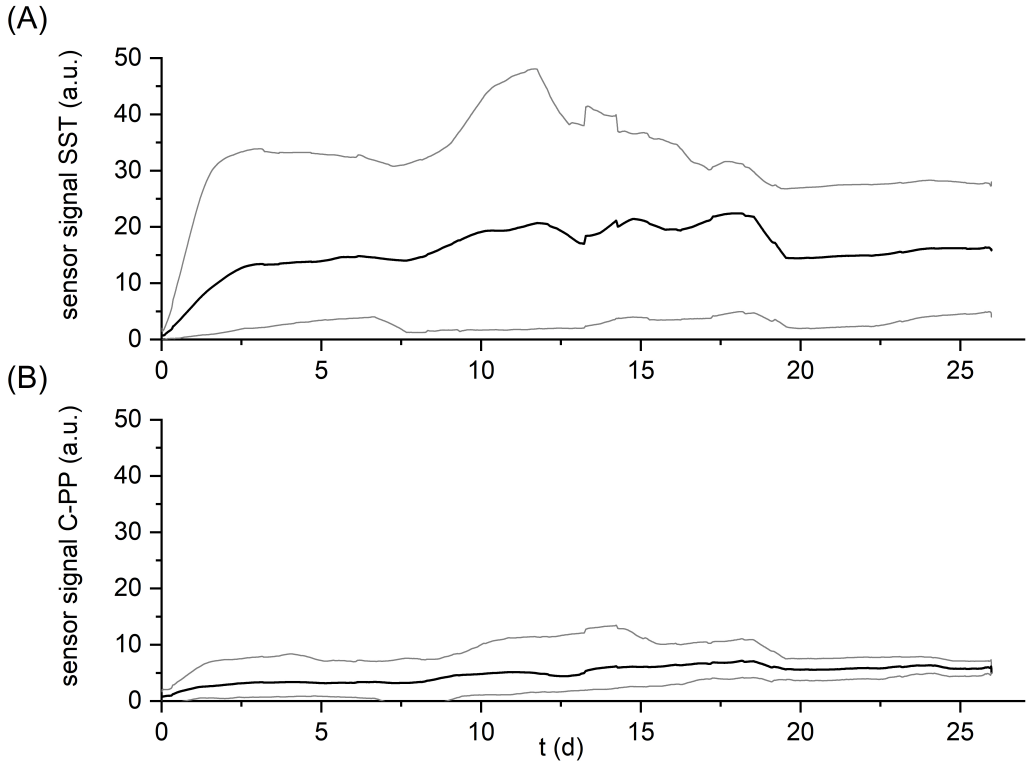

Figure 3.3: Development of the DEPOSENS sensor signal on the pipe made of SST (a) and the C-PP pipe (b) for all experiments (n=9) at standard conditions (ΔT=10 K). Due to the short measurement intervall (5 min) a moving average was applied over a timespan of one day. Day 0 remarks the end of inoculation at which the flow velocity was increased to 12 cm/s (Re = 3000). The thick black line displays the mean signal (in auxilliary units (a.u.)) for all experiments, while the light grey lines display the maximum or minimum signal from any of the sensors at the respective time.

As the flow velocity, was constant the signal was clearly attributed to the accumulation of deposits (e.g. biofilm) inside the pipes. Though, the mean value of the signal (black curves in the Figure 3.3a and 3.3b respectively) of the biofilm sensor on the SST pipe increased more rapidly and steeper to approx. 20 a.u. while the mean signal of the biofilm sensor on the C-PP pipe grew more steadily to approx. 6 a.u. for all the conducted experiments (n=9). It can be concluded that the biofilm sensor on the C-PP pipe is able to display a growth curve of the sensor signal, that follows a comparable trend to that of the sensor signal from the sensor applied to the SST pipe, despite being of smaller magnitude. Nevertheless, these findings indicate that the C-PP material is applicable to the sensor for the monitoring of a biofilm accumulation, in settings where SST as material cannot be applied (e.g. on electrodes of BES). For the purpose of sensor application, the sensitivity (biofilm accumulated per sensor signal a.u.) must be determined, to be able to translate the sensor signal value (measured in auxiliary unit (a.u.)) into the mean accumulated biofilm thickness $\bar{L}_F$ (µm). Assuming an equally

distributed biofilm accumulation over the total area of the respective pipes with integrated sensor the gravimetrically determined mean biofilm thickness represents the mean biofilm thickness at the point of the sensor measurement. Since the sensor signal is based on the heat transfer through the biofilm, not only the thickness of the accumulated biofilm, but also the biofilm density or fraction of organic and inorganic compounds affect the heat transfer, and thus the sensor signal. In Table 3.2 the gravimetrically determined biofilm characteristics in both pipe materials are summarized. A

Table 3.2: Comparison of the gravimetrically determined mean biofilm thickness, biofilm density and fraction of inorganic compounds for the experiments at the standard temperature difference $\Delta T = 10\,K$ ($n = 9$). Data control with the Grubbs test revealed one set of outliers for the mean biofilm density and the fraction of inorganic compounds for the SST material. This dataset was excluded. More details can be found in the Supplementary Materials Table S2 and S3.

Sensor/Pipe Material	Mean Biofilm Thickness $\overline{L}_F$ (µm)	Mean Biofilm Density (kg/m³)	Fraction of Inorganic Compounds (kg/m³)
C-PP	276 ± 102 (± 37 %)	24 ± 13 (± 54 %)	8 ± 5 (± 63%)
SST	170 ± 84 (± 49 %)	19 ± 8 (± 42 %)	9 ± 4 (± 44 %)

total of nine pairs of pipes with sensor have been investigated throughout the experiments at the standard temperature difference ΔT=10 K. At the end of the experiments, large variations of the gravimetrically determined biofilm characteristics (mean thickness, mean wet density and inorganic fraction) were observed among the individual pipes. Though the mean biofilm densities and inorganic fractions for both the C-PP pipes and SST pipes were similar. The mean biofilm thickness $\bar{L}_F$ on the other hand indicates the tendency to accumulate thicker biofilms in the C-PP pipe. The mean biofilm thickness in the C-PP pipe exceeded the biofilm thickness in the SST pipe by 63 %.

Despite the sensor signal of the biofilm sensor applied to the SST pipe exceeding the signal of the biofilm sensor on the C-PP pipe by a factor of 2-3 (Figure 3.3), on trend, less biofilm has accumulated in the SST pipes. This indicates different sensitivity of the sensors depending on the material of the pipe. For the determination of the sensor sensitivity, the mean gravimetrically determined biofilm was correlated to the mean signal of the final hour (12 measurements) of the respective sensor. This correlation is plotted in Figure 3.4. In advance to each experiment, the pipes were cleaned and a new reference for the sensor signal was set at 0. The linear fit function was forced through the origin, since at the start of the experiments with sensor signal 0 no biofilm was accumulated in the pipes. For the standard temperature difference ($\Delta T = 10\,K$), the coefficients of determination were R^2=0.82 for both materials. The sensitivity of the sensors was 11 µm/a.u. (on the SST pipe) and 53 µm/a.u. (on the C-PP pipe) respectively, showing that the sensitivity of the sensors applied to SST pipes exceed the

sensitivity of the sensors on C-PP pipes by almost a factor of 5.

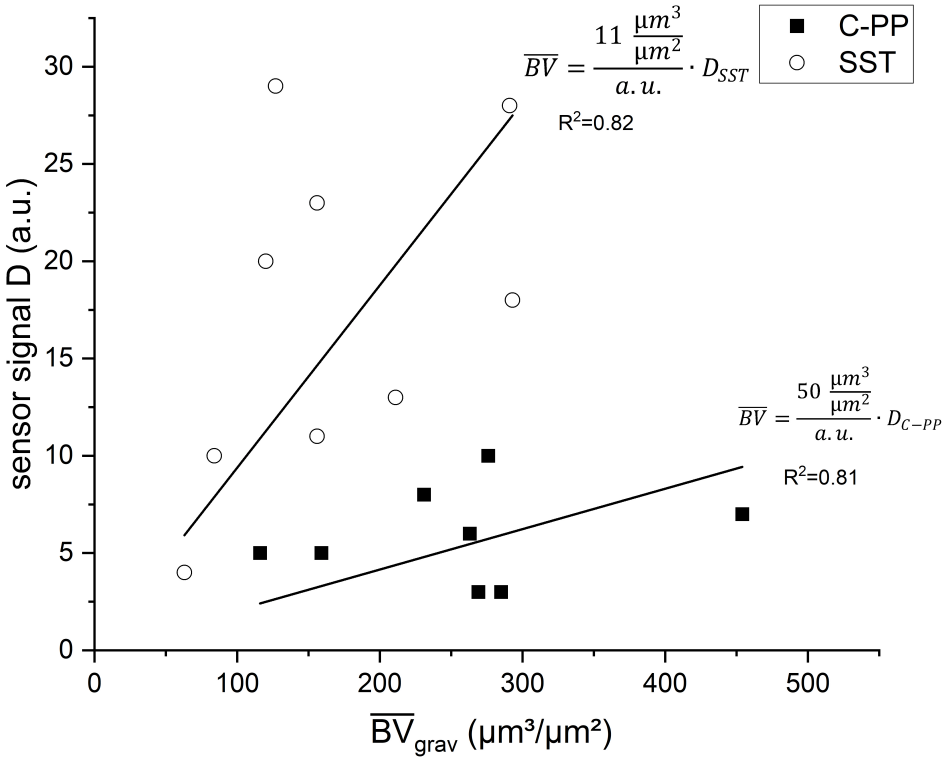

Figure 3.4: Correlation of the mean sensor signal of the final hour of the experiment (12 measurements) with the gravimetrically determined mean biofilm thickness accumulated in the SST and C-PP pipes with integrated biofilm sensors (ΔT=5 K). Assuming that no biofilm was accumulated in the pipe at the time of sensor calibration the linear correlation was forced through the origin

Influence of Setting of Temperature Difference

The experiments were repeated at multiple temperature differences ΔT of 2 K and 5 K. By applying lower temperature differences, the aim was to reduce the effect of longitudinal heat transfer along the pipe wall, which potentially interferes with the temperature measurement of the medium temperature sensor. A reduction of the longitudinal heat transfer could improve the sensitivity of the sensors. For the 2 K setting the biofilm accumulation was performed in a total of 4 sensor pairs. Biofilm accumulated well in both the SST and C-PP pipes with a mean biofilm thickness of 161 ± 52 µm and 302 ± 59 µm. These results are comparable to those obtained from the pipes with the 10 K setting of the sensors. As a consequence of the lower temperature difference between heater and medium, the sensitivity of sensors on both materials decreased, resulting in sensor readings in the range of

0 to 5 a.u. Within these narrow ranges of the sensors output signals at a 2 K setting, the biofilm accumulation in the pipe cannot be displayed well by the sensor anymore. The 2 K setting of the temperature difference was therefore not further investigated.

With the applied temperature difference of 5 K a total of eight pairs of pipes with biofilm sensors were investigated, showing a similar response of the sensor in terms of readings and sensor sensitivity compared to the 10 K setting. Figure 3.5 show the development of the sensor signal at ΔT=5 K. The resulting sensitivities of the biofilm sensors for all applied temperature differences are summarized in Table 3.3 for the SST pipes and C-PP pipes, respectively. Thereby, showing that the sensitivity did not improve by reducing the applied temperature difference to $\Delta T = 5\,K$.

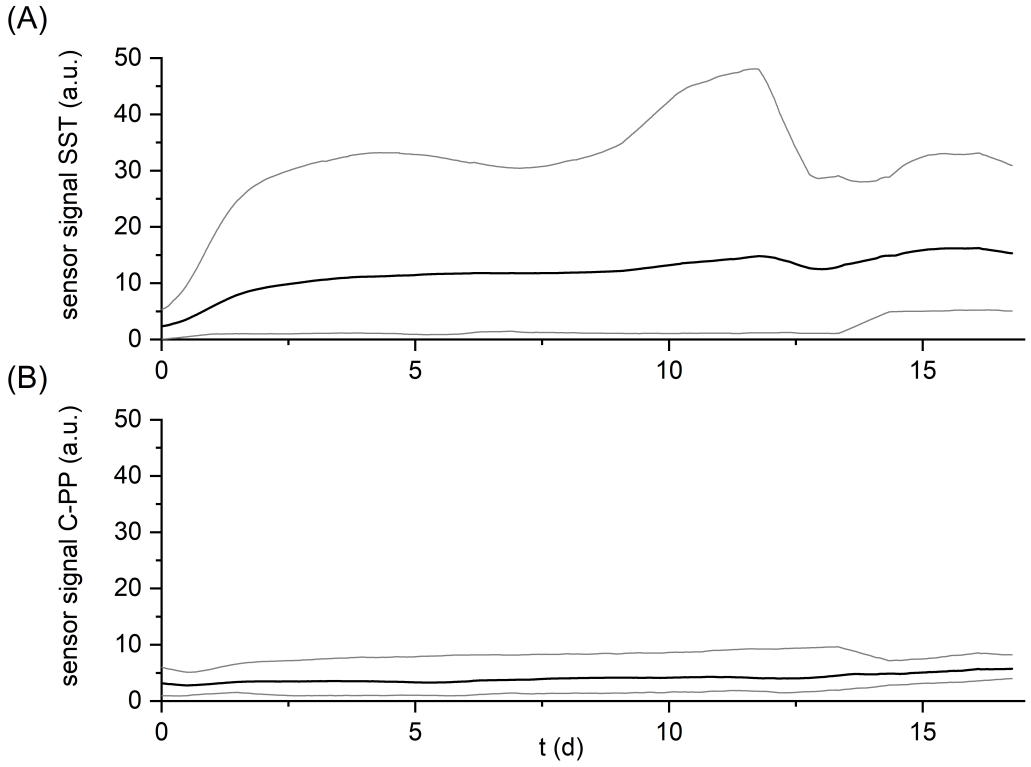

Figure 3.5: Development of the DEPOSENS sensor signal on the pipe made of SST (a) and the C-PP pipe (b) for all experiments (n=9) at standard conditions (ΔT=5 K). Day 0 marks the end of inoculation at which the flow velocity was increased to 12 cm/s. The thick black line displays the mean signal for all experiments, while the light grey lines display the maximum or minimum signal from any of the sensors at the respective time.

Table 3.3: Comparison of the sensor sensitivity for different applied temperature differences of the sensors

Temperature Difference (ΔT)	Mean Biofilm Thickness SST (µm)	Sensitivity SST (µm/a.u.)	Mean Biofilm Thickness C-PP (µm)	Sensitivity C-PP (µm/a.u.)
10	170 ± 84 (± 49 %)	11	276 ± 120 (± 54 %)	50
5	121 ± 29 (± 24 %)	9	193 ± 58 (± 30 %)	52
2	161 ± 52 (± 32 %)	77	302 ± 59 (± 20 %)	100

3.4 Discussion

As previously mentioned in reviews by Janknecht and Melo (2003) or Flemming (2003), biofilm monitoring devices require an on-line non-invasive mechanism to display the accumulation of biofilms within a technical system. The aim of this study was to investigate the application of the heat transfer DEPOSENS biofilm sensor on a carbonaceous-based electrode material (C-PP) for BES. The application on the C-PP material gives the major advantage to eliminate the influence of a different substratum to the growth of the biofilm, compared to the application of DEPOSENS sensor to SST. Due to its drawbacks SST is not commonly utilized as electrode material in microbial fuel cells (Kalathil et al. 2018; Yaqoob et al. 2020). Furthermore, with the application of the sensor to the C-PP material the sensor has the potential to be installed directly on the electrode. Thereby, the sensor is able to monitor the biofilm growing at the hydrodynamic pattern at the surface of the electrode. Usually, heat transfer biofilm sensors have been installed to a side-stream in an industrial plant (Janknecht and Melo 2003). Thereby, limiting the accuracy as the hydrodynamic pattern in the side stream may not be identical to the flow conditions inside the within the pipe or reactor. As reported by Recupido et al. (2020) the morphology of a biofilm is influenced by the hydrodynamic conditions, thus an installation of the sensor into a side stream of the plant may decreases the ability of the sensor signal to represent to actual situation on the electrode. Heat transfer biofilm sensor, like the DEPOSENS sensor, require constant flow conditions, since changing flow velocities of the medium impact the amount of heat withdrawn from the system. For example, a sudden increase of the flow rate results in a steep drop of the sensor signal, as the heater of the sensor requires more power to maintain the temperature difference ΔT. A higher power input to the heater corresponds to a thinner deposit layer and vice versa. Otherwise, a correction factor is necessary to compensate for

the different flow velocities. In the targeted application of the sensor on the fixed anode in a microbial fuel cell, constructed as a rotating disk reactor with rotating cathode (Dutta 2007), at the position of the sensor the flow velocity is constant, thereby diminishing the need for a correction factor. Other biofilm sensors that have been applied industrially based on electrochemical methods such as the electrochemical ALVIM sensor (Pavanello et al. 2011) or reported in literature based on impedimetric sensors (Pires et al. 2013), require an interface made of a different material that the material of an electrode in a BES. For the ALVIM sensor a SST electrode was used (Pavanello et al. 2011), while for the sensor reported by Pires et al. (2013) a gold electrode was the at the interface between biofilm and sensor. Thereby, the different properties of the substratum may diminish the immediacy of the sensor's measurement. Two of the major drawbacks generally reported by Janknecht und Melo (2003) - the low sensitivity of heat transfer sensors due to high uncertainties of the measurement of the wall temperature and the inability to distinguish between the compounds of the deposits - can be seen by the results reported in this study. Garcia et al. (2018) have reported in their research on the impact of biofilms on the heat transfer in seawater tubular heat exchangers that although the majority of the biofilm is composed of water ($0.6\,\mathrm{W/(m \times K)}$), its thermal conductivity may be increased by the concentration and nature of the solid composition of the biofilm. A decrease of the thermal conductivity was observed with a reduction of the solids present in the biofilm from $4.7\,\mathrm{mg/cm^2}$ to $2.2\,\mathrm{mg/cm^2}$. In comparison to the accumulated biofilms in this study, the biofilms ($0.32\,\mathrm{mg/cm^2}$) in the C-PP pipe and $0.36\,\mathrm{mg/cm^2}$ in the SST pipe at 10 K temperature difference) investigated by Garcia et al. (2018) showed a much higher concentration of dissolved solids in the biofilm. Otherwise, Characklis et al. (1981) have reported no significant correlation between the heat transfer coefficient of a biofilm and its density, while investigating biofilms with similar properties to the accumulated biofilms in this study. In this study, a linear correlation between the biofilm thickness and the sensor signal was assumed, which is in agreement with the reports of Janknecht und Melo (2003) stating, that a biofilm thickness of 10 µm will increase the overall thermal resistance by 1 – 1.5 %. The effects of biofilm density and inorganic fraction on the sensor's sensitivity could not be quantified. With the application of the sensor on the C-PP material a reduction of the sensor's sensitivity by approx. 80 % in comparison to that on the SST material was observed. This observation can largely be explained with the higher thermal conductivity of the C-PP material (21 $\mathrm{W/(m \times K)}$ vs. 13.3 $\mathrm{W/(m \times K)}$). As previously explained, two temperature probes are located in the sensor board on different longitudinal positions, measuring the temperature of the heater and the medium temperature respectively. The heat flow from the heater is not limited to across the pipe wall, but will also transfer heat longitudinally along the pipe wall to the medium temperature sensor. Due to the increased thermal conductivity of the C-PP material this

proportion of heat interferes with the temperature measurement to a greater scale than on the SST material. Thus, the sensitivity of the sensor on the C-PP material is diminished. To reduce the effect of the longitudinal heat transfer a smaller temperature difference would be preferential, but as shown in Table 3.3, the sensitivity of the sensor did not improve on either the C-PP or SST material with a lower temperature difference. In microbial fuel cells an optimal biofilm thickness must be established, to allow for efficient electron transfer and substrate access (Sun et al. 2016), since only live cells can contribute to the current generation. Ge and He (2016) have investigated the long-term performance of MFCs with wastewater and reported an unstable and deteriorating performance. To stabilize the MFC performance Islam and coworkers have therefore applied two different biofilm control mechanisms in microbial fuels cells with ultrasound (Islam et al. 2017) or with flushing (Islam et al. 2019), in order to control the biofilm thicknesses accumulated on the electrodes. The herein described sensor can be used as a trigger for the application biofilm control mechanisms. Several groups of researchers have investigated the biofilm thicknesses in MFCs. For the biofilm sensor to be an effective monitoring tool to trigger flushing procedures, the sensor must be able to identify the threshold of excessive biofilm thickness, that would alter the performance of a BES. Given the reported optimal biofilm thicknesses for microbial fuel cells of approx. 50 µm (Read et al. 2010; Semenec et al. 2015), the low sensitivity of the sensor, when applied to C-PP, may limit its ability to display the precise biofilm thickness on the electrode. An improvement of the sensitivity of the sensor on C-PP would be desirable.

3.5 Conclusion

The aim this study was to investigate the applicability of the DEPOSENS biofilm sensor on a graphite-polypropylene (C-PP) material in comparison to the standard SST pipe application, as a direct monitoring device of biofilms developing on the electrode of BES made from the same conductive composite material. This work has shown:

- the DEPOSENS biofilm sensor is able to identify an accumulation of biofilm on the inside of the pipe on both SST and C-PP corresponding to the thickness of the accumulated biofilm. The application of the sensor on C-PP is needed for electrodes made from C-PP to have comparable biofilm growth characteristics in pipe sensors and on electrodes in BES.
- the application on the C-PP material rather than the standard SST pipe resulted in a reduction of sensitivity of the sensor, despite fairly similar thermal characteristics of the materials. The

sensors on the C-PP material displayed a sensitivity (52 µm/a.u.) approximately 5-fold less than the sensor on SST (11 µm/a.u.)

- the reduced sensitivity limits the application of sensor on C-PP to technical systems with accumulating biofilm thicknesses of greater than 50 µm.
- the recommended operational settings for the application of the sensors with a temperature difference of minimum of 5 K.

4 In-situ biofilm monitoring using a heat transfer sensor: The impact of flow velocity in a pipe and planar system

Published as: Netsch, A.; Sen, S. Horn, H.; Wagner, M. In-situ biofilm monitoring using a heat transfer sensor: impact of flow velocity in pipe and planar system. Biosensors 2025, 15(2), 93. https://doi.org/10.3390/bios15020093

Abstract:

Industrially applied bioelectrochemical systems require long-term stable operation, and hence the control of biofilm accumulation on the electrodes. An optimized application of biofilm control mechanisms presupposes on-line, in-situ monitoring of the accumulated biofilm. Heat transfer sensors have successfully been integrated into industrial systems for on-line, non-invasive monitoring of biofilms. In this study, a mathematical model for the description of the sensitivity of a heat transfer biofilm sensor was developed incorporating hydrodynamic conditions of the fluid and the geometrical properties of the substratum. This model was experimentally validated at different flow velocities by integrating biofilm sensors into cylindrical pipes and planar meso-fluidic flow cells with a carbonaceous substratum. Dimensionless sensor readings were correlated with the mean biovolume measured gravimetrically, and optical coherence tomography was used to determine the sensors' sensitivity. The biofilm sensors applied in the planar flow cells revealed an increase in sensitivity by a factor of 6 compared to standard stainless steel pipes, as well as improved sensitivity at higher flow velocities.

4.1 Introduction

The field of applications for bioelectrochemical systems (BESs) is wide, utilizing various substrates/waste streams to produce value-added products, including energy-efficient wastewater treatment (Gude 2016) with the use of microbial fuel cells (MFCs) or production of hydrogen in microbial electrolysis cells (MECs) (Logan et al. 2006). Common denominator among BESs are electroactive biofilms growing on the anode coupling the metabolic conversion of organic substrates by the anodic bacteria with extracellular electron transfer (EET) to a solid electrode. The morphology of the electroactive biofilm on the

anode is of central importance to the efficiency and functionality of BESs (Read et al. 2010; Sun et al. 2016). The goal of upscaling BESs faces a number of challenges in the transition from laboratory-sized reactors to pilot- or industrial-scale systems (Dewan et al. 2008; Logan 2010), among which is mass transfer between the bulk phase and the electroactive biofilm at the electrode-biofilm interface. In detail, in an MFC, organic carbon diffuses towards the anode, where it is oxidized by EAB to CO_2 and H^+. The products need to diffuse out of the biofilm into the bulk phase. Otherwise, subsequent substrate gradients (Bonanni et al. 2013; Kato Marcus et al. 2007; Pereira et al. 2022c) or acidic pH environments (Bonanni et al. 2013; Franks et al. 2009) in the biofilm can limit or inhibit the EAB in their current production. An additional bottleneck of transport phenomena, which also hampers the anodic efficiency of BESs, is the reported limited distance of electron transfer from bacteria to the electrode, by cytochromes, electron shuttles/mediators, or conductive pili (Reguera 2018; Schröder 2007; Semenec et al. 2015). The combination of limitations deriving from EET distance and diffusion resistance along with the need for a high quantity of EAB, suggests an optimal biofilm thickness range for electroactive biofilms. Recently reported optimal biofilm thicknesses for electroactive model organisms range from a few μm for *Shewanella sp.* (Kitayama et al. 2017), to approx. 10 μm for *Desulfuromonas acetexigens* (Katuri et al. 2020) and up to 20-100 μm for *Geobacter sulfurreducens* (Pinck et al. 2020; Read et al. 2010; Reguera et al. 2006).

With the aim of long-term, stable bioelectrochemical processes in reactor systems utilizing waste streams, the control of biofilm thickness within an optimal range would support more efficient applications (Yang et al. 2021). Therefore, continuous monitoring of the state of the electroactive biofilm by means of on-line sensors on the anodes is desirable for the purpose of an industrially usable process control. Industrially applicable biofilm sensors require an on-line, in-situ and non-invasive characterization of the biofilm to provide relevant information regarding the biofilm's morphology (Pereira and Melo 2023). While most of the reported methods of biofilm monitoring have been investigated in lab-scale applications, a few industrially applicable sensors, including electrochemical sensors (e.g., ALVIM (Pavanello et al. 2011), BioGeorge (Bruijs et al. 2001), BIOX (Mollica and Cristiani 2003)), mechanical sensors (Solenis OnGuard (Bierganns and Beardwood 2017), optical sensors (OPTIQUAD (Strathmann et al. 2013)) and thermal sensors (DEPOSENS® (Netsch et al. 2021; Pratofiorito et al. 2024) are known. An extensive discussion of the advantages and limitations of the respective biofilm sensors or sensing methods can be found in the reviews by Janknecht and Melo (2003), Nivens et al.(1995) or Pereira and Melo (2023). Thermal biofilm sensors, which utilize the additional thermal resistance of deposits (such as biofouling or scaling) that increases linearly with accumulation in the

thickness of the deposits (Janknecht and Melo 2003), can be applied without intruding into the flow channel, and thereby are electrically isolated from the electrode. Limiting factors for thermal biofilm sensors have been reported to be a relatively low sensitivity, as well as a lack of differentiation of the chemical nature of the deposit (Janknecht and Melo 2003; Pereira and Melo 2023). Recently, Netsch et al. (2021, compare Chapter 3) demonstrated the applicability of heat transfer biofilm sensors to carbonaceous material, in this case, a compound material of graphite-polypropylene (C-PP). Electrodes of BES are commonly made from carbonaceous materials due to their good electrical conductivity, low costs and biocompatibility (Kalathil et al. 2018; Logan et al. 2006). However, the increased thermal conductivity of the substratum material in reference to the commercially available application, which was stainless steel (SST), resulted in a loss of sensitivity of 80 % compared to SST, thereby diminishing the precision of the substratum material's applicability to BESs, as the optimal thickness is in the range of 50-100 μm. Boukazia et al.(2020) showed an improvement in the metrological performance of a heat transfer sensor with steady thermal excitation, using a PVC scotch as a model deposit, when applied to a planar surface in comparison to a curved sensor surface intruding into the medium.

This study investigates the sensitivity of the DEPOSENS® heat transfer biofilm sensor, targeting an application in BES reactors. To achieve this, the sensor was applied to meso-fluidic flow cells with a planar C-PP substratum and a curved substratum in SST pipes (standard configuration), in which wastewater biofilms were cultivated at different flow velocities, as heat transfer is highly dependent on hydrodynamic conditions. The dimensionless output of the sensor (arbitrary units, a.u.) was correlated with the biofilm thickness through detailed analysis of biofilm parameters by means of optical coherence tomography (OCT), for the determination of the sensor sensitivity. This approach validates the sensor's capability to continuously monitor the biofilm thickness, and identifies the impact of substratum geometry and hydrodynamic conditions on the sensor's sensitivity.

4.2 Materials and Methods

Integration of biofilms sensors in meso-fluidic flow cells

Within this study, DEPOSENS® biofilm sensors manufactured by Lagotec GmbH (Magdeburg, Germany) were investigated. These sensors have been applied commercially to SST pipes for the monitoring of deposits in cooling systems, in the paper industry (www.lagotec.de accessed: 01.07.2024) or for membrane fouling surveillance (Pratofiorito et al. 2024). Netsch et al. (2021) have recently demonstrated the application of these sensors to other materials, in particular a carbon-polypropylene (C-PP)

compound material, despite its increased thermal conductivity ($\lambda_{C-PP} = 21\text{W}/(\text{m} \times \text{K})$) compared to that of SST ($\lambda_{SST} = 13.3\text{W}/(\text{m} \times \text{K})$). Briefly described, the working principal of the sensor is based on a reduction in the the heat transfer due to accumulating deposits with a lower thermal conductivity than the substratum, e.g., biofilms ($\lambda_{biofilm} = 0.6\text{W}/(\text{m} \times \text{K})$) (Characklis et al. 1981). A constant temperature difference (Δ T = 10 K) is set between the heater on the sensor and the medium temperature. The sensor signal results from the heat flux $\dot{Q}$, in reference to the heat flux at a zeroed value (clean state of the substratum) at a constant flow velocity. The measurement interval was five minutes. For a more detailed description of the sensor the authors refer to Netsch et al. (2021), compare Chapter 5.2). The biofilm sensors were applied to two identical pipes with an identical inner diameter (d_i= 25.4 mm), made of SST (l_{SST} = 250 mm) and C-PP (l_{C-PP} = 300 mm), respectively. Additionally, a meso-fluidic flow cell (see Figure 4.1), developed by Hackbarth et al. (2020) (flow channel: w × h = 40 × 9 mm²), made of polyoxymethylene (POM) was modified by integrating a C-PP substratum (l × w × h = 101 × 20 × 4 mm³). In all cases, the same biofilm sensor was installed on the outside of the SST pipes, the C-PP pipes and the bottom of the C-PP substratum in the flow cell, respectively, and enclosed by polyurethane (PUR) thermal insulation.

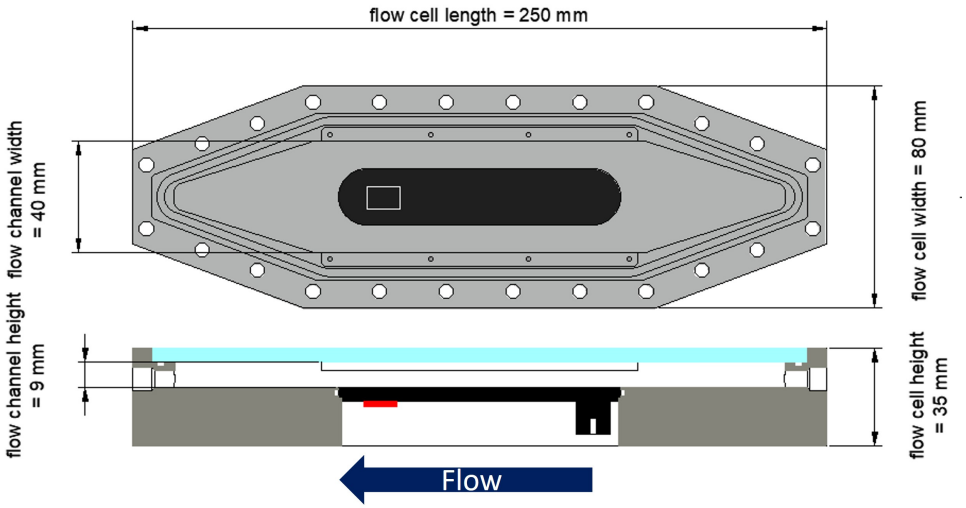

Figure 4.1: The top view and cross-section of the meso-fluidic flow cell. The red rectangle marks the OCT-imaging area (4 × 6 mm²) at the point of measurement of the biofilm sensor. In the cross-section, the biofilm sensor (red) is glued to the C-PP substratum (black) without contact with the bulk medium. The flow channel of the flow cell has a cross-section of 40 ×9 mm². The direction of flow is from right to left.

Experimental setup

The biofilm cultivation experiments were performed in a recirculatory system. Four parallel lines, each with an SST pipe biofilm sensor, a C-PP pipe biofilm sensor and a meso-fluidic flow cell with an integrated biofilm sensor, were installed in series on a mounting platform with a movable holder for the OCT probe. Each line was provided with a magnetic gear pump (Niemzik PAT, Haan, Germany) to recirculate the cultivation medium through the system from a 5 L reservoir. Before each experiment, all parts of the system were thoroughly cleaned manually, to remove any residual deposits. This was confirmed by means of OCT in the flow cells. Due to the cultivation of a wastewater biofilm, it was decided not to perform pre-experimental sterilization or operation under sterile conditions. Within this study, four different flow rates were investigated. Table 4.1 gives an overview of the performed experiments with their respective parameters and number of replicates.

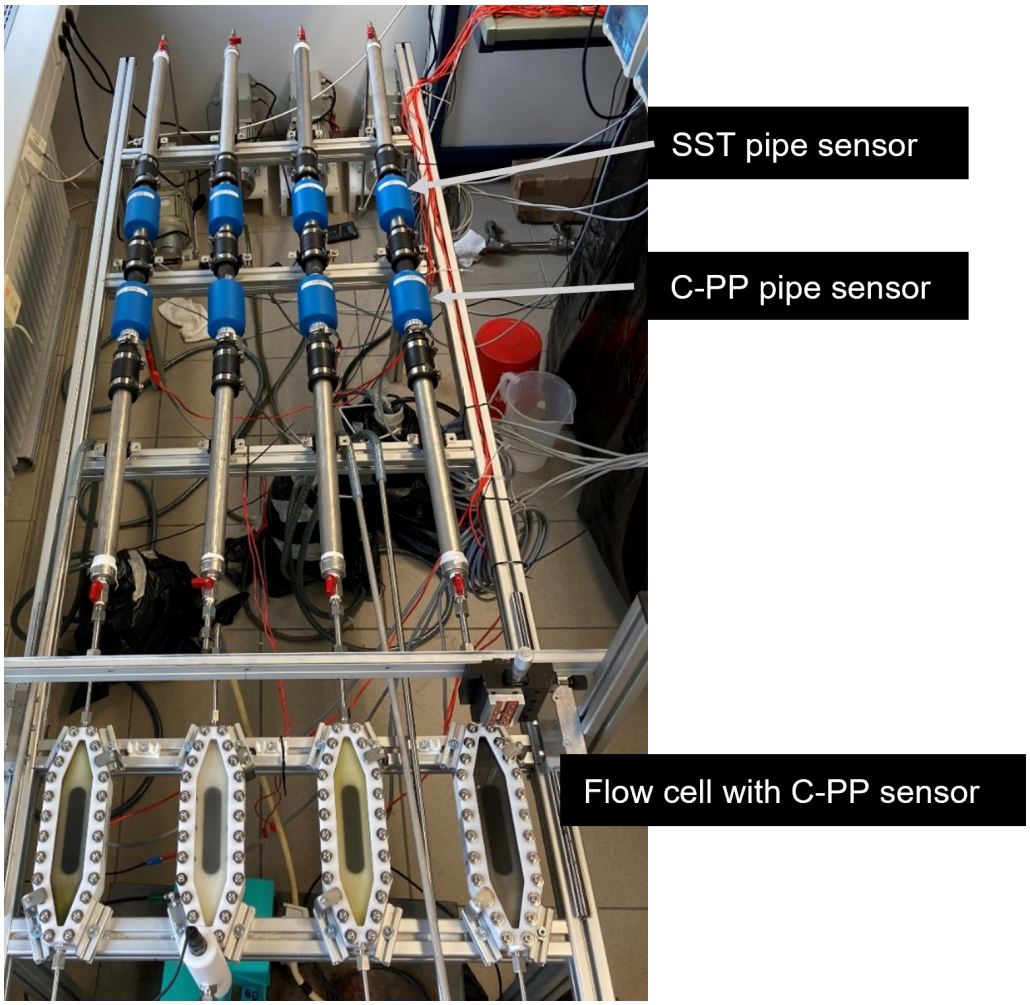

Figure 4.2: A photograph of the experimental setup showing the four replicates operated in parallel. Each replica was equipped with one SST pipe, one C-PP pipe and a meso-fluidic flow cell with a planar C-PP substratum. Biofilm sensors were integrated into each of the three systems (compare 4.1). The direction of flow was from top to bottom.

Table 4.1: An overview of the experimental conditions. Each replica consisted of one SST pipe sensor, one C-PP pipe sensor and a meso-fluidic flow cell with a biofilm sensor installed on the C-PP substratum

Experiment	Q (L/min)	$u_{flowcell}$ (cm/s)	u_{pipe} (cm/s)	no. of replicas n
1	1.94	9 (Re=1320)	6.39 (Re= 1620)	3
2	2.6	12 (Re=1980)	8.65 (Re= 2430)	14 (2a-d)
3	3.46	16 (Re=2350)	11.38 (Re= 2880)	3
4	5.83	27 (Re=3970)	19.18 (Re= 4850)	3

The parallel lines of the system were inoculated with 5 L of the supernatant of activated sludge from a local wastewater treatment plant. During the first 24 hours of inoculation the flow velocity was

reduced to 50 % of the experimental flow velocity. Subsequently, an artificial cultivation medium based on unsterile tap water, with a molar C:N:P ratio of 100:10:1 was added to the system to provide optimal conditions for anaerobic cultivation. Sodium acetate ($c = 238.46\,mg/L$) was provided as a carbon source ($COD = 200\,mg/L$), and ammonium chloride ($c(NH_4Cl) = 31.1\,mg/L$) as a nitrogen source. A phosphate buffer was used to adjust the medium pH to 7.2. The cultivation medium for each line was sampled individually on a regular basis, and COD, NH_4^+-N, $PO_4^{3-}-P$ were measured by Hach vial test. To avoid substrate limitations, the medium was replenished if its substrate contents decreased below a threshold of $COD < 20\,mg/L$ or $NH_4^+-N < 1\,mg/L$.

Biofilm quantification and structural parameters

Biofilm accumulation in the meso-fluidic flow cells was monitored daily by means of optical coherence tomography (OCT), for in-situ and non-invasive analysis of the biofilm's morphological parameters on the C-PP substratum. A GANYMEDE spectral domain OCT system (GAN610, Thorlabs GmbH, Dachau, Germany) with a LSM04 objective lens (Thorlabs GmbH, Dachau, Germany) was used. Three-dimensional OCT datasets (C-scans) were acquired at the position of the biofilm sensor (see Figure 4.1). The imaging volume was set to ($L \times W \times H = 4 \times 6 \times 2.14\ mm^3$) with pixel resolutions 8 μm/px laterally (xy-plane) and 2.06 μm/px axially. Biofilm parameters to describe the morphology were calculated using macros made in-house operated by ImageJ (version 1.54). Six parameters were determined for the characterization of the biofilm structure according to the works of Wagner and Horn (2017) and Murga et al. (1995). The mean biovolume $\overline{BV}_{OCT}$ is defined as the biofilm volume (sum of volume of all biofilm voxels) per imaging area A_{OCT}.

$$\overline{BV}_{OCT} = \frac{\sum voxel(1)}{A_{OCT}} \qquad (\mu m^3/\mu m^2) \tag{4.1}$$

The mean biofilm thickness $\overline{L}_{F,OCT}$ gives the height of the bulk biofilm interface to the substratum, thereby taking the cavities and spatial distribution of the biofilm into account. $L_{F,i}$ is the locally measured biofilm thickness, with N being the number of pixels.

$$\overline{L}_{F,OCT} = \frac{1}{N}\sum_{i=1}^{N} L_{F,i} \qquad (\mu m) \tag{4.2}$$

The substratum coverage (SC) describes the fraction of the imaging area A_{OCT} of the substratum that is covered with biofilm.

$$SC = \frac{A_{OCT} - A_{uncovered}}{A_{OCT}} \qquad (\%) \tag{4.3}$$

The intrinsic porosity Φ measures the volume fraction of voids (voxel(0)) beneath the bulk-biofilm interface $\overline{L}_{F,OCT}$.

$$\phi = \frac{\sum voxel(0)}{\overline{L}_{F,OCT} \times A_{OCT}} \qquad (\%) \tag{4.4}$$

Both the roughness (R_a) and roughness coefficient (R_a^*) describe the surface of the biofilm at the bulk biofilm interface. The roughness coefficient (R_a^*) normalizes the roughness (R_a) to the mean biofilm thickness $\overline{L}_F$ and allows for a comparison of biofilms with different thicknesses.

$$R_a = \frac{1}{N} \sum_{i=1}^{N} |L_{F,i} - \overline{L}_F| \qquad (\mu m) \tag{4.5}$$

$$R_a^* = \frac{1}{N} \sum_{i=1}^{N} \frac{|L_{F,i} - \overline{L}_F|}{\overline{L}_F} \qquad (-) \tag{4.6}$$

At the end of the experiment the biofilm in the pipe sensors (C-PP and SST) was measured gravimetrically. Pipe sensors were placed in a vertical position and water was released. Unbound water was drained for 10 min, before the biofilm was scraped off and weighed (KB 2400-2N, Kern & Sohn GmbH, Balingen, Germany). The mean biovolume distributed over the entire area of the pipe sensor ($A_{pipe,SST} = 126cm^2$, $A_{pipe,C-PP} = 152cm^2$) was determined according to Eq. 4.7, with $m_{biofilm}$ describing the mass of the wet biofilm and $\rho_{biofilm}$ describing the density of the biofilm.

$$\overline{BV}_{grav} = \frac{m_{biofilm}}{A_{pipe} \times \rho_{biofilm}} \qquad (\mu m^3/\mu m^2) \tag{4.7}$$

The gravimetrically determined biovolume can be compared to the biovolume obtained by means of OCT imaging in the meso-fluidic flow cells (Wagner and Horn 2017).

Determination of the sensor sensitivity and statistical analysis

The dimensionless sensor signal D, in arbitrary units (a.u.), requires transfer into a structural biofilm parameter (e.g., mean biovolume $\overline{BV}$) for its implementation as a biofilm monitoring device. The sensor signal was correlated with the mean biovolume acquired from OCT images to develop a linear calibration curve for the sensor in the flow cells at different velocities. The slopes of the calibration curves were inverted to describe the experimentally determined sensitivity of the sensor (compare Eq.4.8). A sensor sensitivity with a small value is the most desirable, as this will allow distinguish between biofilms of different thicknesses more precisely.

$$sensorsensitivity = \frac{1}{slope} = \frac{\Delta \overline{BV}_{grav}}{\Delta D} \qquad (\mu m^3/(\mu m^2 \times a.u.)) \tag{4.8}$$

To determine if triplicate experiments suffice for a precise calibration curve, the experiments 2 a-d (see Table 4.1) were performed as multiple replicates of one flow velocity ($u_{exp} = 12cm/s$), and statistically evaluated. A total of 14 individual flow cell runs were investigated. For a comparable evaluation of the resulting calibration curves, the 14 datasets from the replica experiments were randomly recombined as sets of three. This resulted in a total of 364 combination possibilities, for all of which linear regression curves were calculated, to identify the respective sensor sensitivity for each flow cell combination. The resulting sensor sensitivities were tested for outliers using Grubb's Test ($p < 0.05$), to determine the reproducibility of the sensor measurement. This allowed for a comparison with the experiments (1, 3 and 4), with three replicas each.

4.3 Results and Discussion

The integration of the biofilm sensor into the meso-fluidic flow cells allowed for continuous non-destructive monitoring of the biofilm accumulation $\overline{BV}_{OCT}$ on the substratum directly above the sensor. This allowed for a more detailed observation of the impact of accumulating biofilm on the sensor signal. On the contrary, the biofilm sensors incorporated into the SST and C-PP pipes only allowed for destructive gravimetrical determination of the biovolume $\overline{BV}_{grav}$ at the end of the experiment. For comparability with previous investigations presented by Netsch et al. (2021), in experiment 2 (compare Table 4.1), a linear flow velocity in the flow cell of $u_{exp} = 12cm/s$ (volumetric flow rate of 2.6 L/min) was investigated. Figure 4.3(A) shows the development of the signal of the sensors integrated into the flow cells on the C-PP substratum, as well as of the signals of the sensors integrated into the C-PP pipes and SST pipes.

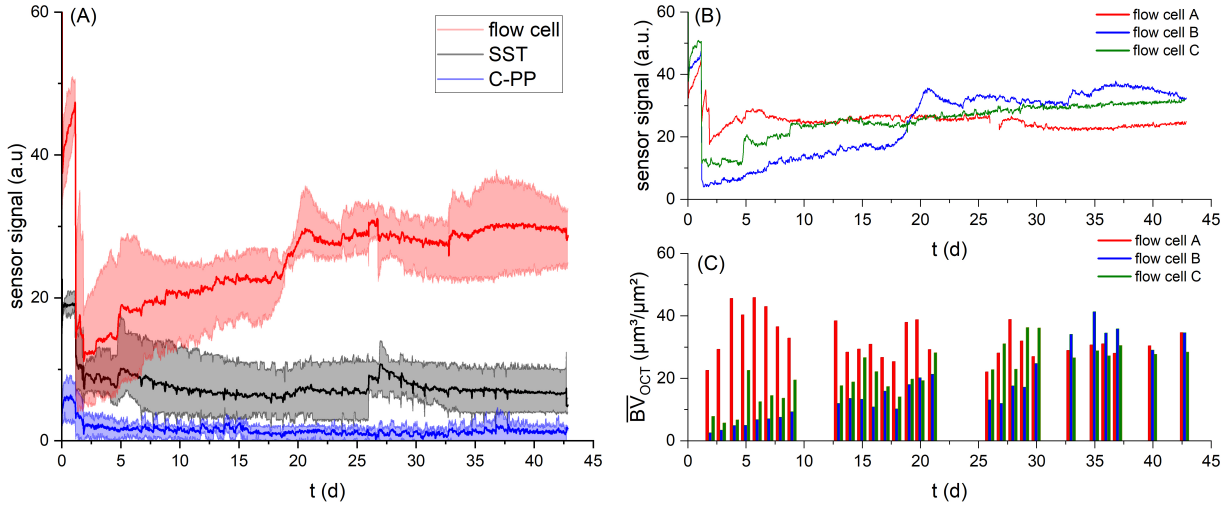

Figure 4.3: (A) The development of the biofilm sensor signal over the cultivation period (t = 45 d) for the sensors integrated in the flow cells (red), SST pipes (black) and C-PP pipes (blue) at a volumetric flow rate of 2.6 L/min (Exp. 2). The mean values are displayed as the thick curve between the minimum and maximum values for the triplicates, respectively. (B) The development of the sensor signal and (C) mean biovolume (bottom) individually for the three replicate flow cells (A-C) in Exp. 2.

A reduced flow velocity ($u_{inoc} = 0.5u_{exp}$) was applied during the inoculation to support bacterial attachment in the early stages of the experiment, resulting in an initially increased sensor signal compared to the reference value set for the clean sensors at u_{exp}. On Day 2, the sensor signals dropped from increased values during inoculation, with a reduced flow rate for all of the different sensor applications. The sensor signals at Day 2 of the cultivation displayed values of 5-18 a.u. for the flow cell sensor, 6-10 a.u. for the SST sensor and 0-4 a.u. for the C-PP sensor. Large differences in signal development in the flow cells could be seen due to variation in the initial biofilm accumulation at the imaging area in the flow cell, as flow cell A (red) showed the highest biovolume accumulation at Day 2 (23 $\mu m^3/\mu m^2$), followed by flow cell C (green) with 8 $\mu m^3/\mu m^2$ and flow cell B (blue) with 3 $\mu m^3/\mu m^2$. Over the course of the cultivation period (t = 45 d), the sensor signal of the flow cell sensors increased to a maximal signal of 27 - 35 a.u. in contrast to the sensor signals of the sensors integrated into the SST and C-PP pipes, where the sensor signals displayed no markable change from the initial value after the adjustment of the flow rate. The increase in the sensor signal of the flow cell sensors can be aligned with the increase in detected biovolume in the flow cells (Figure 4.3 B and C). With increasing biofilm growth, the deposits on the substratum above the sensor in the flow cells lead to an increase in the thermal resistance, measured by the biofilm sensor and converted to a sensor signal in arbitrary units (a.u.). At the end of the cultivation period OCT C-scans showed a

mean biovolume of 35 $\mu m^3/\mu m^2$ in flow cell A and B, while in flow cell C, a mean biovolume of 28 $\mu m^3/\mu m^2$ was measured. In contrast, the gravimetrical determination of the biofilm accumulated in the SST and C-PP pipes showed a mean biovolume of 118 - 173 $\mu m^3/\mu m^2$ and 261 - 379 $\mu m^3/\mu m^2$, respectively. The larger sensor signal measured by the sensors integrated into the flow cells at smaller accumulated biovolumes indicates an improved performance of the biofilm sensors applied on a planar substratum, compared to on the curved substrata of the SST and C-PP pipes.

Correlation of sensor signal with accumulated biovolume

For the application of the biofilm sensor as an on-line monitoring tool, its response to external factors needed to be characterized. Given the dependency on heat transfer of the hydrodynamic conditions in a system, an impact of flow velocity on sensor signal was expected. Figure 4.4 displays the correlation of the biofilm sensor signal with the biovolume quantified from OCT C-scans in the meso-fluidic flow cells.

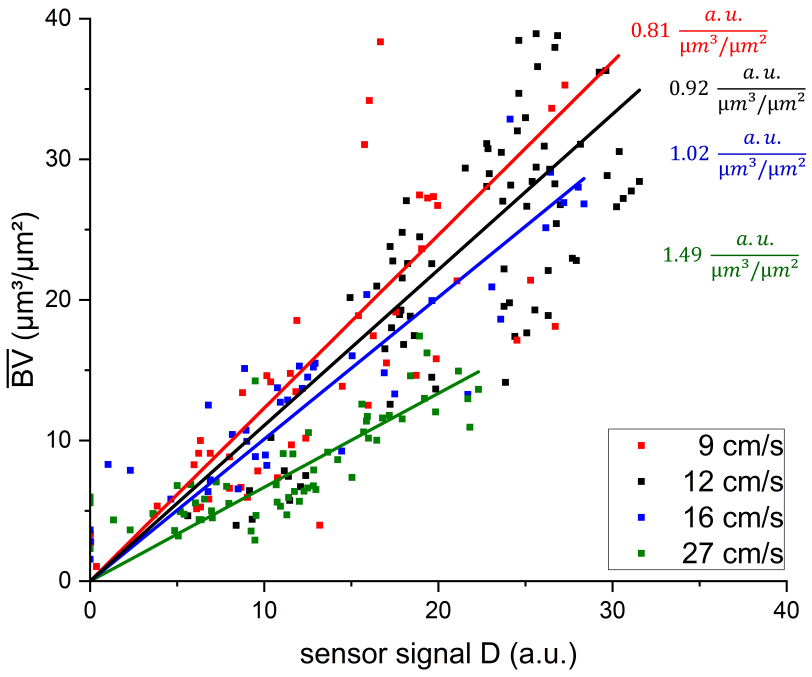

Figure 4.4: The correlation of the sensor signal with the accumulated mean biovolume ($\overline{BV}$) at the position of the sensor on the C-PP substratum in the meso-fluidic flow cells. C-scans with an imaging volume of 4 × 6 × 1 mm³ were analyzed. The acquired biovolume was correlated with the sensor signal at the time of imaging in the respective flow cell. The results of experiments 1-4 (compare Table 4.1) with a mean flow velocity of 9 cm/s (red), 12 cm/s (black), 16 cm/s (blue) and 27 cm/s (green) are shown. The slope of the correlation and coefficient of determination R^2 for the respective flow velocities are listed in Table 4.2.

For all investigated flow velocities, the correlation between accumulated biovolume and sensor signal can be described with a linear regression curve. The resulting inverse slope of the linear fit describes the sensitivity ($\mu m^3/(\mu m^2 \times a.u.)$) of the biofilm sensor with the applied flow velocity. The obtained slopes of the linear fit, sensitivities, and respective coefficients of determination (R^2) are listed in Table 4.2. All linear regression curves achieved coefficients of determination of 0.89 or higher, suggesting an improved correlation in comparison to the measurements performed with the C-PP or SST pipe sensors by Netsch et al. (2021), compare Figure 3.4), with an R^2 of 0.81 and 0.82, respectively. Due to the more frequent in-situ observation of biofilm accumulation by means of OCT directly at the point of sensor measurement in the flow cells, heterogeneous biofilm distribution on the substratum could be excluded as an influencing factor of the correlation between the sensor signal and biovolume. Furthermore, the biofilm sensors integrated into the flow cells responded with an improved sensitivity to biofilm accumulation in comparison to the pipe sensors. While the flow cell sensors identified the accumulated biofilm with a sensitivity in a range of 1 $\mu m^3/(\mu m^2 \times a.u.)$, the sensitivity of the SST pipe sensors was in the range of 10 $\mu m^3/(\mu m^2 \times a.u.)$. Generally, a lower value of sensitivity is more favorable for application of the sensor, due to more precise differentiation between different accumulated biovolumes. The determined sensor sensitivities in this study are in agreement with the sensitivity of 1.4 μm/a.u. found by Pratofiorito et al. (2024), when applying the same biofilm sensor to a planar SST substratum.

Table 4.2: The sensitivity of the biofilm sensor, calculated from the linear regression of the correlation between mean biovolume and sensor signal from experiments 1-4 (compare Table 4.1)

Flow velocity (cm/s)	Slope of linear correlation ($(\mu m^2 \times a.u.)/\mu m^3$)	Sensitivity ($\mu m^3/(\mu m^2 \times a.u.)$	Coefficient of determination R^2	Range of measured biovolume ($\mu m^3/\mu m^2$)
9	0.81	1.23	0.89	0-38
12	0.92	1.09	0.94	0-39
16	1.02	0.98	0.95	0-33
27	1.49	0.67	0.93	0-18

Additionally, the sensor sensitivity of the flow cell sensors displayed an improved response with increasing flow velocity, from 1.23 $\mu m^3/(\mu m^2 \times a.u.)$ at a flow velocity of 9 cm/s to 0.67 $\mu m^3/(\mu m^2 \times a.u.)$ at 27 cm/s. This suggests an impact of the hydrodynamic conditions on the ratio of the thermal resistance attributed to the biofilm (R_F), to the overall thermal resistance (R_{Total}) of the heat transfer. A higher ratio results in an improved sensitivity of the sensor. While the mean biovolume accumulated on the substratum a predominant effect on the thermal resistance, other morphological biofilm parameters

may have had an impact on the thermal resistance of the biofilm and resulted in a deviation from the linear correlation between sensor signal and biovolume.

Analysis of biofilm morphology

The structural biofilm parameters are highly dependent on the hydrodynamic conditions in the cultivation system. Local distribution of shear forces and nutrient supply can result in large deviations in the biofilm morphology. While the impact of hydrodynamic conditions on biofilm morphology is discussed extensively elsewhere (Tsagkari et al. 2022; Yang et al. 2019), within this study, it is of interest, as to whether variations in the morphological biofilm parameters other than the biovolume influence the heat transport from the heater to the bulk phase, and consequently, impact the sensor signal. Additional morphological biofilm parameters were calculated from the 3D-OCT scans. Their development over the cultivation period for the different investigated flow velocities are shown in Figure 4.5.

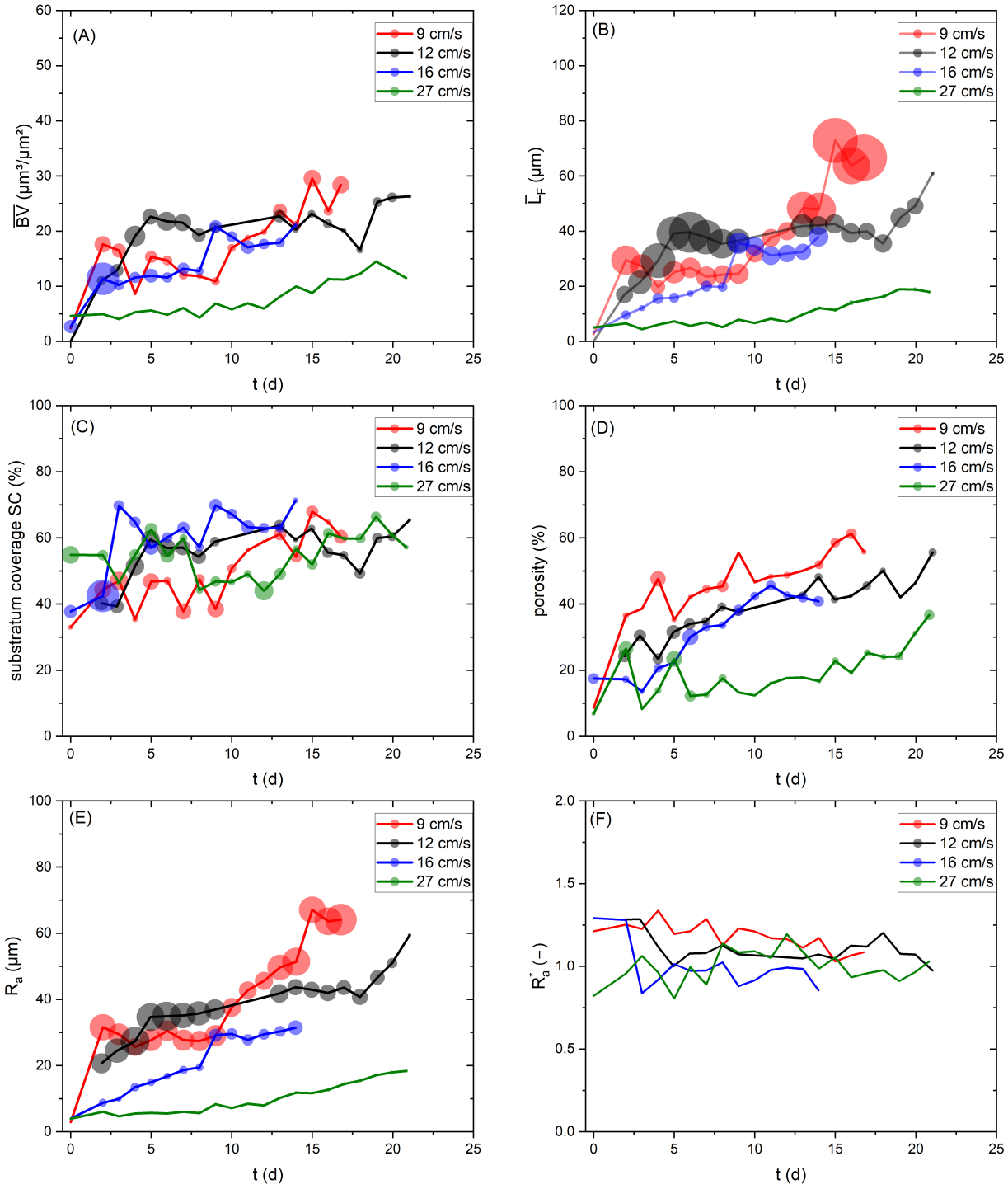

Figure 4.5: Development of biofilm parameters over a period of up to 21 days for the cultivation at the linear flow velocity of 9 -27 cm/s: (A) mean biovolume, (B) mean biofilm thickness, (C) substratum coverage, (D) porosity, (E) roughness and (F) roughness coefficient. The data points displayed are the mean value of triplicates of the respective experiments. The size of the data point shows the standard deviation.

Figure 4.5 (A) shows that the mean biovolume ($\overline{BV}$), and Figure 4.5 (B) shows that the mean biofilm thickness ($\overline{L}_F$), developed similarly for the investigated flow velocities (9, 12 and 16 cm/s), resulting in a mean biofilm thickness of approx. 40 μm on Day 14. In contrast, the accumulation of biofilm at 27 cm/s shows a reduced mean biofilm thickness of up to 12 μm after 20 days of cultivation. Higher shear forces led to a decreased initial setting of bacteria, as well as increased erosion, resulting in lower biofilm accumulation. Similarly, Stoodley et al. (1998) showed the development of thinner biofilms at higher flow velocities. On the contrary, Recupido et al. (2020) found the development of thicker biofilms with a higher flow velocity. The impact of biovolume on the sensor signal is displayed in Figure 4.4. Due to the similar trends of mean biofilm thickness and biovolume, the impact of both parameters on the sensor signal is expected to be identical. The substratum coverage (SC) describes the percentage of the area of the sensor covered by biofilm and thereby contributing towards a reduction in the overall thermal resistance. As shown in Figure 4.5 (C), a similar development for all experiments was found with, a substratum coverage in the range of 60-70 % after 14 days of cultivation. The roughness (R_a) (Figure 4.5 (E)) showed a decreasing trend, with the increasing flow velocity indicating a more heterogeneous biofilm structure at lower flow velocities. Exemplary height maps from the OCT-scans at different flow velocities, displaying the bulk biofilm interface, are presented in the Appendix (Figure A1). At Day 14 of the cultivation, roughness values of 51 μm (9 cm/s), 43 μm (12 cm/s), 31 μm (16 cm/s) and 12 μm (27 cm/s) were measured. A higher roughness of the biofilm correlates with an increased bulk biofilm surface area, which could enhance the heat transfer from the biofilm into the bulk phase. However, the roughness coefficient, describing the roughness related to the mean biofilm thickness, did not show a clear trend. For all velocities, the roughness coefficient (Figure 4.5 (F)) was approx. 1. The porosity of the biofilm was the highest at 9 cm/s, while 12 cm/s and 16 cm/s showed similar developments (see Figure 4.5 (D)). The lowest porosity was detected at 27 cm/s, indicating a more compressed biofilm, likely as a consequence of the higher shear forces. In porous materials, the effective thermal conductivity is a result of the difference between the thermal properties of the solid materials (EPS) and the fluid (water) in the pores. With increasing porosity, the effective thermal conductivity of the biofilm will converge towards the thermal properties of the fluid filling the pores (Liu and Zhao 2022; Smith et al. 2013). The thermal conductivity of a biofilm is commonly assumed to be between 0.5 and 0.7 W/(m $\times$ K) (Verein Deutscher Ingenieure 2013), as the biofilm usually consists of approx. 90 wt.-% water, with a thermal conductivity of 0.6 W/(m $\times$ K) (Characklis et al. 1981), although increases in the effective conductivity of biofilms have been measured depending on the solid content and chemical nature of the biomass. More compact biofilms with a higher fraction of inorganic compounds have increased thermal conductivities (Trueba et al. 2015). The variation in the

porosity measured in the meso-fluidic flow cells may have led to an increased or decreased thermal conductivity of the biofilm, thereby impacting the sensor signal. Generally, the analysis of biofilm parameters is susceptible to large variations and requires large sample sizes for statistically strong data interpretation. Gierl et al. (2020) extensively discussed the variability of biofilm parameters (including mean thickness, substratum coverage and porosity) with a series of 24 replicas, showing that individual data points might significantly deviate from the real statistical mean value. As displayed in Figure 4.5, the size of the data points shows the standard deviation of the calculated biofilm parameters. Notably, the largest variation was visible for the biofilm parameters $\overline{L}_F$ and R_a, while $\overline{BV}$ SC and porosity displayed decreased fluctuation. Moreover, the roughness coefficient was not subject to large variations. Recupido et al. (2020) similarly noted, that roughness coefficient showed the smallest variation for different hydrodynamic conditions and among replicas. It seems that the variation in the biofilm parameters decreased with increasing flow velocity, as the highest flow velocity displayed the lowest fluctuation. In conclusion, we infer that fluctuations in morphological biofilm parameters may cause a deviation from the linear correlation between mean biovolume and heat transfer resistance, thus impacting the sensor signal.

Reproducibility of results

Taking the fluctuation of the morphological biofilm parameters into account, it is required to analyze, how well the correlation of the sensor reading with the mean biovolume can be reproduced. To investigate the reproducibility, experiment 2 ($u_{exp} = 12\,cm/s$) was repeated with a total number of investigated flow cell replicas of n = 14. For a comparison with the experiment 1 ($u_{exp} = 9\,cm/s$), 3 ($u_{exp} = 16\,cm/s$) and 4 ($u_{exp} = 27\,cm/s$) performed as triplicates, the 14 datasets acquired from experiment 2 were randomly recombined in sets of three, as they were equal probable for sensor measurement. For the resulting 364 combined datasets, the sensor sensitivity was calculated according to the linear correlation of the sensor signal with the mean biovolume. Figure 4.6 (left) shows the resulting sensitivities derived from the linear regression of flow cell combinations.

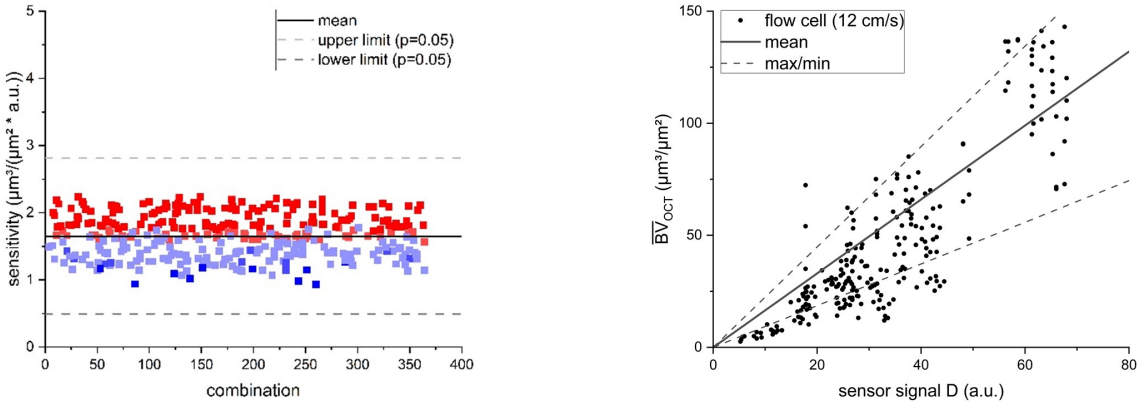

Figure 4.6: (left) The calculated sensor sensitivities for the recombined flow cell combinations (triplicates) at a linear flow velocity of u = 12 cm/s. The datapoints are colored and displayed as a heatmap, according to the maximum range of the mean biovolume. Warmer colored points (red) include a higher maximum mean biovolume than colder colored points (blue). The gray dashed lines indicates the lower and upper limit of deviation from the mean value (p=0.05). (right) A display of all data points from the 14 investigated flow cells, with the mean derived sensitivity, as well as the maximum and minimum sensitivity calculated, from the triplicate recombination.

The mean sensor sensitivity obtained from the 364 combinations revealed a less favorable sensitivity of 1.65 ± 0.31 $\mu m^3/(\mu m^2 \times a.u)$ compared to the initially obtained sensitivity of the initial triplicate of 1.09 $\mu m^3/(\mu m^2 \times a.u.)$ (see Table 4.2). With the larger sample size (n=14), an increased fluctuation of the mean biovolume to sensor signal ratio was visible, deviating from the linear regression curve. This could indicate the influence of other morphological biofilm parameters varying over the course of the biofilm cultivation (see Figure 4.5). Nevertheless, the sensitivity of the recombined triplicates showed good reproducibility, as the performance of Grubb's test for outliers revealed no significant ($p<0.05$) outliers. This supports a sufficiently precise determination of the sensor sensitivity with triplicate experiments. Additionally, the larger sample size enabled the measurement of an increased range of biofilm thicknesses displayed in the 14 flow cells. Biofilms with a larger mean biovolume range of up to 150 $\mu m^3/\mu m^2$ were cultivated in the flow cells. In Figure 4.6 (left) the datapoints are colored and displayed as a heatmap, according to the range of mean biovolume included in the dataset. Larger ranges of mean biovolume are displayed with a warmer color (red), while a smaller range of biovolume is displayed with a colder color (blue). The heat map shows that triplicate combinations with a smaller range of the mean biovolume resulted in an improved sensitivity compared to those triplicates including larger ranges of mean biovolumes. For example, the triplicate combination with the "worst" sensitivity of 2.24 $\mu m^3/(\mu m^2 \times a.u.)$ included a mean biovolume of up to 156 $\mu m^3/\mu m^2$,

while the triplicate combination with the "best" sensitivity of 0.93 $\mu m^3/(\mu m^2 \times$a.u.) only had a mean biovolume range of up to 41 $\mu m^3/\mu m^2$. This hints to a deviation from the linear correlation between mean biovolume and sensor signal for thicker biofilms, although the linear regression showed an R^2 of 0.9 for a mean biovolume range of up to 150 $\mu m^3/\mu m^2$ (see Figure 4.6 (right)).

Mathematical model for calculation of sensor sensitivity

The results obtained in this study indicate that the sensitivity of the heat transfer biofilm sensor is dependent on the hydrodynamic conditions and the geometrical properties of the substratum to which the sensor is attached. Therefore, a mathematical model to predict the sensitivity of the sensor, based on the hydrodynamic and geometrical properties, was developed. Equations and terminology for the model were taken from the VDI Heat Atlas (Verein Deutscher Ingenieure 2013). Assuming a homogeneous distribution of the biofilm with a porosity = 0 % and full substratum coverage (SC = 100 %) of the measurement area of the sensor, the mean biovolume ($\overline{BV}$) equals the biofilm thickness ($\overline{L}_F$). As the sensor measures the change in the required heat input $\dot{Q}$ to maintain a constant temperature difference (ΔT) between the temperature of the medium and of the heater, the required heat input is calculated according to Eq. 4.9. With increasing biofilm accumulation, the total thermal resistance for the heat transfer increases, thereby, the sensitivity of the sensor can be related to the change in the thermal resistance of the biofilm (R_F) as a fraction of the total thermal resistance (R_{Total}) (Eq.4.10). In Eq. 4.11, the calculation of the different fractions of the thermal resistance for the planar geometry of the meso-fluidic flow cells is displayed. The total thermal resistance comprises of the thermal resistance of the substratum ($R_{substratum}$), calculated from the thickness of the substratum s_{C-PP} and its thermal conductivity λ_{C-PP}, of the biofilm (R_F), from the mean biovolume and its thermal conductivity λ_F, as well as of the thermal boundary layer (R_{tbl}). The heat transfer coefficient α can be determined from the Nusselt number, which is dependent on the hydrodynamic conditions (compare Table 4.1). Given the long measurement interval of the sensor (5 min) the temporal fluctuations of the hydrodynamic conditions could be averaged for the model. More details on the calculation of the individual terms of the thermal resistance for the different geometric properties and hydrodynamic conditions can be found in Appendix B.

$$\dot{Q} = \frac{\Delta T}{R_{Total}} \tag{4.9}$$

$$\text{sensor sensitivity} = \frac{\Delta\overline{BV}}{\Delta\frac{R_F}{R_{Total}}} \tag{4.10}$$

$$\text{with } R_{Total} = \frac{1}{A_{sensor}} \times \left(\underbrace{\frac{s_{C-PP}}{\lambda_{C-PP}}}_{R_{substratum}} + \underbrace{\frac{\overline{BV}}{\lambda_F}}_{R_F} + \underbrace{\frac{1}{\alpha}}_{R_{tbl}} \right) \tag{4.11}$$

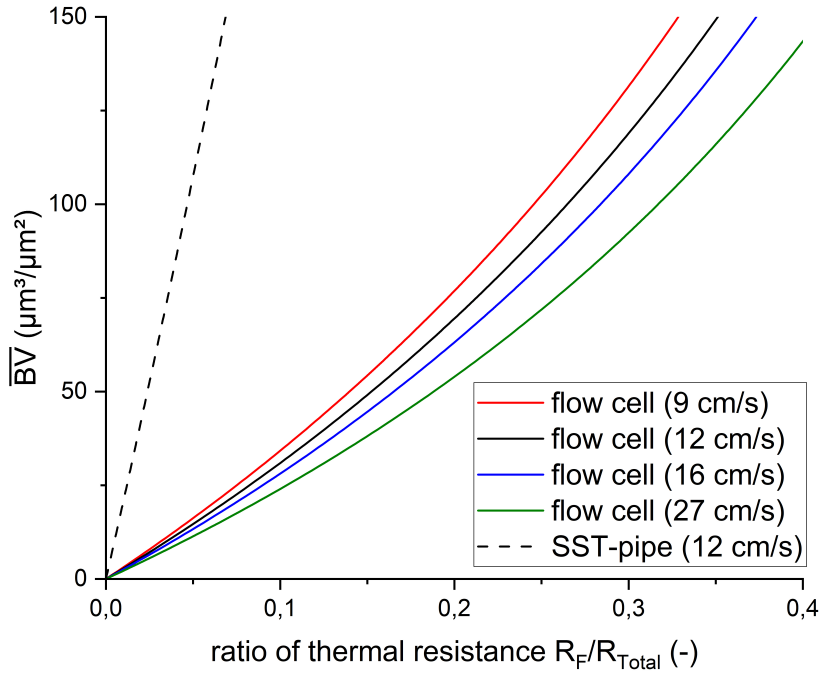

Figure 4.7: Theoretical calculation of the ratio of the biofilm's thermal resistance compared to the total thermal resistance of the system. The calculation was performed for the SST pipe with a linear flow velocity of 12 cm/s, and for the four investigated flow velocities (9-27 cm/s) in the meso-fluidic flow cells with a C-PP substratum. Details of the calculation are provided in the Appendix B.

Figure 4.7 shows the development of the ratio of thermal resistance of the biofilm to the total thermal resistance for a biovolume of up to 150 $\mu m^3/\mu m^2$, based on the mathematical model. The model was applied for the meso-fluidic flow cells with a planar C-PP substratum for the mean flow velocities of 9, 12, 16 and 27 cm/s, respectively, as well as for the SST-pipe with the mean flow velocity of 12 cm/s, investigated by Netsch et al. (2021), compare Chapter 3). The steepness of the resulting curve relates to the sensitivity of the sensor, whereas a flatter gradient is more desirable for sensor application since

it displays a higher resolution for the R_F/R_{total} ratio per increment of biofilm thickness. For example, a 100 μm thick biofilm contributes to a total thermal resistance of 4.7 % in the SST pipe (u = 12 cm/s), while for the planar flow cells with a C-PP substratum, the fraction was 26.5 % for the mean flow velocity of 12 cm/s, showing an approx. 6-fold increase. In comparison, the sensor applied to the SST-pipe achieved a sensitivity of 11 $\mu m^3/(\mu m^2 \times$a.u.), as the sensor integrated into the flow cell had a mean sensitivity of 1.65 $\mu m^3/(\mu m^2 \times$a.u.), resulting also an approx. 6-fold increase. Similarly to this study, Boukazia et al. (2020) investigated geometrical impacts on heat flux by simulating biofouling with different layer thicknesses of PVC scotch on a flat Micro-Electro-Mechanical-System (MEMS) sensor and a cylindrical intrusive sensor. Although the sensitivity of the sensor was not reported, they found strong differences in thermal resistance due to the geometry of the sensor application with lower limits of detection for the flat MEMS structure. Additionally, the difference in the sensor sensitivity for the different hydrodynamic conditions in the flow cells can be seen in Figure 4.7. With increasing flow velocity, the convective fraction of the thermal resistance (R_{tbl}) decreases with a thinner thermal and hydrodynamic boundary layer. Consequently, with decreasing total thermal resistance the impact of accumulating biofilm increases and thereby the sensor sensitivity increases. Furthermore, the regression curves generally show a linear trend for the correlation between the sensor signal and biofilm accumulation (Figure 4.4). The theoretical calculation suggests a non-linear correlation of the sensor sensitivity thickness of the biofilm. The maximum biofilm thickness that was measured in the flow cells were approx. 150 μm. Within this range of biofilm thickness the deviation of the theoretical model from the linear trend is negligible. A linear fit of the theoretical model results for the range of biofilm thickness results in an R^2 of 0.99. The non-linearity of the sensor sensitivity is corroborated by Filladreau et al. (2010), who state that the temperature difference will asymptotically reach a constant value with increasing biofilm thickness when applying a constant heat flux (compare to converted Eq.4.9).

Comparison with available industrial biofilm sensors

Biofilm sensors must be well chosen for their target application to provide relevant information about the state of the biofilm (Pereira and Melo 2023). In the case of BESs, though, commercially available electrochemical biofilm monitoring devices (e.g., ALVIM (Pavanello et al. 2011), BIOX (Mollica and Cristiani 2003), or BioGeorge (Bruijs et al. 2001)) may have a lower limit of detection, already measuring the initial bacterial layer ($\approx$ 1% substratum coverage (Pavanello et al. 2011), they are limited in their upper limit of detection to a few μm. Therefore, they are able to provide information on the substratum coverage but are not suitable for continuous monitoring of multilayer biofilms.

In contrast, the heat transfer biofilm sensor in this study lacks the ability to identify an individual biofilm parameter such as substratum coverage. Optical measurement methods on the other hand meet the requirements for the measurement range of biofilm thickness, being able to detect medium-thick biofilms (approx. 100 μm). For example, the commercially available sensor OPTIQUAD (Strathmann et al. 2013), can detect thin biofilms of 1-50 μm, while optical coherence tomography (OCT) can detect biofilms in the thickness range of several 100 μm, with a resolution of a few μm (Wagner and Horn 2017). Additionally, more sophisticated optical detection methods (e.g., OCT) allow for more detailed analysis of biofilm morphology, while heat transfer sensors are limited to a single biofilm parameter (e.g., mean biovolume). Nevertheless, optical methods require the installation of an optical window, which might be feasible in lab-scale reactors, though with larger increasingly complex reactors, the integration of optical windows that enable a representative measurement of the biofilm at the point of interest would be troublesome. Vibration-based biofilm sensors might present an equally viable option for biofilm monitoring compared to the heat transfer sensor presented in this study. The ultrasound-based Solenis OnGuard 3B analyzer was found to be able to measure medium-thick biofilms of up to 200 μm, with an accuracy of down to 5 μm. However, the thin biofilms in the early growth phase could only be detected with a coupled heat transfer sensor (Bierganns and Beardwood 2017). A similar detection range of 50 - 250 μm was reported by Maurício et al. (2013) for their ultrasound-based sensor, though at an inferior limit of detection to the heat transfer sensor. Comparison with other commercially available biofilm sensors for industrial-scale application supports the use of heat transfer based sensors for the monitoring of biofilms on the electrodes of BESs. Although, in this study, the wastewater biofilm accumulated in the meso-fluidic flow cells was non-electroactive, the determined sensitivities of the sensor should be transferable, as there is no expected difference in this biofilm's thermal properties compared to those of an electroactive biofilm. With the attachment of the biofilm sensor to a planar carbonaceous substratum, the high sensitivity would allow for detailed monitoring within the optimal range of biofilm thickness (approx. up to 100 μm). It should be noted, given the dependency of the sensor sensitivity found in this study, that coupling of the sensor with flow meters is required.

4.4 Conclusions

Within this study the main objective was to characterize the impact of different hydrodynamic conditions on the sensitivity of the heat transfer biofilm sensor as well as the application of the sensor

to planar and curved substratum geometries. The integration of heat transfer biofilm sensor into meso-fluidic flow cells allowed for non-invasive calibration of the dimensionless sensor signal (a.u.) to biofilm accumulation ($\mu m^3/\mu m^2$) by means of OCT. Biofilm morphology and sensor signal were measured with a high temporal resolution (1-2 days) at different biofilm ages throughout the experiments. The development of the sensor signal increased with accumulating biofilm at the point of measurement of the sensor, due to the increased thermal resistance of the biofilm. The key findings can be summarized as follows:

- While the predominant effect on the thermal resistance of the biofilm, and thus on sensor signal development, was identified as the mean biofilm thickness or biovolume, other morphological parameters (porosity, roughness, substratum coverage) might have had an impact on the thermal properties of the biofilm. This could have led to a scattering of the biofilm thickness to sensor signal ratio along a quasi-linear correlation.
- The sensitivity of the sensors in the flow cells improved due to the flat geometry of the C-PP substratum, despite the higher thermal conductivity of the C-PP material. The sensitivity was 6 times better than the sensor sensitivity in the SST-pipe, and 30 times better than in the C-PP pipe.
- With increased flow velocities (more turbulent hydrodynamic conditions) the sensitivity of the sensor increased from 1.26 $\mu m^3/(\mu m^2 \times$a.u.) at 9 cm/s to 0.67 $\mu m^3/(\mu m^2 \times$a.u.) at 27 cm/, due to the decreased thickness of the thermal boundary layer. For precise conversion, the heat transfer biofilm sensor signal must be coupled with a measurement of the flow velocity.
- A mathematical model of the biofilm sensor, incorporating hydrodynamic effects and geometrical heat transfer regimes, was developed. The model can support the prediction of the sensitivity of biofilm sensors for various applications.

The applicability of the heat transfer biofilm sensor to a planar C-PP substratum with an improved sensitivity, in the range of a few $\mu m^3/(\mu m^2 \times$a.u.), compared to SST pipes, enables the installation of the sensors in-situ into the electrodes of BES, thereby, directly at the point of interest in the biofilm reactor, under the same hydrodynamic conditions as electroactive biofilm. The high sensitivity of the biofilm sensor is comparable to that of laboratory optical measurements techniques such as OCT, and enables the precise monitoring of the electroactive biofilm in the assumed optimal range of biofilm thickness of up to 100 μm.

5 Detecting excess biofilm thickness in microbial electrolysis cells by real-time in-situ biofilm monitoring

Submitted: Netsch, A., Latussek, I. Horn, H.; Wagner, M. Detecting excess biofilm thickness in microbial electrolysis cells by real-time in-situ biofilm monitoring. Biotechnology and Bioengineering, 2025

Abstract:

Long-term stable operation of bioelectrochemical systems (BES) presupposes the avoidance of mass transfer limitations of the electroactive biofilm. Excessive pH-gradients from bulk to electrode interface or substrate limitations of the electroactive biofilm are known to diminish the electrical performance of BES. In this study the heat transfer biofilm sensor was utilized to monitor an electroactive biofilm on the anode of a microbial electrolysis cell (MEC) and identify the optimal thickness for a mixed-species wastewater biofilm. The maximum current density of approx. 3.5 A/m² was found for a mean biofilm thickness in the range of 100-150 µm, beyond which thicker biofilms caused mass transfer limitations. Along with local biofilm detachment a continuous decline in efficiency demonstrates the need for active biofilm control to adjust the biofilm thickness. Non-invasive monitoring by means of the biofilm sensor allowed for a continuous evaluation of the morphology of biofilm.

5.1 Introduction

Effective mass and charge transfer is crucial for the efficiency of bioelectrochemical systems (BES) (Yang et al. 2021). For the utilization of electroactive bacteria (EAB) as bio-catalysts for the conversion of waste streams to energy or value-added chemicals (e.g., hydrogen), their growth and metabolism must not be hampered by extrinsic limitations. In BES, usually EAB colonize the electrodes developing a conductive biofilm. Substrates providing a carbon source for the EAB (e.g., acetate, glucose) require to diffuse from the bulk phase to the substratum, while equally the products from the bacterial metabolism require to be removed avoiding the development of local accumulations within the biofilm.

Insufficient diffusive mass transfer is generally known as a limitation of productive biofilm systems, including BES (Philipp et al. 2024).

In the case of BES issues associated with the mass transfer focus on two major aspects. The impact of substrate supply to the electroactive biofilm on the current production has been extensively investigated by various groups (Cheng and Logan 2011; Ullah and Zeshan 2020). Generally, higher organic loads allow for greater current densities. Substrate-limiting conditions for different biofilm thicknesses have recently been demonstrated by Pereira et al. (2022c). For example, the maximum non-limited thickness of a mixed-culture biofilm with a bulk acetate concentration of 8 mM (COD = 512 mg/L) was found at $\overline{L}_F$= 55 µm. The second issue that needs to be considered is the accumulation of protons within the electroactive biofilm, leading to local acidic environments. Usually, with the conversion of organic substrates, protons are produced to maintain charge neutrality in the solution. *Geobacter sulfurreducens*, a model EAB, is completely inhibited at pH < 5, and their growth rate drastically decreases in more acidic environments (Patil et al. 2011). Similarly, the current production by *G. sulfurreducens* was reduced by 50 % when the bulk pH is reduced from 6.9 to 6.15, corroborating the inhibition of the metabolism by acidic pH environments (Renslow et al. 2013). In laboratory experiments, pH gradients are often avoided by the addition of buffer systems to the medium. Too weak buffer systems though result in buffer-limiting conditions, depending on the thickness of the biofilm (Pereira et al. 2022b.)

Charge transfer of electrons from the oxidation reaction of the EAB to the electrode is considered the other limiting factor for efficient BES. Electron transfer from EAB to the electrode are commonly described by two different mechanisms of extracellular electron transfer. Direct electron transfer (DET) via cytochromes or conductive transfer via nanowires (e.g., e-pili) and mediated electron transfer (MET) via electron shuttles/redox mediators (Schröder 2007). The distance of DET mechanisms is limited. DET via cytochromes, incorporated in the bacterial periplasm require direct physical contact with the electrode, limiting this mechanism to a monolayer of bacteria (Schröder 2007). Conductive pili, however, enable the conduction of electrons to further distant solids (Reguera et al. 2006). Even though considering the electroactive biofilm as a conductive matrix of bacterial nanowires, with increasing distance, a higher electrical resistance of the biofilm hampers electron transfer towards the electrode (Babauta et al. 2012; Jain et al. 2011). Mediated electron transfer utilizing molecular electron shuttles (e.g., quinones) underlay the same diffusive mass transport restrictions as substrate supply at larger distances of the microorganism to the electrode. Both electron transfer mechanism seem to be dependent on the local pH in the biofilm (Malvankar et al. 2011; Wu et al. 2016).

In summary, though thicker biofilms contain a higher biomass possibly contributing towards current production, inherently the biofilms will develop mass transfer gradients limiting the current production of the EAB closest to the electrode. Various models have been developed to describe the relationship between biofilm thickness and current production in MFCs, suggesting the need for a regulated biofilm thickness to avoid mass transfer limitation (Kato Marcus et al. 2007; Oliveira et al. 2013; Picioreanu et al. 2010). From experimental investigations different optimal thickness ranges for a *G. sulfurreducens* biofilm (between 30-100 μm) for maximum current production have been reported (Pinck et al. 2020; Read et al. 2010; Reguera et al. 2006; Sun et al. 2016). Nevertheless, Renslow et al. (2013) suggested an electron transfer of EAB to the anode over distances of several 100 µm, even passing inactive zones with dead biomass.

Most experimental studies or theoretical models presented thus far in literature discussing the impact of biofilm morphology on the current production of MFCs, have investigated single species biofilms. Targeting the application of BES for the energy recovery from waste stream, however, mixed-culture biofilms will form on the electrodes. Little is known about the relationship between biofilm morphology and current production for wastewater biofilms. Aim of this study was to investigate the correlation between the morphology of an electroactive biofilm cultivated from wastewater and the current density produced in a microbial electrolysis cell (MEC). The biofilm was cultivated in meso-fluidic flow cells and closely monitored by means of optical coherence tomography (OCT), a laboratory technique commonly used in the investigation of electroactive biofilms (Hackbarth et al. 2020; Molenaar et al. 2018; Pereira et al. 2022a). Additionally, the biofilm was monitored by an industrial heat transfer based biofilm sensor. Thereby, investigating the feasibility of its application as an on-line monitoring tool for electroactive biofilms on the electrodes of larger scaled BES, in which laboratory methods are not suitable, was investigated (Netsch et al. 2025, compare Chapter 4).

5.2 Materials and Methods

MEC flow cell setup

Meso-fluidic flow cells as previously described by Netsch et al. (2025, see Chapter 4) and Hackbarth et al. (2020) were operated as single chamber MEC. Graphite-Polypropylene (C-PP) anodes were integrated along the middle axis into the bottom of the flow cell made from polyoxymethylene (POM). The anodic area was A_{anode} = 1951 mm² (l × w × h = 101×20×4 mm³). In each flow cell two V4A stainless-steel electrodes ($A_{cathode}$ = 2 × 1437 mm²) were mounted on the sides above the anode with

a vertical distance between anode and cathode of 6 mm. The ratio of cathodic to anodic area was approx. 1.36 to avoid cathodic limiting conditions, possibly interfering with the current production. The flow cell was closed with a polycarbonate (PC) optical window to allow for biofilm imaging by means of optical coherence tomography (OCT) along the entire anodic electrode area. On the backside of the anode a heat transfer biofilm sensor DEPOSENS (Lagotec, Magdeburg, Germany) was integrated. The mounting of the sensor to the backside of the anode enables the biofilm monitoring by the sensor without interfering with the hydrodynamic conditions in the flow cell or introducing a different substratum material at the point of visualization and electron transfer.

Figure 5.1: Experimental setup showing three flow cells (A) with integrated biofilm sensor operated in parallel. The cultivation medium was stored in flasks (B) and pumped with magnetic gear pumps (not in image) through the flow cells from bottom to top. Medium for the continuous operation was added into the piping system via peristaltic pump from storage flasks (C).

Figure 5.1 shows the experimental set-up with triplicates of the meso-fluidic flow cells connected with flexible tubing (Tygon A-60-G, Carl Roth, Germany) to medium flasks and a magnetic gear pump (PAT Niemzik, Haan, Germany) for the re-circulation of the cultivation medium. A volumetric flow rate of 100 ml/min was set resulting in a mean flow velocity in the flow cell of 0.5 cm/s. The dimensions of the flow channel were ($l \times w \times h = 220 \times 40 \times 9$ mm^3). In the flasks the medium was continuously sparged with nitrogen gas to ensure anaerobic conditions. The medium was heated

to a temperature of 30 °C ± 2°C (measured at the by the medium temperature probe of the biofilm sensor), to maintain constant cultivation conditions.

Biofilm cultivation procedure and medium composition

The flow cell triplicates were inoculated with a pre-conditioned wastewater from a MFC reactor (construction based on (Haupt et al. 2022)) operated for over half a year with an acetate based cultivation medium. The inoculum was extracted from the bulk phase of the MFC reactor and anaerobized before introduction to the system. Each flow cell was inoculated with 1 L. After inoculation concentrated cultivation medium was injected to the system. The medium composition was modified from Hackbarth et al. (2023) containing: 84 mg/L KH_2PO_4, 44 mg/L K_2HPO_4, 40 mg/L NH_4Cl, 42 mg/L $MgCl_2$, 0.2 mL 0.4 mM $CaCl_2$ solution, 2 mL NB trace mineral solution (100x concentrated), 0.2 mL selenite–tungstate solution (13 mM NaOH, 17 μM Na_2SeO_3, and 12 μM Na_2WO_4), 2 ml Wolin's vitamin solution (German Type Culture Collection DSMZ 141). The cultivation medium was autoclaved and anaerobized by N_2-sparging before introduction to the system. As a carbon source sodium acetate (15 mmol/L unless noted otherwise; COD = 960 mg/L) was added. Biofilm cultivation was performed as batch mode for the first 7 days of the experiment to avoid flushing out planktonic bacteria and support initial attachment of the biofilm. After 7 days the medium was continuously replenished with cultivation medium at a volumetric flow rate of 0.4 ml/min with a peristaltic pump (Reglo digital, Ismatec). Excess medium from the system was removed via overflow. Since, the focus of this study was the cultivation of thick anodic biofilms causing mass transfer limitations in the close proximity of the anode at a constant medium composition. The reactor medium was continuously replenished aiming to set a constant acetate concentration and buffer capacity, thereby, removing the effect of varying medium composition observed in batch or fed-batch experiments.

Two experimental runs were performed with each triplicate flow cells, however in experiment B in one flow cell no electroactive biofilm was cultivated successfully. Table 5.1 shows the conditions for the experimental runs. Note that the system volume was reduced in Exp. B due to the change of 1 L flasks to 0.5 L flasks for the integration of dissolved oxygen probes.

Table 5.1: Overview of the experimental conditions of both experimental runs Note that in Exp. B in one flow cell no electroactive biofilm developed and was therefore excluded from the study.

	duration (d)	no. flow cells	V_{system} (L)	$c_{acetate}$ (start) (mmol/L)	COD (mg/L)	OD_{600}
Exp A	54	3/3	1.3	20	1200	0.1
Exp B	62	2/3	0.8	15	900	0.05

Sampling and measurements

Liquid samples (5 mL) were taken from the bulk medium and the inflow daily. Acetate concentrations were determined via ion chromatography (Metrohm 881 Compact Pro Ion Exchange Chromatograph with a Metrosep Organic Acids 250/7.8 column, Metrohm, Switzerland). Electrical conductivity and pH of the liquid samples were measured daily with lab-grade probes (WTW - SenTix 41, TetraCon 325, Xylem, Weilheim, Germany). Dissolved oxygen concentration was monitored with fiber-optical oxygen probes (ROB10, Pyroscience, Aachen, Germany). The optical cell density (OD_{600}) was measured with a UV/VIS spectrometer (Lambda XLS+, PerkinElmer, Rodgau, Germany).

Biofilm monitoring and OCT anaylsis:

Biofilm development on the anode of the MEC was monitored by the heat transfer biofilm sensor. The biofilm sensor measures the increasing thermal resistance on the substratum due to accumulating biofilm and reports a dimensionless signal (in arbitrary units a.u.) as output. For its validation the sensor signal, as an indicator for the biofilm thickness, was correlated with the biofilm thickness calculated from OCT images at the position of the sensor (OCT Position A - see Figure 5.2). A more detailed description of the working principle of the biofilm sensor was described extensively in a previous publication by this group (Netsch et al. 2021, 2025, see Chapter 3.2). The temperature difference between heater and medium probe was set at $\Delta T = 5$ K to reduce impact of locally different cultivation temperature. The sensor's reference measurement in clean state was set to zero at a volumetric flow rate of 100 ml/min.

Additionally, for validation of the sensor measurement and in-depth analysis of the morphology of the electroactive biofilm daily OCT-scans of 3 selection positions A-C ($w \times l = 4 \times 6$ mm²) along the middle axis of the C-PP anode were performed monitoring a total surface of 72 mm² (approx. 4 % of total anodic area). OCT images were acquired with a GANYMEDE spectral-domain base-unit (GAN610, Thorlabs GmbH, Lübeck, Germany) with a OCT9G scanner and OCT-LK4-BB lens (all components from Thorlabs GmbH, Lübeck, Germany). The lateral pixel resolution was set to 8 µm/px and vertical pixel resolution to 2.06 µm/px. As the entire biofilm growing on the electrode contributes towards the anodic current generation, a "full scan" of 10 positions over the entire width of the electrode ($w \times l = 10 \times 16$ mm²) was taken weekly to visualize the biofilm on a total of 82 % of the anodic area. Images of the "full scan" reveal the representativeness of the daily OCT imaging scheme and uncover uneven biofilm distribution. To reduce the data quantity the "full scan" images were taken with a reduced lateral pixel resolution of 24 µm/px. Imaging positions on the electrode are displayed on Figure 5.2.

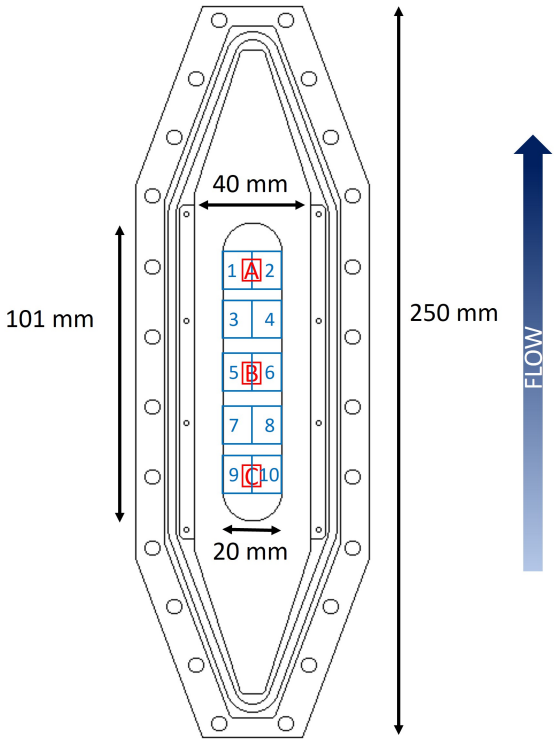

Figure 5.2: Sketch of the meso-fluidic flow cell with the imaging positions for the OCT scans. Red rectangles (4 × 6 mm²) denote the Positions A-C (from bottom to top) that were monitored daily. Blue rectangles (10 × 16 mm²) show the imaging areas (1-10) that were monitored weekly.

Biofilm parameters obtained from the OCT images were calculated according to Wagner and Horn (2017) using in-house ImageJ macros. The distance of the bulk-biofilm interface to the electrode is described by the mean biofilm thickness $\overline{L}_F$, with $L_{F,i}$ being the local biofilm height (Eq. 5.1). The substratum coverage (SC) specifies the percentage of electrode, on which biofilm has grown (Eq. 5.2). OCT images are displayed in the later sections as height maps showing the distance of the bulk-biofilm interface from the substratum (electrode).

$$\overline{L}_F = \frac{1}{N}\sum_{i=1}^{N} L_{F,i} \qquad (\mu m) \tag{5.1}$$

$$SC = \frac{A_{OCT} - A_{uncovered}}{A_{OCT}} \qquad (\%) \tag{5.2}$$

Electrochemical measurements

Anodes (working electrode) were contacted directly by a socket incorporated into the anode material, while the cathodes (counter electrode) were contacted with Grade 2 titanium screws. An Ag/AgCl-

reference electrode (SE23-I, Xylem Analytics, Waldheim, Germany) was installed at the outlet of the flow cell in a custom made stainless-steel electrode holder. All electrodes were connected with a potentiostat (Interface 5000P, Gamry Instruments, Warmister, USA) for anodic potential control and electrochemical measurements. Calculated current densities from the chronoamperometry are in reference to the anodic area $A_{anode} = 1951$ mm². The Coulombic Efficiency (CE) was calculated according to Eq. 5.3 giving the ratio of electroactively consumed acetate to the total acetate consumption in the system. The CE was determined for each time interval between two liquid sampling points (t_2 and t_1), whereas Δc(acetate) described the total acetate consumption in the time interval. The total amount of electroactively consumed acetate was determined by the number of released electrons to the anode. This was calculated by the integral of the resulting current I in the time interval, the number of electrons released per mol of acetate ($z_e = 8$), the reactor volume (V) and Faraday's constant (F = 96485 C/mol).

$$CE = \frac{\int_{t1}^{t2} I(t)dt}{z_e \times V \times \Delta c_{Ac} \times F} \qquad (\%) \tag{5.3}$$

5.3 Results

Current development

Figure 5.3 shows the development of key parameters (current density i_{anode}, mean biofilm thickness $\overline{L}_f$, bulk concentration of acetate $c_{acetate}$ and sensor signal D) in the MECs over the course of the cultivation period. Anodic current production commenced within the first two days after inoculation and displayed a rapid development along with increasing mean biofilm thickness. Interestingly, between Day 3 and 4 of the experiment the current production in four of the MECs seems to stagnate (A2) or even decrease (A1, B1 and B2) before continuing the rapid trend of current increase. Metabolic changes of the EAB from catabolism to anabolism on the anode may explain the inflection in the current development. This effect was possibly not visible for MEC A3 due to an overlapping of the exponential growth phase on different sections of the anode due to the delayed bacterial growth.

After 7 days of cultivation the MEC operation was switched from batch mode to continuous addition of fresh medium and removal of bulk medium. Before changing the operation conditions all MECs reached a maximum current density of 2.4 A/m² (A1), 3.5 A/m² (A2), 1.8 A/m² (A3), 3.7 A/m² (B1) and 6 A/m² (B2). While the steep increase of the current density was aligned with the rapid anodic

biofilm development the height of the current density peak must be put in relation to the pH of the medium. During batch operation the pH increased from 7.2 at inoculation to a pH between 9.0 and 9.2 for all flow cells. The drop of the current density with the continuous addition of medium (pH = 7.2), therefore, is likely the consequence of the resulting pH decrease to more neutral values around 7.5.

During continuous operation the current density remained stable for approx. 10 days in the MECs A1, A2 and B2. While MECs A3 and B1 still showed an increasing current density presumably along with the delayed biofilm growth on some parts of the electrode (compare Figure 5.4). After approx. 25 days (A1 and A2) or 30-35 days (A3, B1 and B2), respectively, all MECs reached a secondary maximum current density at approx. 3.5 A/m^2. Beyond the maximum the MECs deteriorated in their stability and total current output. Despite, the continuous replenishment of the cultivation medium, the acetate concentration in all MECs steadily decreased along with the current density. Simultaneously, these MECs showed an increased consumption of acetate of non-EAB in the system, which in summary leads to a reduced CE, from approx. 40-60% in the early stages of the experiment to 5-15% during the latter stages (more details in Figure 5.7). The decreasing current production after the secondary maximum may have been caused by a reduced concentration of acetate in the bulk, that could have led to a substrate limitation of the EAB in the proximity of the anode.

To determine, if the anodic biofilm was substrate-limited at Day 40 (Exp A) and Day 57 (Exp B), continuous medium addition was interrupted, and the acetate concentration was increased to 20 mmol/L (COD = 1200 mg/L) or 15 mmol/L (COD = 960 mg/L), respectively. In Exp B in both MECs the current rapidly increased to a range similar the secondary maximum, indicating the limiting factor for current production was the availability of the carbon source for the electroactive biofilm. In contrary, the MECs of Exp A showed an additional drop in the current density suggesting other limiting factors beyond the substrate availability reduced the current production.

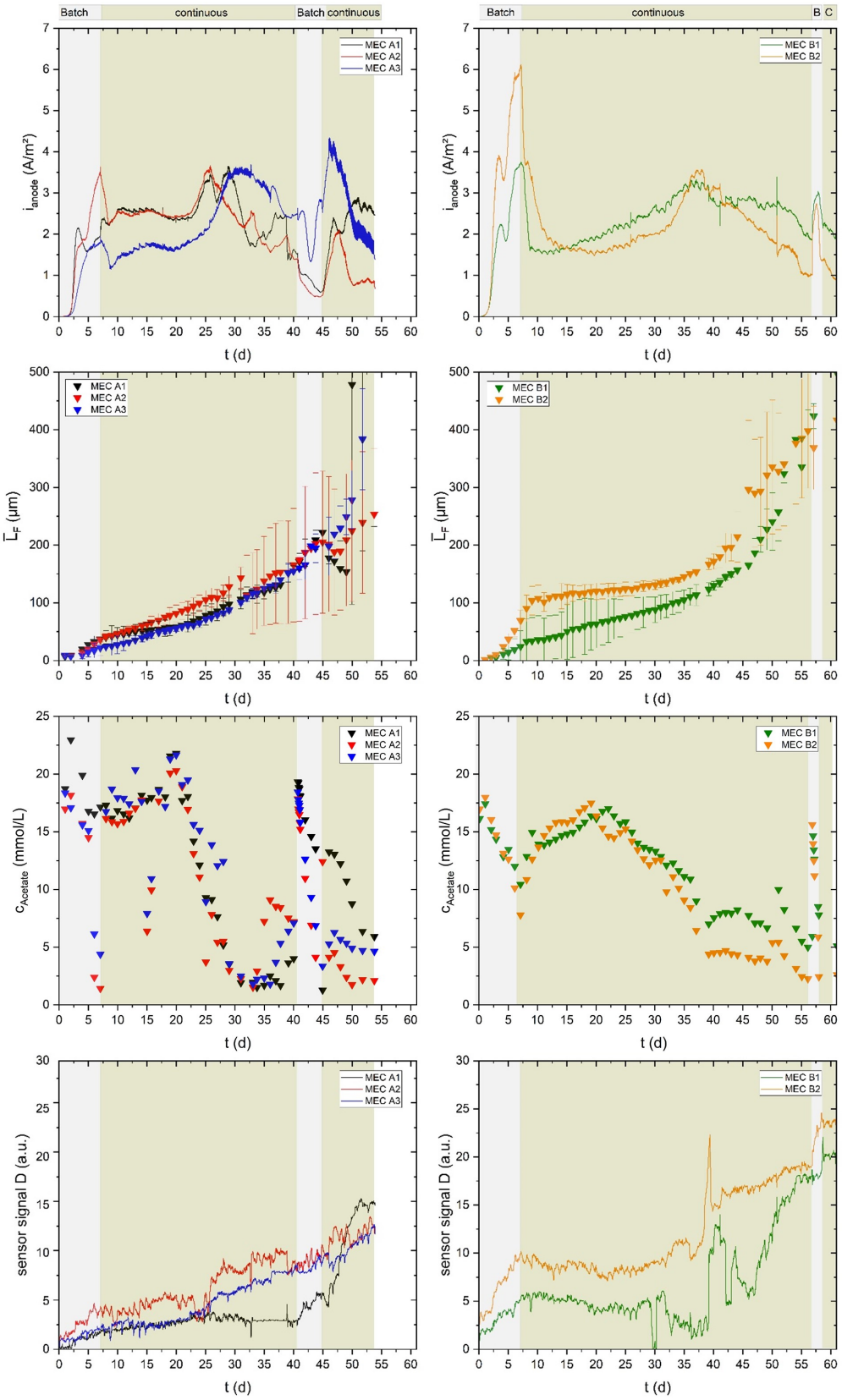

Figure 5.3: From top to bottom the development of the current density, mean biofilm thickness, concentration of acetate in the bulk medium and sensor signal shown for the MECs of experiment A (left) and B (right). Compare with Table 5.1.

Biofilm development and detachment

The electrodes of MECs A1, A2 and B2 showed an almost complete coverage of the substratum within the first few days after inoculation. As an example, Figure 5.4 shows the height map of a "full scan" of the electrode of MEC B2. Additionally, the height maps of the other MECs are provided in the Appendix (see Figures A2, A3,A4, A5). The biofilm in all MECs grew mostly steady with a growth rate between 3-7 µm/d until approx. Day 35. The distribution of the biofilm was mostly homogeneous for the electrode areas that were well covered during the inoculation, visible by the comparatively low standard deviation of the mean biofilm thickness for MECs A1, A2 and B2 (see Figure 5.3). In contrary the electrode of MECs A3 and B1 was unevenly covered, whereas larger areas of the electrode (imaging position C - closest to the inflow) initially remained uncovered. Possibly, the free jet at the inlet has caused increased shear forces hampering bacterial attachment. The uncovered areas however were covered within the next few days, so that biofilm growth simply was delayed. This aligned with the reduced current production in both MECs.

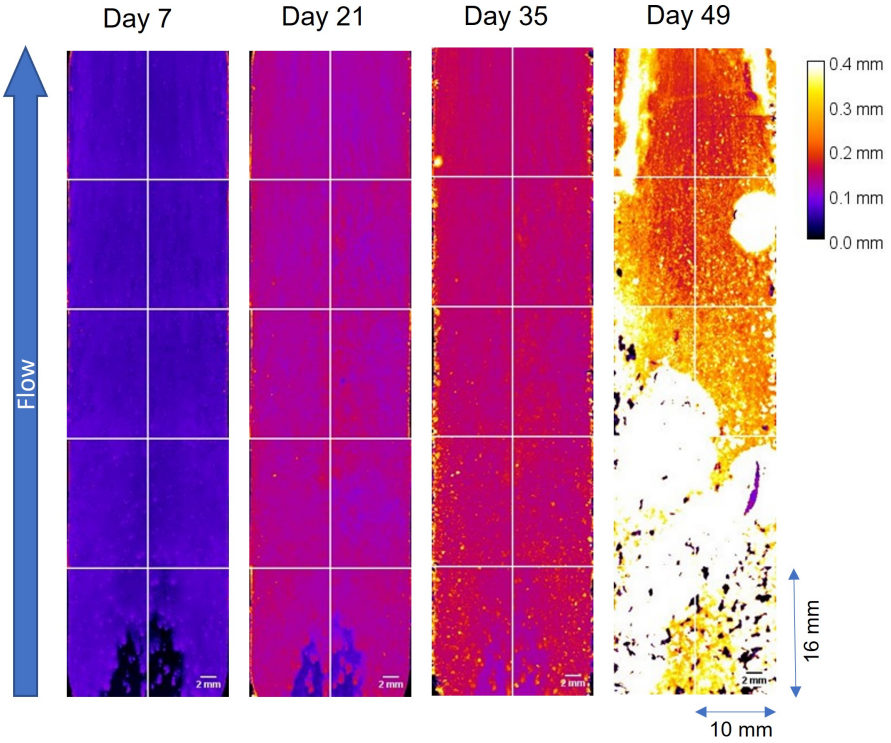

Figure 5.4: Height maps derived from OCT images showing the distance of the bulk-biofilm interface from the electrode substratum of MEC B2 (see Table 5.1). For Days 7, 21, 35 and 49 a full scan displaying approx. 82% of the electrode were taken. The height map displays the thickness of the biofilm according to the heat map for the range of 0-400 µm. The direction of flow was from bottom to top.

After Day 30-35 of both experiments, a rapid increase in the biofilm accumulation rate was detected by OCT imaging along with an increasing sensor signal of the biofilm sensor. The surge of the biofilm accumulation rate can be explained with two different causes. Firstly, it seems a secondary biofilm layer rapidly developed on top of the initial biofilm layer (compare Figure 5.5). While the bottom layer displayed a very homogeneous and compact structure (reddish color) the secondary biofilm grew spottier in higher filamentous patches (blackish/yellowish). The different morphologies of the two biofilm layers indicates the dominance of different bacteria in the two respective biofilm layers. We infer that the slow growing bottom biofilm layer was dominated by EAB contributing towards the current production, while the secondary biofilm layer likely originated from another fast-growing microbial species.

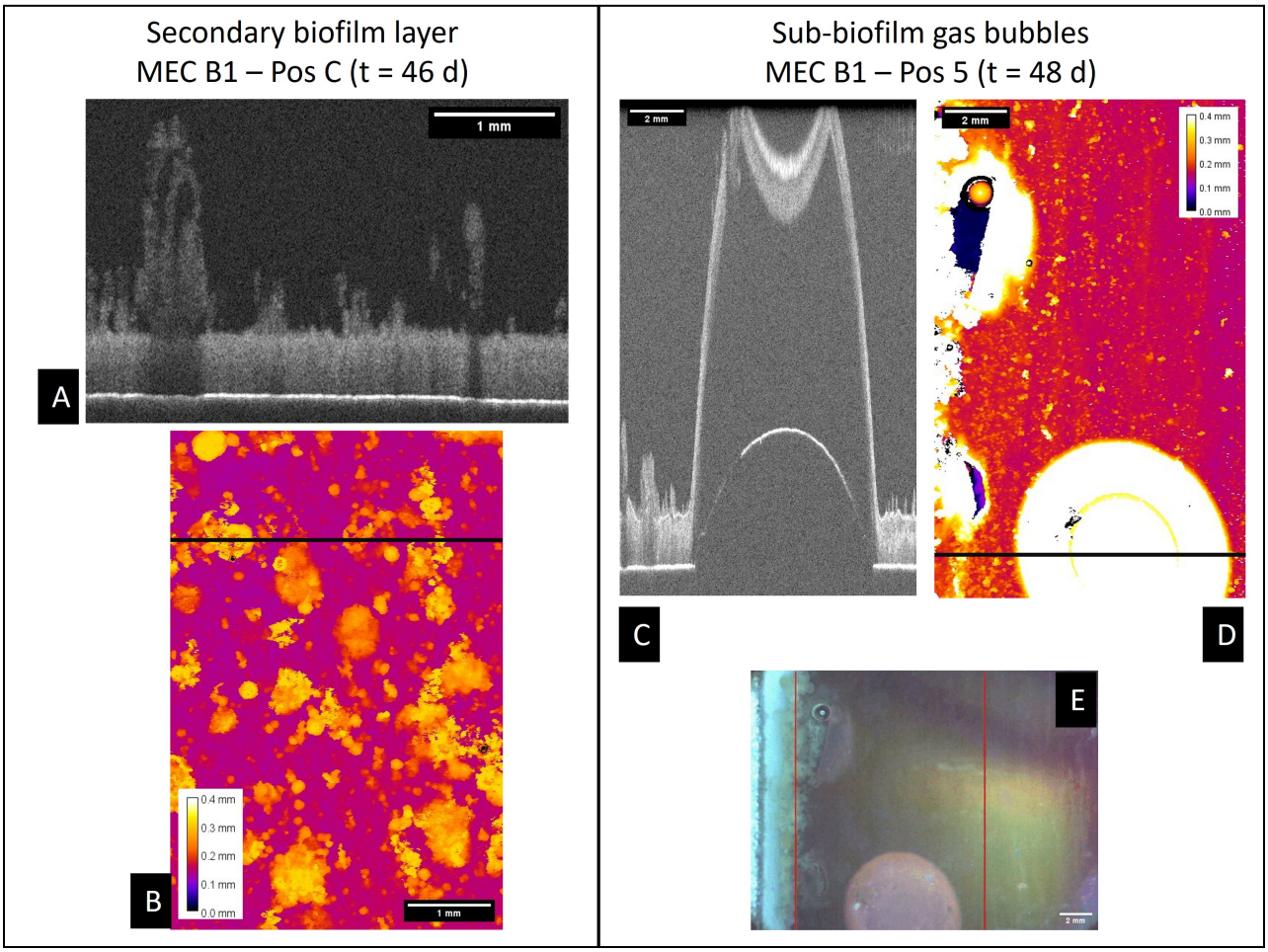

Figure 5.5: (left) Shows a developed gas bubble entrapped below the biofilm in MEC B1 on Day 48 (A - cross-section, B - height map, C - top view image) (right) Shows spotty growth of the secondary biofilm layer (fluffy high structures) on top of the homogeneous primary biofilm layer in a cross-section (D) and the corresponding height map (E). The high yellowish spots in the height map display areas covered by the secondary biofilm layer. The black lines in the height maps mark the position of the respective cross-sections.

The second cause for the biofilm deterioration was a partial detachment of the biofilm mainly caused by gas bubbles (most likely CO_2 or CH_4) forming at the anodic interface. An example of this phenomenon is displayed in Figure 5.5 (A-C), where over several days a locally isolated gas bubble developed below the biofilm surface with an approximate area of 12.5 mm² (≈0.5 % of the anode area). Consequently, the electroactive biofilm layer was locally lifted from the anode and partially ripping patches of biofilm off. The structure of the biofilm seemed to prevent the diffusion of gaseous products from the conversion of organic substrates at the anode. Biofilm detachment events were visible at several occasions, although the biofilm was rarely completely removed. Below the lifted biofilm the electrode was freed from biofilm, suggesting the gas bubbles formed directly at the electrode interface. However, the detachment events could not be directly correlated with a sudden drop of the current density, but are in line with the overall decreasing current density beyond approx. Day 30-35, due to the limited area affected by the individual detachment events and the relative long time interval (several days) for the development of the gas bubbles. For example, the detachment event in MEC B1 on Day 48 (compare Figure 5.3) did not show a change in the decreasing trend of the current density. Though not clearly distinguishable, it is suggested that both causes may have contributed towards the deteriorating current production as a result of the biofilm structure.

Correlation biofilm thickness and current density

The dependency of the current density from the accumulated biofilm on the electrode is displayed in Figure 5.6, in the left subplot, separately for the first 7 days during batch mode and the correlated data points during continuous operation (right).

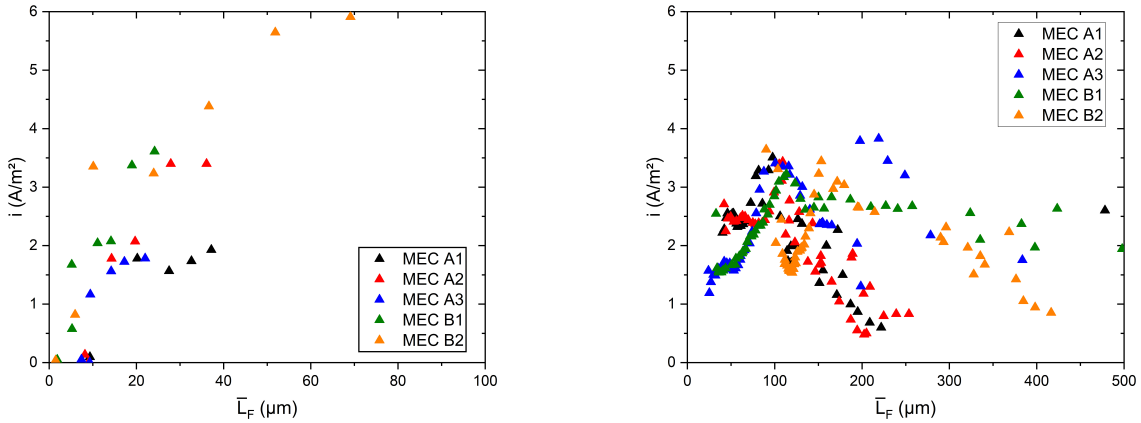

Figure 5.6: Correlation of the current density with the mean biofilm thickness (Pos. A-C - compare - Figure 5.2) of the initial growth during the batch phase (Day 0-7 - left) and during continuous operation > Day 7 (right).

During the initial attachment and growth phase in batch operation of the first 7 days, a linear correlation of the current density with the mean biofilm thickness was visible. Similarly, after acclimatization of the biofilm to the continuous operation the increase in current density per accumulated biofilm showed a linear trend until the maximum current density. However, in comparison during batch operation the slope of this trend ($97.08 \pm 32.84\,A/mm^3$) exceeds the slope of the current growth up to its maximum during continuous operation ($37.18 \pm 8.1\,A/mm^3$) by a factor of 2.6.

All MECs reached a maximum in their produced current density of between 3.2-3.5 A/m^2 at a mean biofilm thickness of 100-115 µm. Although, MEC B2 having an increased biofilm growth reached its maximum at a mean biofilm thickness of 150 µm. Further biofilm growth, however, did not contribute towards an elevated current production of the MECs (see Figure 5.6). A steady decrease of the current density can be seen for all MECs at higher biofilms thicknesses. This may be a consequence of the increasing diffusion depth for both educts (acetate) and products (protons and CO_2) of the metabolism of the EAB. Interestingly, the decline of the current density differed in the magnitude among the MECs. While MECs A1 and A2 produced only a current density of less than 1 A/m^2 at a mean biofilm thickness in the range of 200 µm, the MECs A3, B1 and B2 were able to produce approx. 2 A/m^2 with a mean anodic biofilm thickness between 300 to 400 µm.

The decline in the efficiency of the electroactive biofilm could also be seen in the development of the CE over time. Figure 5.7 displays the CE for all MECs of time.

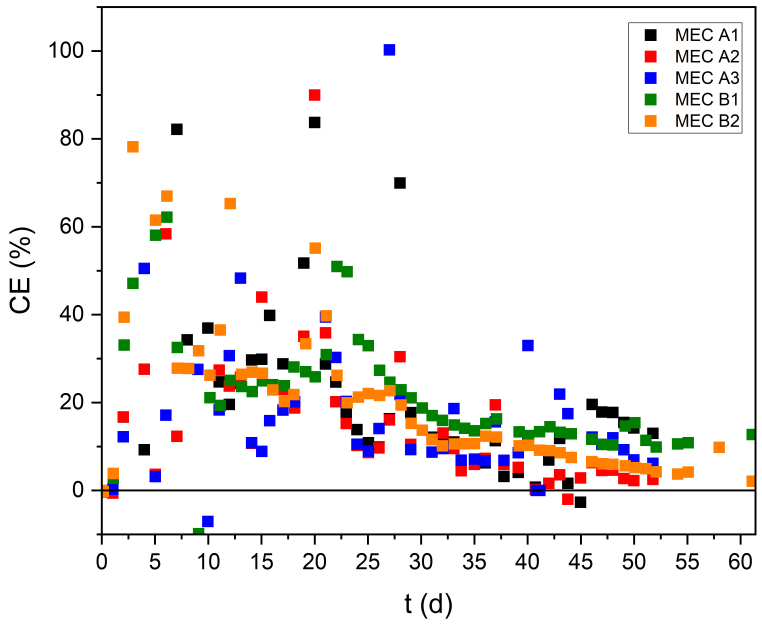

Figure 5.7: Development of the coulombic efficiency (CE) of the MECs over the course of the biofilm cultivation. The CE was calculated based on Eq. 5.3 for the time interval between to sampling points of typically 24 h.

The highest efficiency in terms of fraction of acetate consumption by the EAB was visible towards the end of the initial growth phase in batch mode (Day 7). Here, due to the polarization of the anode at -199 mV vs. Ag/AgCl a favorable niche supports the high selectivity for EAB. Similar to the current development a lower secondary maximum of the CE was visible, that coincided with the peak acetate concentration during the continuous mode. This secondary maximum was in the range of 35-50%. Interestingly, the maximum point, around Day 20 for all MECs, preceded that of the current density by a few days. Possibly, the secondary growth phase during the continuous mode may have been triggered by an increased acetate concentration, leading to the higher CE. For the remainder of the biofilm cultivation however a continuous decline of the CE was visible. This aligns with the suggested increased acetate consumption by non-EAB. Between Days 45-50 the CE for all MECs had decreased to 5-15%.

Evaluation of anodic biofilm by means of the biofilm sensor

From the correlation of the current density with the mean biofilm thickness on the anode an optimal biofilm thickness for maximum current production can be deduced for the continuous operation. This suggests for long-term stable operation controlling the biofilm thickness within the range of 100-150 µm.

For the technical-scale application of BES, the monitoring by means of a non-invasive and user-friendly biofilm sensor would support the evaluation of the state of the anodic biofilm. Biofilm monitoring of the anodes in the meso-fluidic flow cells was performed by the installed heat transfer biofilm sensor on the backside of the anode and confirmed by means of OCT scans. The correlation of the biofilm sensor signal with the mean biofilm thickness at the OCT Position A (point of sensor measurement) is displayed in Figure 5.8.

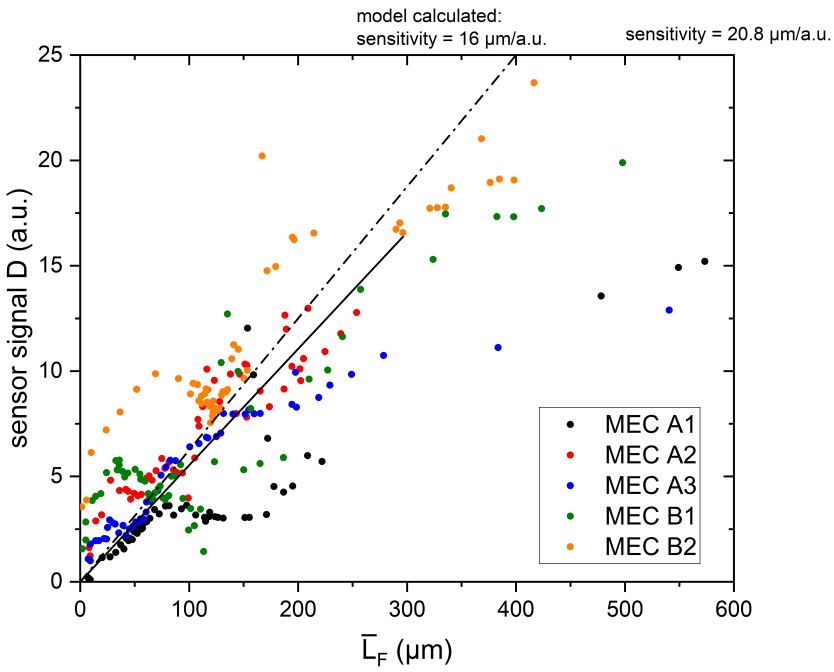

Figure 5.8: Correlation of the dimensionless sensor signal with the mean biofilm thickness calculated from the OCT scans of Pos. A (compare Figure 5.2).

Despite subject to some fluctuations the sensor signal and mean biofilm thickness displayed a linear correlation ($R^2 = 0.87$) with a resulting sensitivity of 20.8 µm/a.u.. Deviations from the linear correlation may have been caused by unstable flow conditions due to excessive biofilm growth in the periphery of the flow cell at later stages of biofilm cultivation. Rapid increases/decreases in the sensor signal are caused by a variance of the volumetric flow rate, then during zeroing at the begin of the experiment (compare Figure 5.3). Additionally, if the minimum required flow velocity for a sensor measurement by means of the biofilm sensor was not exceeded, the sensor signal may have stagnated, e.g., MEC A1. Applying the model for the calculation of the sensor sensitivity presented in Netsch et al. (2025, see Chapter 4.3) with the volumetric flow rate of 100 ml/min an improved sensitivity of 16 µm/a.u. is suggested compared to the determined sensitivity in this study. The deviation may be

explained with the non-linearity of the sensor sensitivity for thicker biofilms (Netsch et al. 2025).

As mentioned above, the sensor signal was correlated with the OCT-scans of Pos. A in the flow cells imaging the point of sensor measurement. However, since the biofilm on the entire surface of the electrode contributes towards the current production, the representativeness of the biofilm measurement needs to be analyzed. Comparing the mean biofilm thickness at Pos. A with the mean biofilm thickness derived from full scans including approx. 80 % of the electrode area revealed a slight underestimation. With the exception of MEC B1, the biofilm at Pos. A generally had the tendency to be thinner by a margin of up to approx. 25 % compared to the full scan within the first 41 days of the experiment. The non-equal biofilm growth was likely a consequence of local variations in the hydrodynamic conditions, as there were also found by Hackbarth et al. (2023) using the same flow cell design. Later comparisons were subject to larger fluctuations due to local detachment events or spotty overgrowth, that increasingly compromised the representativeness of the OCT images. A more detailed analysis is shown in the Appendix (Figure A6). For upscaled BES with larger electrode areas, the uneven biofilm distribution displayed here, would suggest the use of multiple sensors to avoid misinterpretation due to non-homogeneous biofilm growth or locally limited detachment events, in consideration of the hydrodynamic conditions of the reactor.

5.4 Discussion

As previously described, electroactive biofilms are influenced by the trade-off between high bacterial accumulation in the biofilm and the resulting mass transfer limitations from the biofilm morphology. Diffusion coefficients of dissolved species in biofilms are reduced by several biofilm characteristics, including high cell density (Fan et al. 1990), low porosity (Yang et al. 2021), high biofilm age and large distance from the bulk phase (Renslow et al. 2010). Furthermore, Renslow et al., (2010) found a large variability of the local diffusion coefficients in the interior of biofilms due to the local variability of the biofilm structure. The development of sub-biofilm gas bubbles (compare Figure 5.5) hints towards local insufficient diffusive mass transfer of reaction products. Comparing the diffusion coefficients of the possible gases CO_2 and CH_4 with that of the substrate (acetate) it becomes obvious, that diffusion restrictions affecting the transport of product gases out of the biofilm will similarly impede the diffusive transport of substrate into the biofilm, as the diffusion coefficient of acetate is slightly lower than those of CO_2 and CH_4 (compare Table 2).

Table 5.2: Comparison of the diffusion coefficients in water for the relevant chemical species in the electroactive biofilm. The diffusion coefficients were taken from (Cussler 2009)

Chemical species	Diffusion coefficient in water ($\times 10^{-6}$ cm^2/s)
H^+	93.1
CO_2	19.2
CH_4	14.9
Acetate	12.1

Reduced diffusion coefficients along with large biofilm thickness lead to mass transfer limitations in the electroactive biofilm resulting in substrate limitations (Pereira et al. 2022c), as this was the case in the MECs of Exp B, visible during the spiking with substrate in the batch experiment. The substrate limitation in this study may have been enhanced by the development of the fast-growing non-electroactive secondary biofilm layer (Sleutels et al. 2016). The increased diffusion length for the substrate along with the increased substrate consumption of the secondary layer, have reduced the availability of substrate for electroactive consumption in the proximity of the anode, reducing not only the CE, but also the total current production.

Also more acidic pH environments in the anodic proximity (Li et al. 2017; Renslow et al. 2013) as a consequence of increased diffusion length can lead to a reduced electroactive metabolism. Franks et al. (2009) showed the magnitude of the resulting pH gradient in a *G. sulfurreducens* biofilm, with a decrease of 1 pH-unit in a approx. 70 µm thick biofilm. Although the slope of the pH-gradient depends on the respective biofilm characteristics, the 200-400 µm thick anodic biofilms in this study likely have developed an even larger pH decrease from bulk towards anodic interface. The effect of the pH on EAB has been demonstrated by Patil et al., (2011), showing the highest current production at a pH around 9, while in acidic pH environments pH < 5 EAB are partially or completely inhibited, which is further reinforced by weak-buffer systems (Pereira et al. 2022b). Metabolically inactive regions result in less effective biofilms. Both substrate limitation and pH inhibition occur simultaneously in a BES, as they similarly increase with growing biofilm thicknesses and might not be distinguishable in the decline of the produced current.

Yang et al., (2021) suggests the regulation of the biofilm thickness and porosity to enhance mass transfer in an electroactive biofilm. This poses the question for an optimal electroactive biofilm thickness in BES. While,this may simplify the effect of the biofilm morphology in the mass transfer, the monitoring of the continuous growth by means of the biofilm sensor might be an easy and viable indicator for the prediction of impaired current production due to the anodic biofilm morphology. The optimal

biofilm thickness for maximum current production has mostly been investigated for mono-cultural biofilms (e.g., *G. sulfurreducens*) showing viable biofilms up to a thickness of 80 µm (Pinck et al. 2020). However, considering the application of microbial fuel cell in wastewater treatment, a more complex mix of microbial species is expected. Similar to the overgrowth of the electroactive biofilm layer in this study (compare Figure 5.5 D & E) undesired microorganism in the electroactive biofilm should be removed or their growth suppressed. In this study a complex mixed culture preconditioned from a municipal wastewater treatment plant was used, developing the maximum current production during continuous operation a higher range of thickness between 100-150 µm. If the described optimal range of biofilm thickness found in this study can be applied widely for different mixed culture electroactive biofilms, requires more extensive analysis. Though, a global study by Santoro et al. (2021) found comparable power outputs from different wastewater inocula in identical systems, while the enriched bacteria in the biofilm differed from each other.

Although not specifically identified, large scale pilot-plant microbial fuel cells in wastewater treatment applications by several groups (e.g., Blatter et al. 2021 or Babanova et al. 2020) have shown a continuous decline of the current production, possibly attributed to increasing mass transfer limitations. The decline in current production and CE over time along with increasing anodic biofilm thickness in this study, clearly shows the necessity of biofilm control mechanisms. Unlike biofilm control in technical systems such as, e.g., membrane applications a complete biofilm removal is not targeted. Moreover, given the maximum current production found in the range of 100-150 µm the aim should be to continuously set the biofilm to this thickness. It was shown by Islam et al. (2017) that periodic treatment ultrasound of an MFC with carbon brush electrodes revitalized the electroactive biofilm to the same maximum current density as before its decline over a period of 40 days. Similarly, flow induced increase of shear forces was investigated by the same group of researchers showing a recovery of the current production (Islam et al. 2019). In both cases the physical control mechanisms removed large fractions of the biofilm followed by a quick reattachment of living cell. Thereby, showing the need for a removal of dead cells, as a high ratio of living cells in a thinner biofilm is most desirable (Islam et al. 2019). Heat transfer biofilms sensors can allow for a condition-based use of control mechanisms, by detecting excess biofilm thickness or surges in the biofilm growth rate which might indicate an overgrowth of the electroactive biofilm layer. Applicable biofilm control mechanisms may be limited due to constructive restrictions in BES reactor design. Control mechanisms used in other fields of productive biofilm applications may present more viable options. Hwang et al. (2010) used nitrogen sparging to adjust the biofilm thickness in a membrane biofilm reactor with a nitrifying biofilm. Wei

et al. (2024) used air-scouring in a membrane aerated biofilm reactor for biofilm control, while Zhang et al. (2017) used mechanical abrasion to remove salt precipitation and biofilm from an air cathode in MFCs. Although, targeting different deposits on the substratum the control mechanisms were equally utilized to remove mass transfer limitations in productive biofilm applications.

5.5 Conclusions

Within this study the development of the anodic biofilm in a MEC was monitored over a period of up to 62 days to quantify the relationship between accumulation of biofilm and current production. The aim was to demonstrate the applicability of a non-invasive on-line heat transfer biofilm sensor for the monitoring of the electroactive biofilm and identify its optimal thickness for a maximum current production, while avoiding mass transfer limitations.

- An optimal thickness range for an electroactive biofilm cultivated from wastewater was determined between 100-150 µm producing up to 3.5 A/m^2.
- A combination of mass transfer limitation due to the excess biofilm thickness along with increased substrate consumption by non-electroactive bacteria have led to decreasing substrate concentration in the proximity of the anode. The lower availability of substrate for EAB resulted in a declining current production.
- The deteriorating biofilm performance was caused by a combination of overgrowth of the primary electroactive biofilm layer with a fast-growing secondary biofilm, along with local detachment of the primary biofilm due to gas development beneath the biofilm at the anodic interface.
- Heat transfer biofilm sensors can viably support the monitoring of electroactive biofilm in the electrodes of BES. However, for the evaluation of the performance of the BES, the sensor information must be coupled with knowledge of the local hydrodynamic condition as well as the medium composition (pH, substrate concentration)

This study urges for the consideration of controlling electroactive biofilms. Effective mechanisms to adjust the thickness of the electroactive biofilm should be investigated, as they are required for long-term stable operation of BES in technical-scale systems.

6 Summary

The aim of this dissertation was the investigation and demonstration of the feasibility of the application of heat transfer biofilm sensors for the on-line monitoring of electroactive biofilms. Thereby, supporting the identification of mass transport limitations evoked by the structure of electroactive biofilms in upscaled reactor systems. The commercially available DEPOSENS biofilm sensor, whose measuring principle is based on the increased thermal resistance through the formation of deposits (e.g., biofilm), was integrated into different flow cells with a commonly used carbonaceous electrode material for BES. The experiments were conducted with anaerobic wastewater biofilms and electroactive biofilms to convert the dimensionless sensor signal into a structural biofilm parameter (e.g., mean biovolume or biofilm thickness). For the application of the sensor, its sensitivity, given as mean biovolume or biofilm thickness per arbitrary unit (a.u.), was determined based on the correlation of the sensor signal with the biovolume or biofilm thickness determined gravimetrically or by means of OCT. More desirable sensor sensitivities are indicated by lower values, as they allow for a finer distinguishment between different thicknesses of the accumulated biofilm.

For the assessment of the applicability of the DEPOSENS sensor as a biofilm monitoring tool on the electrodes in BES, initially, the material compatibility of a carbonaceous electrode material (C-PP) was investigated and compared to the standard application of the sensor on stainless-steel pipes (SST). Given the different material properties of the C-PP and SST, foremost the higher thermal conductivity of $\lambda_{C-PP} \approx 21\mathrm{W/(m \times K)}$ vs. $\lambda_{SST} = 13.31\mathrm{W/(m \times K)}$, an impact on the sensor measurement was expected. In the comparison of the sensors applied to C-PP pipes with those applied to SST pipes, the C-PP applied sensors displayed a worse sensitivity of approx. 52 $\mu\mathrm{m}^3/(\mu\mathrm{m}^2\times\mathrm{a.u.})$ compared to approx. 11 $\mu\mathrm{m}^3/(\mu\mathrm{m}^2\times\mathrm{a.u.})$ of the SST applied sensors. Increased thermal losses due to the higher thermal conductivity of the C-PP than SST, may have lead to a diminished sensitivity of the sensor. The application of a low ΔT of 5 K and 2 K, compared to typically 10 K, did not improve the sensor sensitivity, but a minimal ΔT of 5 K is necessary for the sensor measurement. Despite the reduced sensor sensitivity, when applied to C-PP the feasibility of the transfer of the sensor to electrode materials could be concluded.

Secondly, the hydrodynamic and geometric impacts on the sensor measurement were characterized, as both features can have a significant effect on the heat transfer in a system. Applying the DEPOSENS sensor to a planar C-PP substratum in meso-fluidic flow cells, allowed for a high temporal resolution of

the biofilm thickness to sensor signal correlation due to OCT imaging, along with the characterization of additional morphological biofilm parameters (e.g., substratum coverage, roughness and porosity). These parameters may impact the effective thermal conductivity of the biofilm, however, the predominant effect on the heat transfer seems to be attributed to the biofilm thickness or biovolume. The planar substratum in the flow cells increased the impact of the thermal resistance of the biofilm on the total thermal resistance. Consequently, an improved sensitivity on the range of 1 $\mu m^3/(\mu m^2 \times$a.u.) could be determined, outperforming the standard SST sensor at similar flow conditions. Additionally, the hydrodynamic impact on the sensor sensitivity could be demonstrated, as higher flow velocities further improved the sensor sensitivity. The thinner thermal boundary layer at higher Reynolds numbers, decreased the fraction of the convective thermal resistance and thereby the fraction of the thermal resistance attributed to the biofilm increases. The sensitivity of the sensor related to the gradient of the fraction of the biofilms thermal resistance compared to the total thermal resistance, with increasing biofilm thickness. A theoretical model incorporating the substratum material, geometry and the hydrodynamic conditions in the flow cell with biofilm sensor was developed and validated with the experimental measurements at four different flow velocities (9 - 27 cm/s), covering a typical range for biofilm reactors. The model will allow for the integration of the biofilm sensor into various electrode configurations and evaluate the sensor signal based on local hydrodynamic conditions. Among the commercially available and technically proven biofilm sensors, for the monitoring of biofilms in the mesoscale, the DEPOSENS sensor outperforms other sensors with a large range of measurable biofilm thickness along with the high sensitivity. The sensitivity is even in a comparable range to the optical resolution of OCT, a standard laboratory tool for biofilm investigation. Though biofilm sensors based on an electrochemical measurement principle can provide more insight in the initial biofilm formation and substratum coverage.

The necessity of biofilm monitoring for electroactive biofilms was demonstrated in the operation of the meso-fluidic flow cells as a MEC. The correlation of the mean biofilm thickness with the anodic current density showed at maximum current density of approx. 3.5 A/m² for a mean thickness in the range between 100 -150 μm for an anodic biofilm cultivated from wastewater. Beyond the maximum thickness the MEC performance (current density) deteriorated in a combination of effects associated with excess biofilm thickness. The increased substrate concentration gradients and pH gradients formed a low substrate and more acidic environment at the anodic interface. Both adverse conditions for electroactive bacteria, which are most efficient in the proximity of the anode due to limited electron transfer distances. These effects were intensified by the overgrowth of the electroactive biofilm with

a supposedly non-electroactive organism in the niche developing at the bulk-biofilm interface, along with its consumption of substrate. The biofilm thickness could be continuously monitored with the DEPOSENS biofilm sensor, especially the surge in biofilm growth as a consequence of the secondary biofilm development. Which of the two affects, substrate limitation or acidic pH, is the predominant cause of the deterioration of the MEC performance could not be distinguished clearly. However, the cause for either limitation is an effect of insufficient mass transport in the biofilm due to too long diffusion pathway or reduced effective diffusion coefficients. Both limitations may occur in the application in technical BES, based on the boundary conditions. Depending on type of substrate and requirements of discharge, for higher substrate concentrations the pH-value is more likely to become the limiting factor. For lower substrate concentration, in wastewater treatment, given the discharge requirements substrate limiting conditions are more probable to occur.

The optimal biofilm thickness found in the experiments of this dissertation must be considered in the light of the boundary conditions. While the biofilm thickness and concentration of substrate will determine the depth of the diffusion pathway, the effective diffusion coefficients depend on the type of substrate, temperature, as well as, biofilm characteristics, including density and porosity. Additionally, the electrical conductivity of the biofilm and electrode/reactor configuration will affect distance for efficient electron transfer. The findings in this dissertation though support the hypothesis of an optimum in the biofilm thickness in the trade-off between the accumulation of electroactive bacteria forming thick biofilms and the mass transport and electron transfer limitations caused thereby. On-line biofilm sensors, such as the DEPOSENS sensor investigated in this dissertation, can effectively monitor the thickness of an electroactive biofilm, which is a simplified but easy to measure biofilm parameter for the identification of mass transport limitations and can support the operational control of BES. Active control of the biofilm thickness should consequently considered for a long-term stable operation of BES. Methods for the promotion of biofilm detachment, by increased shear forces due to flow, gas sparging or even ultrasound have been only scarcely investigated for BES and deserve more focus. Applicable and effective mechanisms should be integrated into upscaled BES in consideration of the reactors construction.

List of Publications

Peer-reviewed publications

Netsch, A.; Latussek, I.; Horn, H.; Wagner, M. Detecting excess biofilm thickness in microbial electrolysis cells by real-time in-situ biofilm monitoring. Biotechnology and Bioengineering, 2025 (submitted)

Netsch, A.; Sen, S. Horn, H.; Wagner, M. In Situ Biofilm Monitoring Using a Heat Transfer Sensor: The Impact of Flow Velocity in a Pipe and Planar System. Biosensors 2025, 15 (2), 93. https://doi.org/10.3390/bios15020093

Netsch, A.; Horn, H.; Wagner, M. On-Line Monitoring of Biofilm Accumulation on Graphite-Polypropylene Electrode Material Using a Heat Transfer Sensor. Biosensors 2022, 12 (1), 18. https://doi.org/10.3390/bios12010018

Conference presentations and posters

Netsch, A., Latussek, I., Horn, H., Wagner, M., 2024. On-line in-situ monitoring of electroactive biofilms in bioelectrochemical systems by means of a heat-transfer biofilm sensor, (Oral presentation) IWA Biofilms for Nutrient Removal and Carbon Neutrality, Shanghai, China.

Netsch, A., Chen, D., Horn, H., Wagner, M., 2024. Integration of denitrification into a single chamber microbial fuel cell (MFC) – nitrate and oxygen competing for electrons, (Poster presentation) IWA Biofilms for Nutrient Removal and Carbon Neutrality, Shanghai, China.

Netsch, A., Wagner, M., Horn, H., 2022. On-line monitoring of biofilm accumulation on graphite-polypropylene electrodes applicable in bioelectrochemical systems using a heat transfer sensor., (Oral Presentation) Biofilms 10 Conference - Ecology meets Technology, Leipzig, Germany.

Bibliography

Babanova, S., Jones, J., Phadke, S., Lu, M., Angulo, C., Garcia, J., Carpenter, K., Cortese, R., Chen, S., Phan, T., and Bretschger, O. (2020). Continuous Flow, Large-scale, Microbial Fuel Cell System for the Sustained Treatment of Swine Waste. *Water Environment Research* 92 (1), 60–72. ISSN: 1061-4303, 1554-7531. DOI: 10.1002/wer.1183.

Babauta, J. T., Nguyen, H. D., Harrington, T. D., Renslow, R., and Beyenal, H. (2012). pH, Redox Potential and Local Biofilm Potential Microenvironments within *Geobacter Sulfurreducens* Biofilms and Their Roles in Electron Transfer. *Biotechnology and Bioengineering* 109 (10), 2651–2662. ISSN: 0006-3592, 1097-0290. DOI: 10.1002/bit.24538.

Belleville, P., Merlin, G., Ramousse, J., and Deseure, J. (2022). Characterization of Spatiotemporal Electroactive Anodic Biofilm Activity Distribution Using 1D Simulations. *Scientific Reports* 12 (1), 5849. ISSN: 2045-2322. DOI: 10.1038/s41598-022-09596-w.

Bierganns, P. and Beardwood, E. (2017). "A New and Novel Abiotic-Biotic Fouling Sensor for Aqueous Systems". In: *Heat Exchanger Fouling and Cleaning*. Heat Exchanger Fouling and Cleaning.

Blatter, M., Delabays, L., Furrer, C., Huguenin, G., Cachelin, C. P., and Fischer, F. (2021). Stretched 1000-L Microbial Fuel Cell. *Journal of Power Sources* 483, 229130. ISSN: 03787753. DOI: 10.1016/j.jpowsour.2020.229130.

Bogaard, R. H. (1985). "Thermal Conductivity of Selected Stainless Steels". In: *Thermal Conductivity 18*. Ed. by T. Ashworth and D. R. Smith. Boston, MA: Springer US, pp. 175–185. ISBN: 978-1-4684-4918-1 978-1-4684-4916-7. DOI: 10.1007/978-1-4684-4916-7_20.

Bonanni, P. S., Bradley, D. F., Schrott, G. D., and Busalmen, J. P. (2013). Limitations for Current Production in *Geobacter Sulfurreducens* Biofilms. *ChemSusChem* 6 (4), 711–720. ISSN: 1864-5631, 1864-564X. DOI: 10.1002/cssc.201200671.

Boukazia, Y., Delaplace, G., Cadé, M., Bellouard, F., Bégué, M., Semmar, N., and Fillaudeau, L. (2020). Metrological Performances of Fouling Sensors Based on Steady Thermal Excitation Applied to Bioprocess. *Food and Bioproducts Processing* 119, 226–237. ISSN: 09603085. DOI: 10.1016/j.fbp.2019.11.007.

Bruijs, M., Venhuis, L., Jenner, H., Daniels, D., and Licina, G. (2001). Biocide Optimization Using an On-Line Biofilm Monitor. *Journal of Power Plant Chemistry* 3 (7), 400–405. ISSN: 1438-5325.

Bullen, R., Arnot, T., Lakeman, J., and Walsh, F. (2006). Biofuel Cells and Their Development. *Biosensors and Bioelectronics* 21 (11), 2015–2045. ISSN: 09565663. DOI: 10.1016/j.bios.2006.01.030.

Butler, C. and Boltz, J. (2014). "Biofilm Processes and Control in Water and Wastewater Treatment". In: *Comprehensive Water Quality and Purification*. Elsevier, pp. 90–107. ISBN: 978-0-12-382183-6. DOI: 10.1016/B978-0-12-382182-9.00083-9.

Characklis, W. G., Nevimons, M. J., and Picologlou, B. F. (1981). Influence of Fouling Biofilms on Heat Transfer. *Heat Transfer Engineering* 3 (1), 23–37. ISSN: 0145-7632, 1521-0537. DOI: 10.1080/01457638108939572.

Characklis, W. G. and Marshall, K. C., eds. (1990). Biofilms. Wiley Series in Ecological and Applied Microbiology. New York: Wiley. ISBN: 978-0-471-82663-7.

Cheng, S. and Logan, B. E. (2011). Increasing Power Generation for Scaling up Single-Chamber Air Cathode Microbial Fuel Cells. *Bioresource Technology* 102 (6), 4468–4473. ISSN: 09608524. DOI: 10.1016/j.biortech.2010.12.104.

Crattelet, J., Ghnimi, S., Debreyne, P., Zaid, I., Boukabache, A., Esteve, D., Auret, L., and Fillaudeau, L. (2013). On-Line Local Thermal Pulse Analysis Sensor to Monitor Fouling and Cleaning: Application to Dairy Product Pasteurisation with an Ohmic Cell Jet Heater. *Journal of Food Engineering* 119 (1), 72–83. ISSN: 02608774. DOI: 10.1016/j.jfoodeng.2013.05.009.

Cussler, E. L. (2009). Diffusion: Mass Transfer in Fluid Systems. 3rd ed. Cambridge ; New York: Cambridge University Press. ISBN: 978-0-521-87121-1.

De Lichtervelde, A., Ter Heijne, A., Hamelers, H., Biesheuvel, P., and Dykstra, J. (2019). Theory of Ion and Electron Transport Coupled with Biochemical Conversions in an Electroactive Biofilm. *Physical Review Applied* 12 (1), 014018. ISSN: 2331-7019. DOI: 10.1103/PhysRevApplied.12.014018.

Dewan, A., Beyenal, H., and Lewandowski, Z. (2008). Scaling up Microbial Fuel Cells. *Environmental Science & Technology* 42 (20), 7643–7648. ISSN: 0013-936X, 1520-5851. DOI: 10.1021/es800775d.

Donlan, R. M. (2002). Biofilms: Microbial Life on Surfaces. *Emerging Infectious Diseases* 8 (9), 881–890. ISSN: 1080-6040, 1080-6059. DOI: 10.3201/eid0809.020063.

Du, Z., Li, H., and Gu, T. (2007). A State of the Art Review on Microbial Fuel Cells: A Promising Technology for Wastewater Treatment and Bioenergy. *Biotechnology Advances* 25 (5), 464–482. ISSN: 07349750. DOI: 10.1016/j.biotechadv.2007.05.004.

Duddridge, J. E., Kent, C. A., and Laws, J. F. (1982). Effect of Surface Shear Stress on the Attachment of *Pseudomonas Fluorescens* to Stainless Steel under Defined Flow Conditions. *Biotechnology and Bioengineering* 24 (1), 153–164. ISSN: 0006-3592, 1097-0290. DOI: 10.1002/bit.260240113.

Dumas, C., Mollica, A., Féron, D., Basséguy, R., Etcheverry, L., and Bergel, A. (2007). Marine Microbial Fuel Cell: Use of Stainless Steel Electrodes as Anode and Cathode Materials. *Electrochimica Acta* 53 (2), 468–473. ISSN: 00134686. DOI: 10.1016/j.electacta.2007.06.069.

Dutta, S. (2007). "Mathematical Modeling of the Performance of a Rotating Biological Contactor for Process Optimisation in Wastewater Treatment". Karlsruhe: Karlsruher Institut für Technologie (KIT).

Edel, M., Horn, H., and Gescher, J. (2019). Biofilm Systems as Tools in Biotechnological Production. *Applied Microbiology and Biotechnology* 103 (13), 5095–5103. ISSN: 0175-7598, 1432-0614. DOI: 10.1007/s00253-019-09869-x.

Engel, C., Schattenberg, F., Dohnt, K., Schröder, U., Müller, S., and Krull, R. (2019). Long-Term Behavior of Defined Mixed Cultures of Geobacter Sulfurreducens and Shewanella Oneidensis in Bioelectrochemical

Systems. *Frontiers in Bioengineering and Biotechnology* 7, 60. ISSN: 2296-4185. DOI: 10.3389/fbioe.2019.00060.

Fan, L.-S., Leyva-Ramos, R., Wisecarver, K. D., and Zehner, B. J. (1990). Diffusion of Phenol through a Biofilm Grown on Activated Carbon Particles in a Draft-tube Three-phase Fluidized-bed Bioreactor. *Biotechnology and Bioengineering* 35 (3), 279–286. ISSN: 0006-3592, 1097-0290. DOI: 10.1002/bit.260350309.

Fillaudeau, L., Crattelet, J., and Auret, L. (2010). "Fouling Monitoring: Local Thermal Analysis". In: *Encyclopedia of Agricultural, Food, and Biological Engineering, Second Edition*. Ed. by D. R. Heldman and C. I. Moraru. CRC Press. ISBN: 978-1-4398-1111-5 978-1-4398-2806-9. DOI: 10.1081/E-EAFE2.

Fischer, M., Triggs, G. J., and Krauss, T. F. (2016). Optical Sensing of Microbial Life on Surfaces. *Applied and Environmental Microbiology* 82 (5). Ed. by H. L. Drake, 1362–1371. ISSN: 0099-2240, 1098-5336. DOI: 10.1128/AEM.03001-15.

Flemming, H.-C. (2003). Role and Levels of Real-Time Monitoring for Successful Anti-Fouling Strategies - an Overview. *Water Science and Technology* 47 (5), 1–8. ISSN: 0273-1223, 1996-9732. DOI: 10.2166/wst.2003.0265.

Flemming, H.-C., Tamachkiarowa, A., Klahre, J., and Schmitt, J. (1998). Monitoring of Fouling and Biofouling in Technical Systems. *Water Science and Technology* 38 (8–9), 291–298. ISSN: 0273-1223, 1996-9732. DOI: 10.2166/wst.1998.0818.

Flemming, H.-C., Wingender, J., Szewzyk, U., Steinberg, P., Rice, S. A., and Kjelleberg, S. (2016). Biofilms: An Emergent Form of Bacterial Life. *Nature Reviews Microbiology* 14 (9), 563–575. ISSN: 1740-1526, 1740-1534. DOI: 10.1038/nrmicro.2016.94.

Flexer, V. and Jourdin, L. (2020). Purposely Designed Hierarchical Porous Electrodes for High Rate Microbial Electrosynthesis of Acetate from Carbon Dioxide. *Accounts of Chemical Research* 53 (2), 311–321. ISSN: 0001-4842, 1520-4898. DOI: 10.1021/acs.accounts.9b00523.

Franks, A. E. and Nevin, K. P. (2010). Microbial Fuel Cells, A Current Review. *Energies* 3 (5), 899–919. ISSN: 1996-1073. DOI: 10.3390/en3050899.

Franks, A. E., Nevin, K. P., Jia, H., Izallalen, M., Woodard, T. L., and Lovley, D. R. (2009). Novel Strategy for Three-Dimensional Real-Time Imaging of Microbial Fuel Cell Communities: Monitoring the Inhibitory Effects of Proton Accumulation within the Anode Biofilm. *Energy Environ. Sci.* 2 (1), 113–119. ISSN: 1754-5692, 1754-5706. DOI: 10.1039/B816445B.

Fricke, K. (2009). Energieeffizenz Kommunaler Kläranlagen. Umweltbundesamt.

Garcia, S., Trueba, A., Vega, L. M., and Madariaga, E. (2018). Quantitative Changes In Biofilms Of A Seawater Tubular Heat Exchanger Subjected To Electromagnetic Fields Treatmentvolume. DOI: 10.5281/ZENODO.1474451.

Ge, Z. and He, Z. (2016). Long-Term Performance of a 200 Liter Modularized Microbial Fuel Cell System Treating Municipal Wastewater: Treatment, Energy, and Cost. *Environmental Science: Water Research & Technology* 2 (2), 274–281. ISSN: 2053-1400, 2053-1419. DOI: 10.1039/C6EW00020G.

Gierl, L., Stoy, K., Faíña, A., Horn, H., and Wagner, M. (2020). An Open-Source Robotic Platform That Enables Automated Monitoring of Replicate Biofilm Cultivations Using Optical Coherence Tomography. *npj Biofilms and Microbiomes* 6 (1), 18. ISSN: 2055-5008. DOI: 10.1038/s41522-020-0129-y.

Gude, V. G. (2016). Wastewater Treatment in Microbial Fuel Cells – an Overview. *Journal of Cleaner Production* 122, 287–307. ISSN: 09596526. DOI: 10.1016/j.jclepro.2016.02.022.

Gujer, W. (2007). Siedlungswasserwirtschaft. Springer Berlin Heidelberg. ISBN: 978-3-540-34329-5. DOI: 10.1007/978-3-540-34330-1.

Hackbarth, M., Gescher, J., Horn, H., and Reiner, J. E. (2023). A Scalable, Rotating Disc Bioelectrochemical Reactor (RDBER) Suitable for the Cultivation of Both Cathodic and Anodic Biofilms. *Bioresource Technology Reports* 21, 101357. ISSN: 2589014X. DOI: 10.1016/j.biteb.2023.101357.

Hackbarth, M., Jung, T., Reiner, J. E., Gescher, J., Horn, H., Hille-Reichel, A., and Wagner, M. (2020). Monitoring and Quantification of Bioelectrochemical Kyrpidia Spormannii Biofilm Development in a Novel Flow Cell Setup. *Chemical Engineering Journal* 390, 124604. ISSN: 13858947. DOI: 10.1016/j.cej.2020.124604.

Harnisch, F. and Holtmann, D., eds. (2019). Bioelectrosynthesis. Vol. 167. Advances in Biochemical Engineering/Biotechnology. Cham: Springer International Publishing. ISBN: 978-3-030-03298-2 978-3-030-03299-9. DOI: 10.1007/978-3-030-03299-9.

Harnisch, F. and Schröder, U. (2010). From MFC to MXC: Chemical and Biological Cathodes and Their Potential for Microbial Bioelectrochemical Systems. *Chemical Society Reviews* 39 (11), 4433. ISSN: 0306-0012, 1460-4744. DOI: 10.1039/c003068f.

Haupt, D. R., Landwehr, L., Schumann, R., Hahn, L., Issa, M., Coskun, C., Kunz, U., and Sievers, M. (2022). A New Reactor Concept for Single-Chamber Microbial Fuel Cells and Possible Anti-Fouling Strategies for Long-Term Operation. *Microorganisms* 10 (12), 2421. ISSN: 2076-2607. DOI: 10.3390/microorganisms10122421.

Heinrichmeier, J., Littfinski, T., Vasyukova, E., Steuernagel, L., and Wichern, M. (2023). On-Site Performance Evaluation of a 1,000-Litre Microbial Fuel Cell System Using Submergible Multi-Electrode Modules with Air-Cathodes for Sustainable Municipal Wastewater Treatment and Electricity Generation. *Water Science & Technology* 87 (8), 1969–1981. ISSN: 0273-1223, 1996-9732. DOI: 10.2166/wst.2023.106.

Horn, H. and Morgenroth, E. (2006). Transport of Oxygen, Sodium Chloride, and Sodium Nitrate in Biofilms. *Chemical Engineering Science* 61 (5), 1347–1356. ISSN: 00092509. DOI: 10.1016/j.ces.2005.08.027.

Hwang, J. H., Cicek, N., and Oleszkiewicz, J. A. (2010). Achieving Biofilm Control in a Membrane Biofilm Reactor Removing Total Nitrogen. *Water Research* 44 (7), 2283–2291. ISSN: 00431354. DOI: 10.1016/j.watres.2009.12.022.

Ieropoulos, I. A., Singh, A., Zertuche Moreno, D., and Greenman, J. (2024). Bioelectrochemical Systems and Their Readiness for Commercialisation. *Current Opinion in Electrochemistry* 46, 101540. ISSN: 24519103. DOI: 10.1016/j.coelec.2024.101540.

Islam, M. A., Woon, C. W., Ethiraj, B., Cheng, C. K., Yousuf, A., and Khan, M. M. R. (2017). Ultrasound Driven Biofilm Removal for Stable Power Generation in Microbial Fuel Cell. *Energy & Fuels* 31 (1), 968–976. ISSN: 0887-0624, 1520-5029. DOI: 10.1021/acs.energyfuels.6b02294.

Islam, M. A., Ehiraj, B., Cheng, C. K., Dubey, B. N., and Khan, M. M. R. (2019). Biofilm Re-Vitalization Using Hydrodynamic Shear Stress for Stable Power Generation in Microbial Fuel Cell. *Journal of Electroanalytical Chemistry* 844, 14–22. ISSN: 15726657. DOI: 10.1016/j.jelechem.2019.05.013.

Jain, A., Gazzola, G., Panzera, A., Zanoni, M., and Marsili, E. (2011). Visible Spectroelectrochemical Characterization of Geobacter Sulfurreducens Biofilms on Optically Transparent Indium Tin Oxide Electrode. *Electrochimica Acta* 56 (28), 10776–10785. ISSN: 00134686. DOI: 10.1016/j.electacta.2011.02.073.

Janknecht, P. and Melo, L. F. (2003). Online Biofilm Monitoring. *Reviews in Environmental Science and Bio/Technology* 2 (2–4), 269–283. ISSN: 1569-1705. DOI: 10.1023/B:RESB.0000040461.69339.04.

Jourdin, L., Sousa, J., Stralen, N. V., and Strik, D. P. (2020). Techno-Economic Assessment of Microbial Electrosynthesis from CO2 and/or Organics: An Interdisciplinary Roadmap towards Future Research and Application. *Applied Energy* 279, 115775. ISSN: 03062619. DOI: 10.1016/j.apenergy.2020.115775.

Kalathil, S., Patil, S., and Pant, D. (2018). "Microbial Fuel Cells: Electrode Materials". In: *Encyclopedia of Interfacial Chemistry*. Elsevier, pp. 309–318. ISBN: 978-0-12-809894-3. DOI: 10.1016/B978-0-12-409547-2.13459-6.

Kato Marcus, A., Torres, C. I., and Rittmann, B. E. (2007). Conduction-Based Modeling of the Biofilm Anode of a Microbial Fuel Cell. *Biotechnology and Bioengineering* 98 (6), 1171–1182. ISSN: 00063592, 10970290. DOI: 10.1002/bit.21533.

Katuri, K. P., Kamireddy, S., Kavanagh, P., Muhammad, A., Conghaile, P. Ó., Kumar, A., Saikaly, P. E., and Leech, D. (2020). Electroactive Biofilms on Surface Functionalized Anodes: The Anode Respiring Behavior of a Novel Electroactive Bacterium, Desulfuromonas Acetexigens. *Water Research* 185, 116284. ISSN: 00431354. DOI: 10.1016/j.watres.2020.116284.

Kitayama, M., Koga, R., Kasai, T., Kouzuma, A., and Watanabe, K. (2017). Structures, Compositions, and Activities of Live Shewanella Biofilms Formed on Graphite Electrodes in Electrochemical Flow Cells. *Applied and Environmental Microbiology* 83 (17). Ed. by R. M. Kelly, e00903–17. ISSN: 0099-2240, 1098-5336. DOI: 10.1128/AEM.00903-17.

Korth, B., Rosa, L. F., Harnisch, F., and Picioreanu, C. (2015). A Framework for Modeling Electroactive Microbial Biofilms Performing Direct Electron Transfer. *Bioelectrochemistry* 106, 194–206. ISSN: 15675394. DOI: 10.1016/j.bioelechem.2015.03.010.

Lewandowski, Z. and Boltz, J. (2011). "Biofilms in Water and Wastewater Treatment". In: *Treatise on Water Science*. Elsevier, pp. 529–570. ISBN: 978-0-444-53199-5. DOI: 10.1016/B978-0-444-53199-5.00095-6.

Li, J., Hu, L., Zhang, L., Ye, D.-d., Zhu, X., and Liao, Q. (2017). Uneven Biofilm and Current Distribution in Three-Dimensional Macroporous Anodes of Bio-Electrochemical Systems Composed of Graphite Electrode Arrays. *Bioresource Technology* 228, 25–30. ISSN: 09608524. DOI: 10.1016/j.biortech.2016.12.092.

Lin, W. C., Coppi, M. V., and Lovley, D. R. (2004). *Geobacter Sulfurreducens* Can Grow with Oxygen as a Terminal Electron Acceptor. *Applied and Environmental Microbiology* 70 (4), 2525–2528. ISSN: 0099-2240, 1098-5336. DOI: 10.1128/aem.70.4.2525-2528.2004.

Liu, H. and Zhao, X. (2022). Thermal Conductivity Analysis of High Porosity Structures with Open and Closed Pores. *International Journal of Heat and Mass Transfer* 183, 122089. ISSN: 00179310. DOI: 10.1016/j.ijheatmasstransfer.2021.122089.

Logan, B. E. (2007). Microbial Fuel Cells. 1st ed. Wiley. ISBN: 978-0-470-23948-3 978-0-470-25859-0. DOI: 10.1002/9780470258590.

Logan, B. E. (2010). Scaling up Microbial Fuel Cells and Other Bioelectrochemical Systems. *Applied Microbiology and Biotechnology* 85 (6), 1665–1671. ISSN: 0175-7598, 1432-0614. DOI: 10.1007/s00253-009-2378-9.

Logan, B. E., Hamelers, B., Rozendal, R., Schröder, U., Keller, J., Freguia, S., Aelterman, P., Verstraete, W., and Rabaey, K. (2006). Microbial Fuel Cells: Methodology and Technology. *Environmental Science & Technology* 40 (17), 5181–5192. ISSN: 0013-936X, 1520-5851. DOI: 10.1021/es0605016.

Malvankar, N. S., Vargas, M., Nevin, K. P., Franks, A. E., Leang, C., Kim, B.-C., Inoue, K., Mester, T., Covalla, S. F., Johnson, J. P., Rotello, V. M., Tuominen, M. T., and Lovley, D. R. (2011). Tunable Metallic-like Conductivity in Microbial Nanowire Networks. *Nature Nanotechnology* 6 (9), 573–579. ISSN: 1748-3387, 1748-3395. DOI: 10.1038/nnano.2011.119.

Mateo, S., Cañizares, P., Fernandez-Morales, F. J., and Rodrigo, M. A. (2018). A Critical View of Microbial Fuel Cells: What Is the Next Stage? *ChemSusChem* 11 (24), 4183–4192. ISSN: 1864-5631, 1864-564X. DOI: 10.1002/cssc.201802187.

Maurício, R., Dias, C. J., Jubilado, N., and Santana, F. (2013). Biofilm Thickness Measurement Using an Ultrasound Method in a Liquid Phase. *Environmental Monitoring and Assessment* 185 (10), 8125–8133. ISSN: 0167-6369, 1573-2959. DOI: 10.1007/s10661-013-3160-0.

Molenaar, S. D., Sleutels, T., Pereira, J., Iorio, M., Borsje, C., Zamudio, J. A., Fabregat-Santiago, F., Buisman, C. J. N., and ter Heijne, A. (2018). In Situ Biofilm Quantification in Bioelectrochemical Systems by Using Optical Coherence Tomography. *ChemSusChem* 11 (13), 2171–2178. ISSN: 1864-5631, 1864-564X. DOI: 10.1002/cssc.201800589.

Mollica, A. and Cristiani, P. (2003). On-Line Biofilm Monitoring by "BIOX" Electrochemical Probe. *Water Science and Technology: A Journal of the International Association on Water Pollution Research* 47 (5), 45–49. ISSN: 0273-1223. pmid: 12701905.

Muddemann, T., Haupt, D. R., Gomes Silva E Silva, L., Jiang, B., Kunz, U., Bormann, H., Niedermeiser, M., Schlaefer, O., and Sievers, M. (2017). Integration of Upscaled Microbial Fuel Cells in Real Municipal Sewage Plants. *ECS Transactions* 77 (11), 1053–1077. ISSN: 1938-6737, 1938-5862. DOI: 10.1149/07711.1053ecst.

Muffler, K. and Ulber, R., eds. (2014). Productive Biofilms. Vol. 146. Advances in Biochemical Engineering/Biotechnology. Cham: Springer International Publishing. ISBN: 978-3-319-09694-0 978-3-319-09695-7. DOI: 10.1007/978-3-319-09695-7.

Murga, R., Stewart, P. S., and Daly, D. (1995). Quantitative Analysis of Biofilm Thickness Variability. *Biotechnology and Bioengineering* 45 (6), 503–510. ISSN: 0006-3592, 1097-0290. DOI: 10.1002/bit.260450607.

Mustakeem (2015). Electrode Materials for Microbial Fuel Cells: Nanomaterial Approach. *Materials for Renewable and Sustainable Energy* 4 (4), 22. ISSN: 2194-1459, 2194-1467. DOI: 10.1007/s40243-015-0063-8.

Nam, J.-Y., Tokash, J. C., and Logan, B. E. (2011). Comparison of Microbial Electrolysis Cells Operated with Added Voltage or by Setting the Anode Potential. *International Journal of Hydrogen Energy* 36 (17), 10550–10556. ISSN: 03603199. DOI: 10.1016/j.ijhydene.2011.05.148.

Netsch, A., Horn, H., and Wagner, M. (2021). On-Line Monitoring of Biofilm Accumulation on Graphite-Polypropylene Electrode Material Using a Heat Transfer Sensor. *Biosensors* 12 (1), 18. ISSN: 2079-6374. DOI: 10.3390/bios12010018.

Netsch, A., Sen, S., Horn, H., and Wagner, M. (2025). In Situ Biofilm Monitoring Using a Heat Transfer Sensor: The Impact of Flow Velocity in a Pipe and Planar System. *Biosensors* 15 (2), 93. ISSN: 2079-6374. DOI: 10.3390/bios15020093.

Neu, T. R. and Lawrence, J. R. (2015). Innovative Techniques, Sensors, and Approaches for Imaging Biofilms at Different Scales. *Trends in Microbiology* 23 (4), 233–242. ISSN: 0966842X. DOI: 10.1016/j.tim.2014.12.010.

Neu, T. R., Manz, B., Volke, F., Dynes, J. J., Hitchcock, A. P., and Lawrence, J. R. (2010). Advanced Imaging Techniques for Assessment of Structure, Composition and Function in Biofilm Systems. *FEMS Microbiology Ecology* 72 (1), 1–21. ISSN: 01686496, 15746941. DOI: 10.1111/j.1574-6941.2010.00837.x.

Nevin, K. P., Richter, H., Covalla, S. F., Johnson, J. P., Woodard, T. L., Orloff, A. L., Jia, H., Zhang, M., and Lovley, D. R. (2008). Power Output and Columbic Efficiencies from Biofilms of *Geobacter Sulfurreducens* Comparable to Mixed Community Microbial Fuel Cells. *Environmental Microbiology* 10 (10), 2505–2514. ISSN: 1462-2912, 1462-2920. DOI: 10.1111/j.1462-2920.2008.01675.x.

Nivens, D. E., Palmer, R. J., and White, D. C. (1995). Continuous Nondestructive Monitoring of Microbial Biofilms: A Review of Analytical Techniques. *Journal of Industrial Microbiology* 15 (4), 263–276. ISSN: 0169-4146, 1476-5535. DOI: 10.1007/BF01569979.

Oliveira, V., Simões, M., Melo, L., and Pinto, A. (2013). A 1D Mathematical Model for a Microbial Fuel Cell. *Energy* 61, 463–471. ISSN: 03605442. DOI: 10.1016/j.energy.2013.08.055.

Pandey, P., Shinde, V. N., Deopurkar, R. L., Kale, S. P., Patil, S. A., and Pant, D. (2016). Recent Advances in the Use of Different Substrates in Microbial Fuel Cells toward Wastewater Treatment and Simultaneous Energy Recovery. *Applied Energy* 168, 706–723. ISSN: 0306-2619. DOI: 10.1016/j.apenergy.2016.01.056.

Patil, S. A., Harnisch, F., Koch, C., Hübschmann, T., Fetzer, I., Carmona-Martínez, A. A., Müller, S., and Schröder, U. (2011). Electroactive Mixed Culture Derived Biofilms in Microbial Bioelectrochemical Systems: The Role of pH on Biofilm Formation, Performance and Composition. *Bioresource Technology* 102 (20), 9683–9690. ISSN: 09608524. DOI: 10.1016/j.biortech.2011.07.087.

Pavanello, G., Faimali, M., Pittore, M., Mollica, A., Mollica, A., and Mollica, A. (2011). Exploiting a New Electrochemical Sensor for Biofilm Monitoring and Water Treatment Optimization. *Water Research* 45 (4), 1651–1658. ISSN: 00431354. DOI: 10.1016/j.watres.2010.12.003.

Pereira, A. and Melo, L. F. (2023). Online Biofilm Monitoring Is Missing in Technical Systems: How to Build Stronger Case-Studies? *npj Clean Water* 6 (1), 36. ISSN: 2059-7037. DOI: 10.1038/s41545-023-00249-7.

Pereira, J., De Nooy, S., Sleutels, T., and Ter Heijne, A. (2022a). Opportunities for Visual Techniques to Determine Characteristics and Limitations of Electro-Active Biofilms. *Biotechnology Advances* 60, 108011. ISSN: 07349750. DOI: 10.1016/j.biotechadv.2022.108011.

Pereira, J., Pang, S., Borsje, C., Sleutels, T., Hamelers, B., and Ter Heijne, A. (2022b). Real-Time Monitoring of Biofilm Thickness Allows for Determination of Acetate Limitations in Bio-Anodes. *Bioresource Technology Reports* 18, 101028. ISSN: 2589014X. DOI: 10.1016/j.biteb.2022.101028.

Pereira, J., Wang, G., Sleutels, T., Hamelers, B., and Ter Heijne, A. (2022c). Maximum Thickness of Non-Buffer Limited Electro-Active Biofilms Decreases at Higher Anode Potentials. *Biofilm* 4, 100092. ISSN: 25902075. DOI: 10.1016/j.bioflm.2022.100092.

Philipp, L.-A., Bühler, K., Ulber, R., and Gescher, J. (2024). Beneficial Applications of Biofilms. *Nature Reviews Microbiology* 22 (5), 276–290. ISSN: 1740-1526, 1740-1534. DOI: 10.1038/s41579-023-00985-0.

Picioreanu, C., Van Loosdrecht, M. C., Curtis, T. P., and Scott, K. (2010). Model Based Evaluation of the Effect of pH and Electrode Geometry on Microbial Fuel Cell Performance. *Bioelectrochemistry* 78 (1), 8–24. ISSN: 15675394. DOI: 10.1016/j.bioelechem.2009.04.009.

Pinck, S., Ostormujof, L. M., Teychené, S., and Erable, B. (2020). Microfluidic Microbial Bioelectrochemical Systems: An Integrated Investigation Platform for a More Fundamental Understanding of Electroactive Bacterial Biofilms. *Microorganisms* 8 (11), 1841. ISSN: 2076-2607. DOI: 10.3390/microorganisms8111841.

Pires, L., Sachsenheimer, K., Kleintschek, T., Waldbaur, A., Schwartz, T., and Rapp, B. E. (2013). Online Monitoring of Biofilm Growth and Activity Using a Combined Multi-Channel Impedimetric and Amperometric Sensor. *Biosensors and Bioelectronics* 47, 157–163. ISSN: 09565663. DOI: 10.1016/j.bios.2013.03.015.

Poma, N., Vivaldi, F., Bonini, A., Salvo, P., Kirchhain, A., Ates, Z., Melai, B., Bottai, D., Tavanti, A., and Di Francesco, F. (2021). Microbial Biofilm Monitoring by Electrochemical Transduction Methods. *TrAC Trends in Analytical Chemistry* 134, 116134. ISSN: 01659936. DOI: 10.1016/j.trac.2020.116134.

Potter, M. (1911). Electrical Effects Accompanying the Decomposition of Organic Compounds. *Proceedings of the Royal Society of London. Series B, Containing Papers of a Biological Character* 84 (571), 260–276. ISSN: 0950-1193, 2053-9185. DOI: 10.1098/rspb.1911.0073.

Pratofiorito, G., Horn, H., and Saravia, F. (2024). Application of Online Biofilm Sensors for Membrane Performance Assessment in High Organic Load Reverse Osmosis Feed Streams. *Separation and Purification Technology* 330, 125200. ISSN: 13835866. DOI: 10.1016/j.seppur.2023.125200.

Rahardianto, A., Gu, H., Khan, B. M., and Plumlee, M. H. (2020). Real-time Reverse Osmosis Monitoring for Antiscalant Dose Selection in Advanced Treatment of Wastewater. *AWWA Water Science* 2 (5), e1196. ISSN: 2577-8161, 2577-8161. DOI: 10.1002/aws2.1196.

Rahimnejad, M., Najafpour, G., Ghoreyshi, A., Shakeri, M., and Zare, H. (2011). Methylene Blue as Electron Promoters in Microbial Fuel Cell. *International Journal of Hydrogen Energy* 36 (20), 13335–13341. ISSN: 0360-3199. DOI: 10.1016/j.ijhydene.2011.07.059.

Rani, A., Snyder, S. W., Kim, H., Lei, Z., and Pan, S.-Y. (2022). Pathways to a Net-Zero-Carbon Water Sector through Energy-Extracting Wastewater Technologies. *npj Clean Water* 5 (1), 49. ISSN: 2059-7037. DOI: 10.1038/s41545-022-00197-8.

Rawat, A. and Shandilya, S. (2020). Effectiveness of Microbial Fuel Cell in Sustainable Energy Production during Wastewater Treatment: A Mini Review. *The Pharma Innovation* 9 (2), 495–498. ISSN: 23498242, 22777695. DOI: 10.22271/tpi.2020.v9.i2i.4444.

Read, S. T., Dutta, P., Bond, P. L., Keller, J., and Rabaey, K. (2010). Initial Development and Structure of Biofilms on Microbial Fuel Cell Anodes. *BMC Microbiology* 10 (1), 98. ISSN: 1471-2180. DOI: 10.1186/1471-2180-10-98.

Recupido, F., Toscano, G., Tatè, R., Petala, M., Caserta, S., Karapantsios, T. D., and Guido, S. (2020). The Role of Flow in Bacterial Biofilm Morphology and Wetting Properties. *Colloids and Surfaces B: Biointerfaces* 192, 111047. ISSN: 09277765. DOI: 10.1016/j.colsurfb.2020.111047.

Reguera, G. (2018). Microbial Nanowires and Electroactive Biofilms. *FEMS Microbiology Ecology* 94 (7). ISSN: 1574-6941. DOI: 10.1093/femsec/fiy086.

Reguera, G., Nevin, K. P., Nicoll, J. S., Covalla, S. F., Woodard, T. L., and Lovley, D. R. (2006). Biofilm and Nanowire Production Leads to Increased Current in *Geobacter Sulfurreducens* Fuel Cells. *Applied and Environmental Microbiology* 72 (11), 7345–7348. ISSN: 0099-2240, 1098-5336. DOI: 10.1128/AEM.01444-06.

Renslow, R. S., Babauta, J. T., Dohnalkova, A. C., Boyanov, M. I., Kemner, K. M., Majors, P. D., Fredrickson, J. K., and Beyenal, H. (2013). Metabolic Spatial Variability in Electrode-Respiring Geobacter Sulfurreducens Biofilms. *Energy & Environmental Science* 6 (6), 1827. ISSN: 1754-5692, 1754-5706. DOI: 10.1039/c3ee40203g.

Renslow, R. S., Majors, P. D., McLean, J. S., Fredrickson, J. K., Ahmed, B., and Beyenal, H. (2010). In Situ Effective Diffusion Coefficient Profiles in Live Biofilms Using Pulsed-field Gradient Nuclear Magnetic Resonance. *Biotechnology and Bioengineering* 106 (6), 928–937. ISSN: 0006-3592, 1097-0290. DOI: 10.1002/bit.22755.

Reyes-Romero, D., Behrmann, O., Dame, G., and Urban, G. (2014). Dynamic Thermal Sensor for Biofilm Monitoring. *Sensors and Actuators A: Physical* 213, 43–51. ISSN: 09244247. DOI: 10.1016/j.sna.2014.03.032.

Römling, U. (2023). Is Biofilm Formation Intrinsic to the Origin of Life? *Environmental Microbiology* 25 (1), 26–39. ISSN: 1462-2912, 1462-2920. DOI: 10.1111/1462-2920.16179.

Rosenbaum, M., Aulenta, F., Villano, M., and Angenent, L. T. (2011). Cathodes as Electron Donors for Microbial Metabolism: Which Extracellular Electron Transfer Mechanisms Are Involved? *Bioresource Technology* 102 (1), 324–333. ISSN: 09608524. DOI: 10.1016/j.biortech.2010.07.008.

Santoro, C., Arbizzani, C., Erable, B., and Ieropoulos, I. (2017). Microbial Fuel Cells: From Fundamentals to Applications. A Review. *Journal of Power Sources* 356, 225–244. ISSN: 03787753. DOI: 10.1016/j.jpowsour.2017.03.109.

Santoro, C., Babanova, S., Cristiani, P., Artyushkova, K., Atanassov, P., Bergel, A., Bretschger, O., Brown, R. K., Carpenter, K., Colombo, A., Cortese, R., Erable, B., Harnisch, F., Kodali, M., Phadke, S., Riedl, S., Rosa, L. F. M., and Schröder, U. (2021). Front Cover: How Comparable Are Microbial Electrochemical Systems around the Globe? An Electrochemical and Microbiological Cross-Laboratory Study (ChemSusChem 11/2021). *ChemSusChem* 14 (11), 2262–2262. ISSN: 1864-5631, 1864-564X. DOI: 10.1002/cssc.202100825.

Sapireddy, V., Katuri, K. P., Muhammad, A., and Saikaly, P. E. (2021). Competition of Two Highly Specialized and Efficient Acetoclastic Electroactive Bacteria for Acetate in Biofilm Anode of Microbial Electrolysis Cell. *npj Biofilms and Microbiomes* 7 (1), 47. ISSN: 2055-5008. DOI: 10.1038/s41522-021-00218-3.

Schmid, T., Helmbrecht, C., Panne, U., Haisch, C., and Niessner, R. (2003). Process Analysis of Biofilms by Photoacoustic Spectroscopy. *Analytical and Bioanalytical Chemistry* 375 (8), 1124–1129. ISSN: 1618-2642. DOI: 10.1007/s00216-002-1690-3.

Schröder, U. (2007). Anodic Electron Transfer Mechanisms in Microbial Fuel Cells and Their Energy Efficiency. *Phys. Chem. Chem. Phys.* 9 (21), 2619–2629. ISSN: 1463-9076, 1463-9084. DOI: 10.1039/B703627M.

Sehar, S. and Naz, I. (2016). "Role of the Biofilms in Wastewater Treatment". In: *Microbial Biofilms - Importance and Applications*. Ed. by D. Dhanasekaran and N. Thajuddin. InTech. ISBN: 978-953-51-2435-1 978-953-51-2436-8. DOI: 10.5772/63499.

Semenec, L., E Franks, A., and Department of Physiology, Anatomy and Microbiology, Faculty of Science, Technology & Engineering, La Trobe University, Melbourne, Victoria, 3086, Australia (2015). Delving through Electrogenic Biofilms: From Anodes to Cathodes to Microbes. *AIMS Bioengineering* 2 (3), 222–248. ISSN: 2375-1495. DOI: 10.3934/bioeng.2015.3.222.

Settu, K., Chen, C.-J., Liu, J.-T., Chen, C.-L., and Tsai, J.-Z. (2015). Impedimetric Method for Measuring Ultra-Low E. Coli Concentrations in Human Urine. *Biosensors and Bioelectronics* 66, 244–250. ISSN: 09565663. DOI: 10.1016/j.bios.2014.11.027.

Slate, A. J., Whitehead, K. A., Brownson, D. A., and Banks, C. E. (2019). Microbial Fuel Cells: An Overview of Current Technology. *Renewable and Sustainable Energy Reviews* 101, 60–81. ISSN: 13640321. DOI: 10.1016/j.rser.2018.09.044.

Sleutels, T., Molenaar, S., Heijne, A., and Buisman, C. (2016). Low Substrate Loading Limits Methanogenesis and Leads to High Coulombic Efficiency in Bioelectrochemical Systems. *Microorganisms* 4 (1), 7. ISSN: 2076-2607. DOI: 10.3390/microorganisms4010007.

Smith, D. S., Alzina, A., Bourret, J., Nait-Ali, B., Pennec, F., Tessier-Doyen, N., Otsu, K., Matsubara, H., Elser, P., and Gonzenbach, U. T. (2013). Thermal Conductivity of Porous Materials. *Journal of Materials Research* 28 (17), 2260–2272. ISSN: 0884-2914, 2044-5326. DOI: 10.1557/jmr.2013.179.

Stewart, P. S. (2003). Diffusion in Biofilms. *Journal of Bacteriology* 185 (5), 1485–1491. ISSN: 0021-9193, 1098-5530. DOI: 10.1128/JB.185.5.1485-1491.2003.

Stoodley, P., Dodds, I., Boyle, J., and Lappin-Scott, H. (1998). Influence of Hydrodynamics and Nutrients on Biofilm Structure. *Journal of Applied Microbiology* 85 (S1), 19S–28S. ISSN: 13645072. DOI: 10.1111/j.1365-2672.1998.tb05279.x.

Strathmann, M., Mittenzwey, K.-H., Sinn, G., Papadakis, W., and Flemming, H.-C. (2013). Simultaneous Monitoring of Biofilm Growth, Microbial Activity, and Inorganic Deposits on Surfaces with an in Situ , Online, Real-Time, Non-Destructive, Optical Sensor. *Biofouling* 29 (5), 573–583. ISSN: 0892-7014, 1029-2454. DOI: 10.1080/08927014.2013.791287.

Sun, D., Chen, J., Huang, H., Liu, W., Ye, Y., and Cheng, S. (2016). The Effect of Biofilm Thickness on Electrochemical Activity of Geobacter Sulfurreducens. *International Journal of Hydrogen Energy* 41 (37), 16523–16528. ISSN: 03603199. DOI: 10.1016/j.ijhydene.2016.04.163.

Torres, C. I., Kato Marcus, A., and Rittmann, B. E. (2008). Proton Transport inside the Biofilm Limits Electrical Current Generation by Anode-respiring Bacteria. *Biotechnology and Bioengineering* 100 (5), 872–881. ISSN: 0006-3592, 1097-0290. DOI: 10.1002/bit.21821.

Trueba, A., García, S., Otero, F. M., Vega, L. M., and Madariaga, E. (2015). Influence of Flow Velocity on Biofilm Growth in a Tubular Heat Exchanger-Condenser Cooled by Seawater. *Biofouling* 31 (6), 527–534. ISSN: 0892-7014, 1029-2454. DOI: 10.1080/08927014.2015.1070404.

Tsagkari, E., Connelly, S., Liu, Z., McBride, A., and Sloan, W. T. (2022). The Role of Shear Dynamics in Biofilm Formation. *npj Biofilms and Microbiomes* 8 (1), 33. ISSN: 2055-5008. DOI: 10.1038/s41522-022-00300-4.

Ullah, Z. and Zeshan, S. (2020). Effect of Substrate Type and Concentration on the Performance of a Double Chamber Microbial Fuel Cell. *Water Science and Technology* 81 (7), 1336–1344. ISSN: 0273-1223, 1996-9732. DOI: 10.2166/wst.2019.387.

Verein Deutscher Ingenieure (2013). VDI-Wärmeatlas: mit 320 Tabellen. 11., bearb. und erw. Aufl. Springer Reference. Berlin Heidelberg: Springer Vieweg. ISBN: 978-3-642-19980-6 978-3-642-19982-0.

Virdis, B., Rabaey, K., Rozendal, R., Yuan, Z., Mu, Y., and Keller, J. (2010). Simultaneous Nitrification and Denitrification (SND) at a Microbial Fuel Cell (MFC) Biocathode. *Journal of Biotechnology* 150, 153–154. ISSN: 01681656. DOI: 10.1016/j.jbiotec.2010.08.398.

Virdis, B., Rabaey, K., Yuan, Z., and Keller, J. (2008). Microbial Fuel Cells for Simultaneous Carbon and Nitrogen Removal. *Water Research* 42 (12), 3013–3024. ISSN: 00431354. DOI: 10.1016/j.watres.2008.03.017.

Wagner, M. and Horn, H. (2017). Online Erfassung, Behandlung und Reduktion der Biofilm-Bildung sowie anorganischen Ablagerungen in mit vorgeklärtem Abwasser betriebenen Bewässerungssystemen (BioScIrr). Abschlussbericht. DVGW-Forschungsstelle, Wasserchemie und Wassertechnologie am Engler-Bunte-Institut,

Wei, C.-H., Zhai, X.-Y., Jiang, Y.-D., Rong, H.-W., Zhao, L.-G., Liang, P., Huang, X., and Ngo, H. H. (2024). Simultaneous Carbon, Nitrogen and Phosphorus Removal in Sequencing Batch Membrane Aerated Biofilm Reactor with Biofilm Thickness Control via Air Scouring Aided by Computational Fluid Dynamics. *Bioresource Technology* 409, 131267. ISSN: 09608524. DOI: 10.1016/j.biortech.2024.131267.

Wieland, T., Assmann, J., Bethe, A., Fidelak, C., Gmoser, H., Janßen, T., Kotthaus, K., Lübke-Becker, A., Wieler, L. H., and Urban, G. A. (2021). A Real-Time Thermal Sensor System for Quantifying the Inhibitory Effect of Antimicrobial Peptides on Bacterial Adhesion and Biofilm Formation. *Sensors* 21 (8), 2771. ISSN: 1424-8220. DOI: 10.3390/s21082771.

Wu, Y., Li, F., Liu, T., Han, R., and Luo, X. (2016). pH Dependence of Quinone-Mediated Extracellular Electron Transfer in a Bioelectrochemical System. *Electrochimica Acta* 213, 408–415. ISSN: 00134686. DOI: 10.1016/j.electacta.2016.07.122.

Yang, J., Cheng, S., Li, C., Sun, Y., and Huang, H. (2019). Shear Stress Affects Biofilm Structure and Consequently Current Generation of Bioanode in Microbial Electrochemical Systems (MESs). *Frontiers in Microbiology* 10, 398. ISSN: 1664-302X. DOI: 10.3389/fmicb.2019.00398.

Yang, W., Li, J., Fu, Q., Zhang, L., Wei, Z., Liao, Q., and Zhu, X. (2021). Minimizing Mass Transfer Losses in Microbial Fuel Cells: Theories, Progresses and Prospectives. *Renewable and Sustainable Energy Reviews* 136, 110460. ISSN: 13640321. DOI: 10.1016/j.rser.2020.110460.

Yaqoob, A. A., Mohamad Ibrahim, M. N., Rafatullah, M., Chua, Y. S., Ahmad, A., and Umar, K. (2020). Recent Advances in Anodes for Microbial Fuel Cells: An Overview. *Materials* 13 (9), 2078. ISSN: 1996-1944. DOI: 10.3390/ma13092078.

Zhang, E., Wang, F., Yu, Q., Scott, K., Wang, X., and Diao, G. (2017). Durability and Regeneration of Activated Carbon Air-Cathodes in Long-Term Operated Microbial Fuel Cells. *Journal of Power Sources* 360, 21–27. ISSN: 03787753. DOI: 10.1016/j.jpowsour.2017.05.119.

Zhang, Y. and Angelidaki, I. (2014). Microbial Electrolysis Cells Turning to Be Versatile Technology: Recent Advances and Future Challenges. *Water Research* 56, 11–25. ISSN: 00431354. DOI: 10.1016/j.watres.2014.02.031.

Appendix

A Supplementary Information to Chapter 3

Detailed List of conducted experiments

Table A.1: Overview of the different experimental runs

experiment no.	Q (L/min)	Re (-)	ΔT (K)	number of pipes SST/C/PP
A			10	4/4
B			10	5/5
C1			10	1/1
C2			5	2/2
C3	3.6	3000	2	2/2
D1			10	1/1
D2			5	2/2
D3			2	2/2
E			5	5/5

Statistical Analysis

Table A.2: Results of the Shapiro-Wilk and Kolmogorov-Smirnov tests for the parameters mean biofilm thickness, mean biofilm density and fraction of inorganic compounds at the sensor setting ΔT=10 K for both pipe materials.

pipe material	parameter	n	p-value (Shapiro-Wilk)	p-value (Kolmogorov-Smirnov)
C-PP	mean biofilm thickness $\overline{L}_F$	8	0.337	0.560
	mean biofilm density		0.140	0.886
	fraction of inorganic compounds		0.177	0.902
SST	mean biofilm thickness $\overline{L}_F$	9	0.300	0.739
	mean biofilm density		0.004	0.286
	fraction of inorganic compounds		0.003	0.469

In combination with a Grubbs test the statistical analysis revealed one data set of outliers for the mean biofilm density and fraction of inorganic compounds of the SST pipe material. This data set was excluded from the analysis.

In addition the Grubbs test did not reveal any outliers for the data sets of either of the pipe materials at the ΔT=5K setting of the sensor.

Table A.3: Results of the Shapiro-Wilk and Kolmogorov-Smirnov tests for the parameters mean biofilm thickness, mean biofilm density and fraction of inorganic compounds at the sensor setting ΔT=5 K for both pipe materials.

pipe material	parameter	n	p-value (Shapiro-Wilk)	p-value (Kolmogorov-Smirnov)
C-PP	mean biofilm thickness $\overline{L}_F$	8	0.474	1
	mean biofilm density		0.010	0.213
	fraction of inorganic compounds		0.012	0.303
SST	mean biofilm thickness $\overline{L}_F$	8	0.930	1
	mean biofilm density		0.014	0.607
	fraction of inorganic compounds		0.089	0.800

B Supplementary Information to Chapter 4

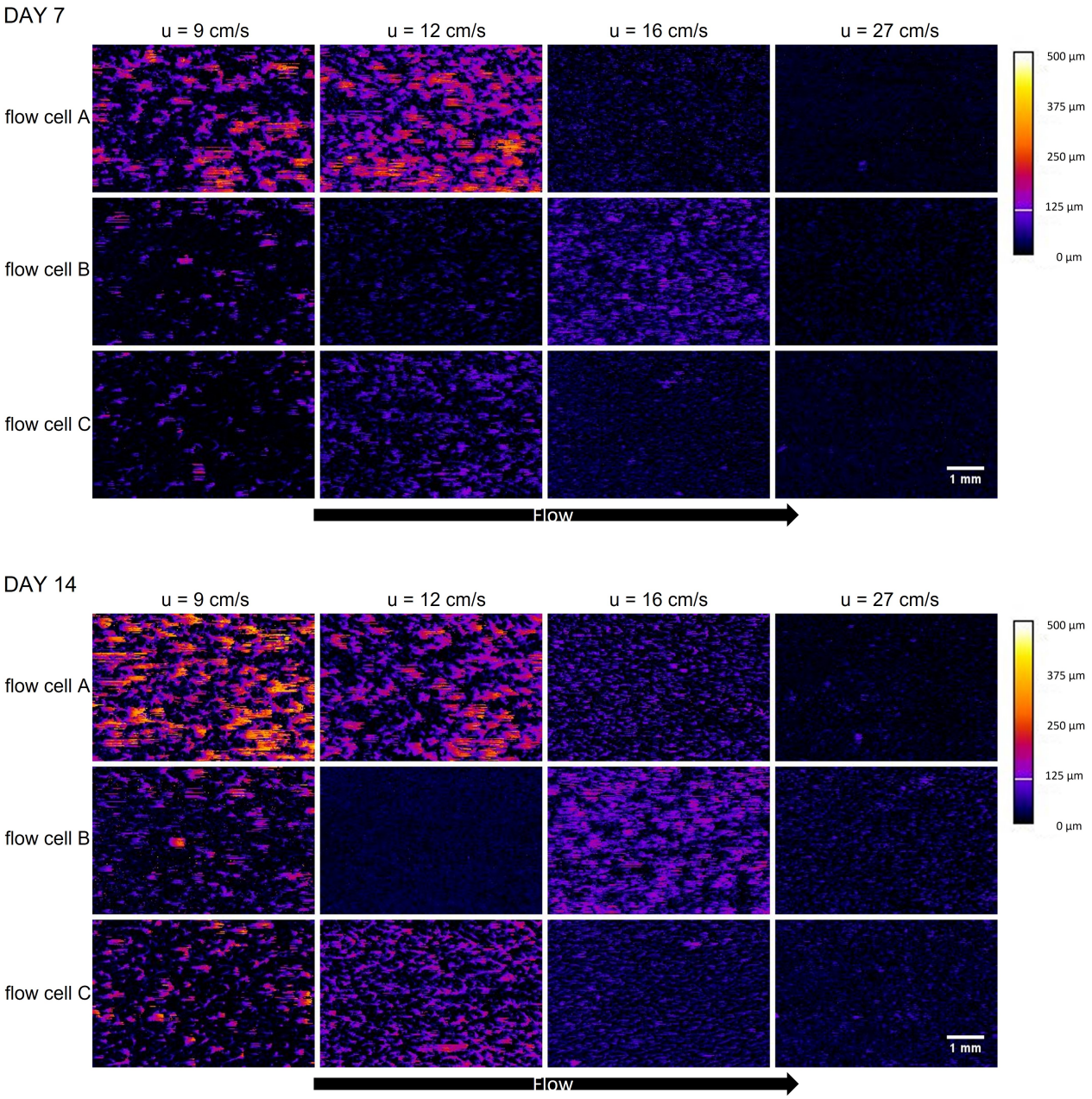

Figure A1: Height Maps ($6 \times 4mm^2$) displaying the bulk-biofilm interface of the flow cells A, B and C for all four flow velocities at Day 7 and 14 of cultivation. The direction of flow was from left to right.

Model for the theoretical calculation of the sensor sensitivity

For the development of the theoretical model of the sensor sensitivity, equations from the VDI-Wärmeatlas (2013) were used to calculate the three different contributors to the thermal resistance.

Table B.1: Input parameters for the mathematical model

Geometric variables		
A_{sensor}	Sensor area	100 mm²
d_i	Inner diameter pipe	25.4 mm
l_{pipe}	Length pipe	250 mm
l_{sensor}	Length sensor area	10 mm
r_i	Inner radius pipe	12.7 mm
s	Wall thickness pipe	3 mm
s_{C-PP}	Wall thickness C-PP	4 mm
$\overline{BV}$ or $\overline{L}_F$	Mean biovolume or biofilm thickness	0-1000 (µm³/µm²) or (µm)
Thermodynamic variables		
α	Heat transfer coefficient	W/(m² × K)
$\dot{Q}$	Heat flux	W
R	Thermal resistance	K/W
ΔT	Temperature difference	10 K
Material properties at 25 °C		
λ_{C-PP}	Thermal conductivity C-PP	21 W/(m × K)
λ_F	Thermal conductivity biofilm	0.6 W/(m × K)
λ_{water}	Thermal conductivity water	0.6 W/(m × K)
λ_{SST}	Thermal conductivity SST	13.6 W/(m × K)
Dimensionless numbers		
Nu	Nusselt number	f (Re, Pr)
Re	Reynolds number	compare Table 4.1
Pr	Prandtl number	6.137
η	Turbulence factor	-
γ	Intermittence factor	-

The required heat input $\dot{Q}$ to maintain a constant temperature difference Δ T is:

$$\dot{Q} = \frac{\Delta T}{R_{Total}} \tag{A}$$

With:

$$R_{Total} = R_{substratum} + R_F + R_{boundary\,layer} \tag{B}$$

The sensor sensitivity relates to:

$$sensor\,sensitivity \approxeq \frac{\Delta\overline{BV}}{\Delta\frac{R_F}{R_{Total}}} \tag{C}$$

For the application of the sensor to a planar substratum (e.g. flow cell):

$$R_{substratum} = \frac{1}{A_{Sensor}}\frac{s_{C-PP}}{\lambda_{C-PP}} \tag{D}$$

$$R_F = \frac{1}{A_{Sensor}}\frac{\bar{L}_F}{\lambda_F} \tag{E}$$

$$R_{convection} = \frac{1}{A_{Sensor} \times \alpha} \tag{F}$$

The heat transfer coefficient α_{fc} is a function of the Nusselt number (Nu = f (Re,Pr))

$$\alpha_{fc} = \frac{Nu_{fc} \times \lambda_{water}}{l_{Sensor}} \tag{G}$$

For flow conditions $10 < \mathrm{Re} < 10^7$:

$$Nu_{fc} = \sqrt{Nu_{lam}^2 + Nu_{turb}^2} \tag{H}$$

With:

$$Nu_{lam} = 0.664 \times \ Re^{\frac{1}{2}}\ timesPr^{\frac{1}{3}} \tag{I}$$

$$Nu_{turb} = \frac{0.037 \times \ Re^{0.8} \times Pr}{(1 + 2.443 \times Re^{-0.1} \times (Pr^{\frac{2}{3}} - 1)} \tag{J}$$

For the application of the sensor to a cylindrical substratum (e.g. pipe):

$$R_{substratum} = \frac{1}{2 \times \pi \times l_{Sensor}} \times \frac{\ln(\frac{r_i+s}{r_i})}{\lambda_F} \tag{K}$$

$$R_F = \frac{1}{2 \times \pi \times l_{Sensor}} \times \frac{\ln(\frac{r_i}{r_i - L_F})}{\lambda_F} \tag{L}$$

$$R_{convection} = \frac{1}{A_{Sensor} \times \alpha} \tag{M}$$

The heat transfer coefficient α is a function of the Nusselt number (Nu = f (Re,Pr))

$$\alpha_{pipe} = \frac{Nu_{pipe} \times \lambda_{water}}{d_i} \tag{N}$$

For laminar flow conditions Re < 2300:

$$Nu_{pipe} = 0.332 \times Pr^{\frac{1}{3}} \times (Re \times \frac{d_i}{l_{pipe}})^{\frac{1}{2}} \tag{O}$$

For flow conditions in the transient zone 2300< Re < 10000:

$$Nu_{pipe} = (1 - \gamma) * Nu_{pipe,lam} + \gamma * Nu_{pipe,\ turb} \tag{P}$$

With the intermittence factor γ:

$$\gamma = \frac{Re - 2300}{10000 - 2300} \tag{Q}$$

$$Nu_{pipe,turb} = \frac{\frac{\zeta}{8} * 10^4 * Pr}{(1 + 12.7\sqrt{\frac{\zeta}{8} * (Pr^{\frac{2}{3}} - 1)})} * \left(1 + \frac{1}{3} * \left(\frac{d_i}{l_{sensor}}\right)^{\frac{2}{3}}\right) \tag{R}$$

With the turbulence factor ζ:

$$\zeta = (1.8 * \log(Re) - 1.5)^{-2} \tag{S}$$

$$Nu_{pipe,lam} = (49.371 + (Nu_{m,t,2,lam} - 0.7)^3 + Nu^3_{m,t,3,lam})^{\frac{1}{3}} \tag{T}$$

$$Nu_{m,t,2,lam} = 1.615 * (2300 * Pr * \frac{d_i}{l_{sensor}})^{\frac{1}{3}} \tag{U}$$

$$Nu_{m,t,3,lam} = (\frac{2}{1 + 22 \times Pr})^{0.18} * (2300 * Pr * \frac{d_i}{l_{sensor}})^{\frac{1}{2}} \tag{V}$$

C Supplementary Information to Chapter 5

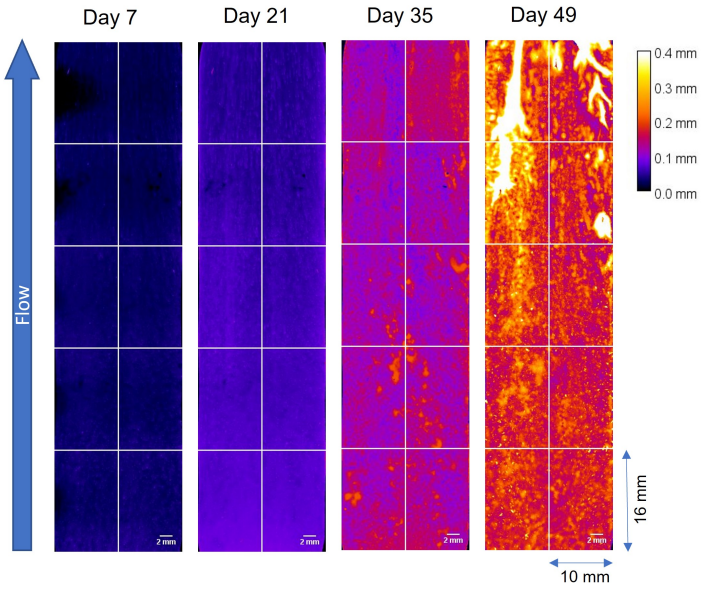

Figure A2: Height maps showing the distance of the bulk-biofilm interface from the electrode substratum of MEC A1 (see Table 5.1). For Days 7, 21, 35 and 49 a full scan displaying approx. 82 % of the electrode were taken. The height map displays the thickness of the biofilm according to the heat map for the range of 0-400 µm. The direction of flow was from bottom to top.

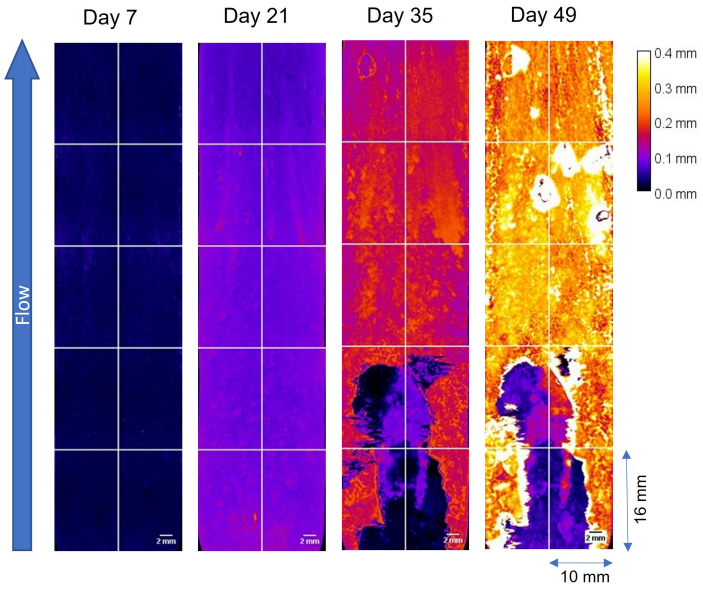

Figure A3: Height maps showing the distance of the bulk-biofilm interface from the electrode substratum of MEC A2 (see Table 5.1). For Days 7, 21, 35 and 49 a full scan displaying approx. 82 % of the electrode were taken. The height map displays the thickness of the biofilm according to the heat map for the range of 0-400 µm. The direction of flow was from bottom to top.

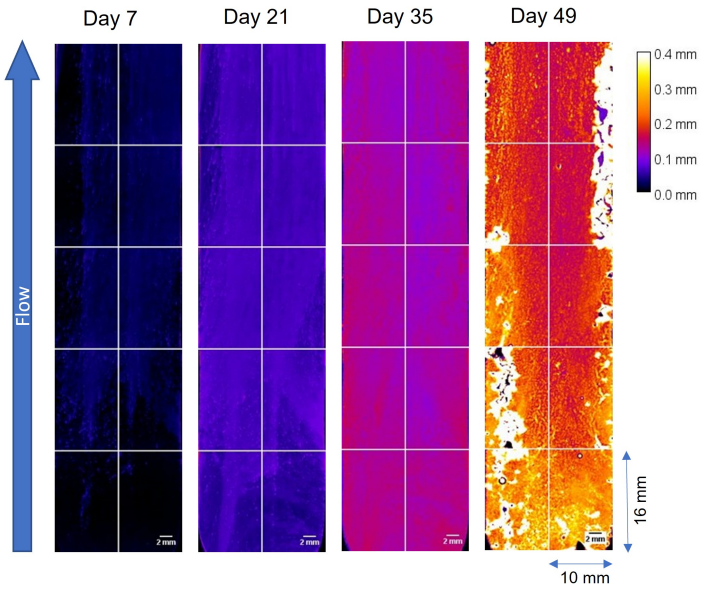

Figure A4: Height maps showing the distance of the bulk-biofilm interface from the electrode substratum of MEC A3 (see Table 5.1). For Days 7, 21, 35 and 49 a full scan displaying approx. 82 % of the electrode were taken. The height map displays the thickness of the biofilm according to the heat map for the range of 0-400 µm. The direction of flow was from bottom to top.

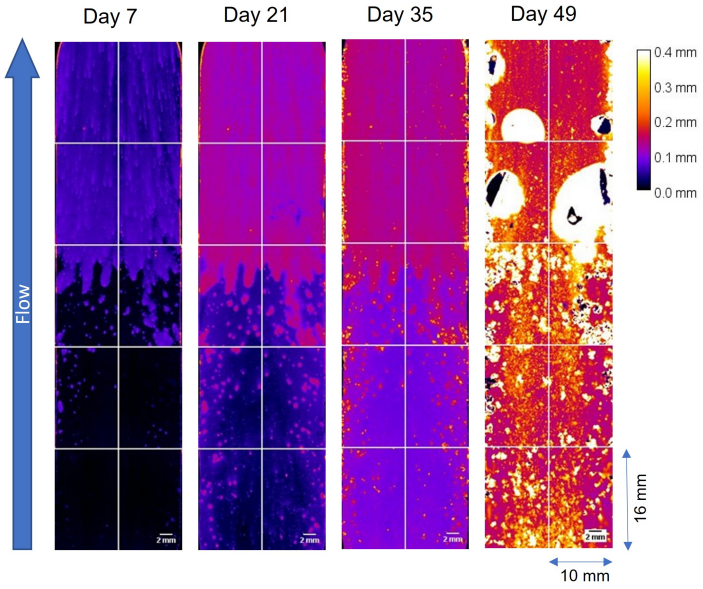

Figure A5: Height maps showing the distance of the bulk-biofilm interface from the electrode substratum of MEC B1 (see Table 5.1). For Days 7, 21, 35 and 49 a full scan displaying approx. 82 % of the electrode were taken. The height map displays the thickness of the biofilm according to the heat map for the range of 0-400 µm. The direction of flow was from bottom to top.

Paper 3 - Representativeness of OCT scan area

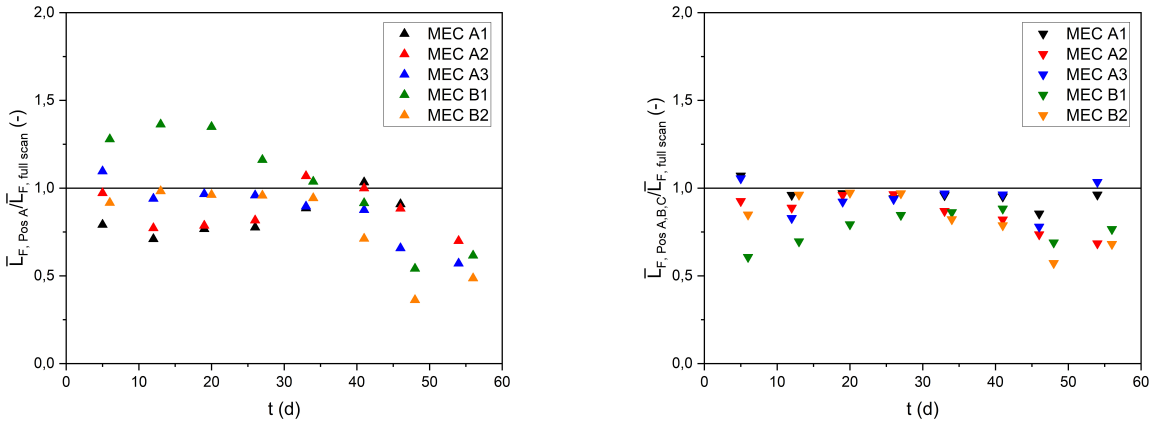

Figure A6: (left) Comparison of the mean biofilm thickness from imaging position A with the mean biofilm thickness from full scan images - showing the representativeness of the biofilm sensor measurement (right) Comparison of the mean biofilm thickness from imaging positions A, B and C with the mean biofilm thickness from full scan images - showing the representativeness of the daily imaging scheme for the correlation of the current density with the mean biofilm thickness